UNIVERSITY OF COPENHAGEN
FACULTY OF SCIENCE

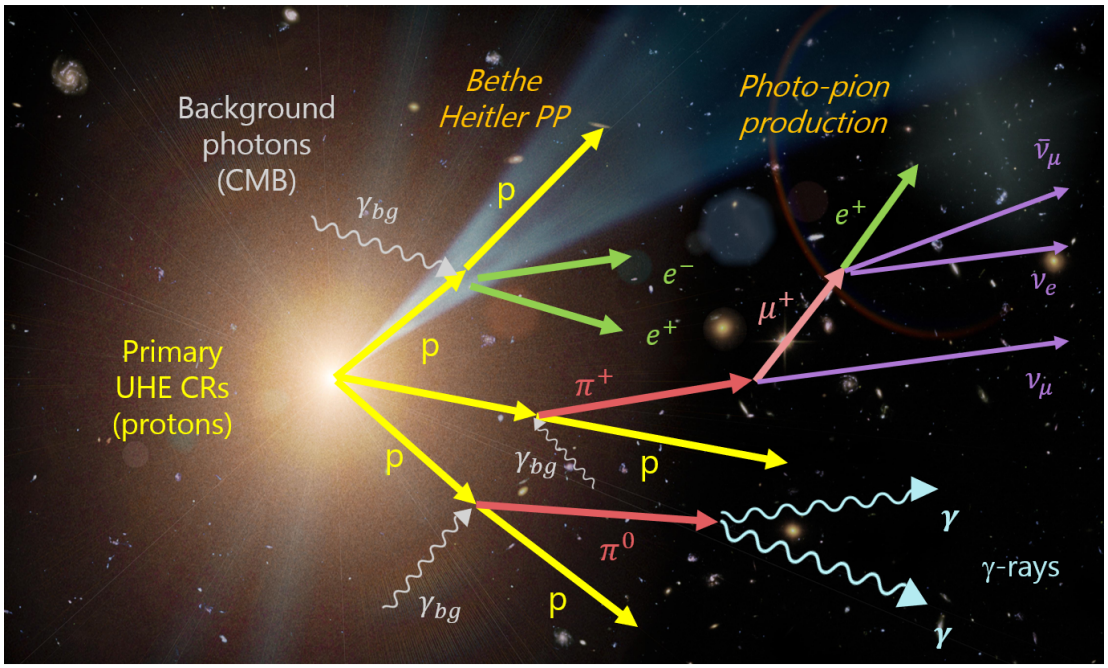

Master's thesis

Probing Ultra-High Energy Cosmic Ray Models with Cosmogenic Neutrinos and Photons

Kathrine Mørch Groth

Advisors: Markus Ahlers and Yoann Genolini

Submitted: August 13, 2021

Abstract

Cosmic ray (CR) interactions with cosmic radiation backgrounds are a guaranteed source of high-energy neutrinos and photons. The most optimistic scenario assumes the dominance of CR protons at ultra-high energies (UHE) that rapidly interact with the cosmic microwave background above the Greisen-Zatsepin-Kuzmin (GZK) cutoff. The corresponding cosmogenic fluxes are testable with present neutrino and CR observatories. On the other hand, if heavy nuclei dominate the UHECR spectrum, the fluxes of GZK neutrinos and photons can become orders of magnitude smaller. In this project we implement a new numerical cascade module designed for state-of-the-art Monte Carlo propagation codes like CRPropa to allow for efficient development of the electromagnetic cascades responsible for cosmogenic gamma ray fluxes. Combining this with CRPropa, we revise predictions of cosmogenic fluxes based on recent observations of the spectrum and chemical composition of UHECRs. In particular, we focus on deriving lower limits on the cosmogenic neutrino and photon flux depending on astrophysical uncertainties. We investigate the prospects and requirements of future large-scale neutrino and CR observatories to observe these fluxes.

Acknowledgments

I would like to thank my supervisors Markus Ahler and Yoann Genolini for their thorough guidance and support throughout the year of this Master's project. I am deeply grateful for the experience of the project as a fulfilling collaboration.

Furthermore, I would like to thank Markus, Yoann and Enrico Peretti for their invaluable advice on matters of both physics and career and for, especially in a year marked by the pandemic, making the everyday life in physics inspirational and fun.

I would like to express my gratitude to the IceCube group at the Niels Bohr Institute that I had the privilege of discussing my work with throughout the project: Jason Koskinen, Tom Stuttard, James Vincent Mead, Étienne Bourbeau and Tetiana Kozynets. A special thanks to Tetiana as well for our discussions in relation to the International Conference of Cosmic Rays and for her always helpful presence in general.

Finally, I would like to thank Mads, my parents and siblings and my friends for their loving care and support, and for reminding an absorbed physics student to eat plenty of snacks.

Contents

List of Figures

Introduction

Earth is constantly under bombardment of particles from outer space. Particles such as protons, neutrinos and photons reach us from sources near and far – from our own Sun to distant galaxies. Cosmic rays is the term used to refer to charged particles that arrive at Earth from space. The Pierre Auger (PA) Observatory has detected cosmic ray particles with extreme energies [1, 2] at over 10^{20} eV, making cosmic rays the most energetic particles we have ever seen in our universe and several orders of magnitude larger than the maximum energy attainable at the Large Hadron Collider at CERN. These particles, the so-called Ultra-High Energy Cosmic Rays (UHECRs), are thought to be extragalactic in origin, but their actual sources remain one of the biggest mysteries in modern physics. As they are charged particles, UHECRs get deflected in magnetic fields in our Galaxy and in the extragalactic space, obscuring the direction of their points of origin. Only for the most extreme energies is it believed that UHECR arrival directions could be correlated with the ones of their sources.

One way to constrain UHECR models is to fit spectral features of the arriving flux, which is a result of initial source spectra and the chemical composition of the UHECRs and interactions with cosmic radiation backgrounds. Remarkably, we see a strong suppression of the UHECR spectrum for extremely high energies, beyond approx. 50 EeV [1, 2]. This can have two different causes: it can be a result of the maximum energy that sources are able to accelerate the cosmic-ray nuclei up to, or it can be an effect of the interactions the cosmic rays undergo as they propagate through the photon fields that permeate extragalactic space. The latter effect is referred to as the GZK cutoff, named after Greisen, Zatsepin and Kuz'min who first predicted it [3, 4]. The GZK cutoff is caused by the scattering of UHECR protons with the cosmic microwave background (CMB), while heavier nuclei will photo-disintegrate on the CMB at the same energy. Due to the GZK cutoff, the propagation distance of UHECRs is limited to within a few 100 Mpc. So while we have observed UHECRs, we expect only to see parts of the full picture.

Luckily for us, UHECRs do not arrive on their own, but are accompanied by two other kinds of messengers: electromagnetic particles and neutrinos. These are directly related to the GZK mechanism as they are created when the UHECRs interact with the background fields of radiation that fill the extragalactic space. The neutrinos are much more promising when it comes to preserving their original energy and pinpointing their sources. Indeed, since neutrinos are weakly interacting particles, they will travel through the universe unhindered by deflections and photon interactions, carrying with them the footprints of their parent particles through their energy. The heavier the UHECRs constituents are, the higher initial energy it would take to produce the same neutrino flux as we would see from UHECRs made up only of protons. Detection of these neutrinos would thus not only help us understand where the UHECRs are produced, but also in what kinds, in what amounts and by which mechanisms.

The other accompanying messengers consist of high-energy photons – called γ-rays – together with electrons and positrons. However, these messengers strongly interact with the background radiation themselves, triggering cascades of many more electromagnetic particles. In this way, the original electromagnetic messengers will live too briefly to be observed by us, but we can instead detect the ensuing cascades. As the cascades, like the neutrinos, depend on the original energy and composition of the UHECR primary particles, they too can function as probes for the properties of the UHECRs. This is why we are interested in the secondary messengers of UHECRs as well. These so-called cosmogenic fluxes and UHECRs are signals from the farthest corners of our universe that can reveal

what incredulous objects must exist in order to send these extremely energetic particles our way.

Multimessenger astronomy that combines measurements of cosmic rays with different types of cosmic messengers like neutrinos and photons is a recent field. Two major events in 2017 in particular established that we are now in the age of multimessenger astronomy: The joint detection of gravitational waves from LIGO-Virgo [5] simultaneously with a γ-ray signal measured by the Fermi-Gamma-ray Burst Monitor in 2017, as well as the high-energy (though not cosmogenic) neutrinos measured by IceCube to coincide with a γ-ray flare measurement by the Fermi-Large Area Telescope (Fermi-LAT) and others from the blazar TSX 0506+056 in 2017 [6].

The current status of the field is that the cosmogenic neutrinos remain unobserved, while we see the cosmogenic γ-rays only indirectly through the contributions of their cascades to the isotropic γ-ray background. While new experiments are being built and proposed to detect these cosmogenic signals it is timely to reevaluate the expected fluxes with the latest advances on CR propagation and updated CR spectrum and composition data. To do so, we turn to simulations. We use a combination of Monte Carlo techniques (for UHECR and neutrino propagation) and a numerical transport equation solver custom-built for this thesis (for cosmogenic photon propagation). From this we can obtain minimal models for the cosmogenic neutrino flux that depend on the observed UHECR spectrum and composition as well as the source evolution of the UHECR sources. We need these minimal fluxes to constrain UHECR models and to estimate the required sensitivity of future neutrino and CR observatories necessary for their detection.

In this thesis we begin by introducing the components necessary for following the UHECRs from they escape from the sources, through propagation and until they reach Earth. We introduce the physical processes and interactions that impact both the CR spectrum and composition and generate the cosmogenic messengers, including the photon backgrounds that permeate the universe. The chapter concludes with a presentation of the multimessenger picture.

The next chapter (chapter 2) is devoted to the physics of the electromagnetic cascades initiated by the secondary electromagnetic particles from UHECR primaries. The cascades are mainly created when the electromagnetic particles interact with the photon backgrounds through the processes of electron-positron pair production followed by inverse Compton scattering. In this way the cosmogenic γ-rays created by the UHECRs cascade to lower energies and create γ-rays with energies in the GeV-TeV range.

Chapter 3 focuses on the propagation of UHECRs and the expected flux of cosmogenic neutrinos. We first present the methods used for our simulations and fits to recent UHECR data. Here we turn to a simulation of UHECRs using the Monte Carlo propagation code CRPropa [7] for which we use two composition models: a pure proton spectrum as well as a mixed-composition source model based on the recent data for the UHECR spectrum and composition. From this we get both the resulting CR spectra and the accompanying cosmogenic spectra. We present our approach to estimate minimal neutrino fluxes by considering the UHECR nucleon spectrum. We use a fit to the nucleon spectrum to obtain minimal models for the cosmogenic neutrinos flux that are consistent with the observed UHECR spectra and composition. The results from our studies of UHECRs and cosmogenic neutrinos conclude this chapter: the UHECR spectrum, the accompanying cosmogenic neutrino flux and the minimal fluxes established by the nucleon spectrum treatment, as well as their dependencies on different source model uncertainties. Here we discuss the important question of whether we will be able to detect the cosmogenic neutrinos with the planned future neutrino observatories.

As an extension of this analysis we built a custom Electromagnetic Cascades module (referred to as the "EM module" in the following) to be combined with the spectra from CRPropa in order to get the resulting electromagnetic fluxes (cascade γ-rays and electrons/positrons). Chapter 4 is devoted to the framework and methods used to construct the EM module. We provide verification of the output from the EM module through comparisons to CRPropa. In the next part of this chapter we combine the results from our simulations and fits from chapter 3 with our EM module. We present the outcome of propagating the first generation of EM particles obtained with the UHECR simulation through our custom EM module. The electromagnetic cascade flux computed with the EM module from different type of EM source injections are demonstrated in the end of this chapter. We reach then the concluding chapter 5 that summarises our work. As an outlook, we consider the path forward

for expanding the analysis and the EM module. An example is presented of using the EM module to compute the EM cascade emission from a nearby source.

The appendices contain three parts: part A contains the detailed derivations and additional calculations for the interaction rates and the Continuous Energy Loss (CEL) approximation used in the EM module. Part B consists of the building blocks of the EM module: elaborations of the matrix doubling method, the numerical handling of the integrations over interaction rates and the forward difference method used for the CEL approximation. It also presents a number of supporting plots of the results from the EM module. Finally, in part C we enclose the proceedings article from the 37th International Cosmic Ray Conference 2021 [8] wherein a part of this thesis was presented.

Chapter 1

Ultra-high energy cosmic rays and cosmogenic fluxes

The field of cosmic ray physics has a long history, dating back to the discovery of cosmic rays in 1912 by Victor Hess [10]. The first observation of an ultra-high energy cosmic ray was made in the 1960'ies [11]. In the following, the main aspects of UHECR physics that are of importance for the current work are presented. We will highlight the current results and measurements of key parameters for the analysis in the following chapters.

The cosmic ray energy spectrum is one of the major observables in astroparticle physics, as it can provide information on the types of source environments responsible for the cosmic rays as well as the physics of their propagation. A wide range of experiments aim to reach better statistics and precision of measurements of the energy spectrum. Figure 1.1 shows a collection of these together with the current highest-energy measurements of neutrinos (from IceCube — see sec. 1.2) and γ-rays (from Fermi-LAT [12]).

The spectrum extends from around 1 GeV ($= 10^9$ eV) to up just above 100 EeV ($= 10^{20}$ eV) and can be approximated by a power-law:

$$\frac{\mathrm{d}N}{\mathrm{d}E} \propto E^{-\gamma}, \tag{1.1}$$

where the value of γ changes slightly at different points along the spectrum.

To help physicists have a shared language for the cosmic ray spectrum, its shape has been likened to that of a leg and its features are named accordingly: we have a knee and an ankle where the spectral index changes. The knee at about $E_{knee} \approx 5 \times 10^{15}$ eV marks a softening of the spectrum. Latest results from the Pierre Auger Observatory (see below, in the end of this section) put the ankle at $E_{ankle} = 5.0 \pm 0.1 \pm 0.8 \times 10^{18}$ eV, where the spectral index changes from $\gamma = 3.29 \pm 0.02 \pm 0.10$ to $\gamma = 2.51 \pm 0.03 \pm 0.05$ with statistical and systematic uncertainties [2, 1].

The recent results from the Pierre Auger Observatory also report a new feature that challenges the physiological analogy with the introduction of a kink or "broken ankle" at $E_{kink} = 13 \pm 1 \pm 2 \times 10^{18}$ eV, where the spectrum softens, before reaching a final suppression at $E_{suppr} = 46 \pm 3 \pm 6 \times 10^{18}$ eV [2, 1]. To further complicate the leg-comparison, a second knee around 10^{17} eV has also been reported.

Interpretation of the knee feature is still under debate; for example, it could stem from the maximum energies attainable in the dominant galactic cosmic ray sources, such as supernova remnants [14]. Alternatively, it could indicate the energy above which cosmic rays more readily escape our Galaxy. The second knee could similarly be an effect from the maximum energy attainable by heavy nuclei such as iron at the sources [14].

The cause for the suppression in the cosmic ray spectrum seen above the ankle around 50 EeV is also not yet fully determined. However, the suppression fits very well with the predictions from the Greisen-Zatsepin-Kuz'min (GZK) effect [3, 4], whereby the UHECRs' collisions with the cosmic

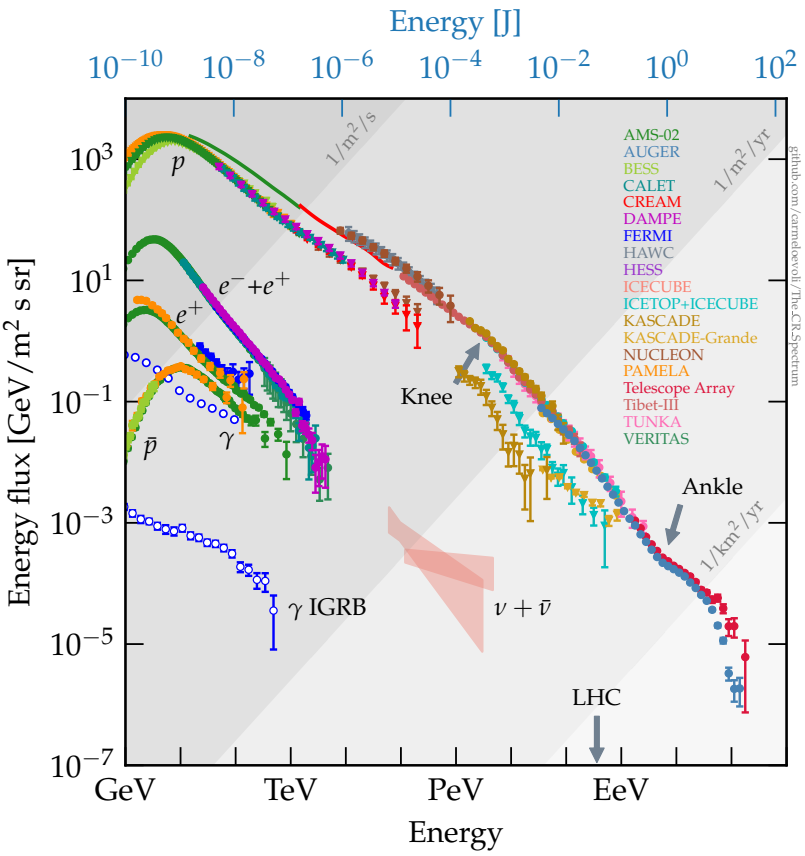

Figure 1.1: The cosmic ray spectrum: The cosmic ray all-particle spectrum ($J \times E^2$) as measured by a range of experiments with data after 2000 including the Pierre Auger Collaboration. The γ-ray fluxes observed by Fermi-LAT and a range of ground-based telescopes and HE neutrino fluxes from IceCube are also shown. From [13].

microwave background (CMB) create pions that thus take away energy from the primary cosmic rays at this energy. We will go into more details on this process in section 1.1.3. For heavier nuclei 50 EeV is also the energy where photodisintegration dominates and likewise leads to a steepening of the energy spectrum. Finally, it is assumed that the maximum energy attainable at the UHECR sources also makes up a contributing factor to the suppression [2]. In this thesis our focus will be the UHE part of the CR spectrum, defined as where energies exceed $E = 10^{18}$ eV (= 1 EeV, shown in the figure).

The spectra of UHECRs, neutrinos, γ-rays and electrons/positrons we focus on in this work are the ones that arrive at the top of Earth's atmosphere. These are often inferred from detection of the secondary particles created inside Earth's atmosphere by ground-based experiments. Charged particles such as UHECRs that enter Earth's atmosphere can emit Cherenkov radiation and excite the fluorescence of nitrogen atoms. UHECRs are low in numbers, as we see from the flux indications on figure 1.1, making vast detector areas necessary to make their detection probable. Extensive Air-Shower Array-experiments measure UHECRs by detecting the secondary particles that are created in cascades when CRs interact with atmospheric nuclei. In these reactions, the incoming CR colliding with atmospheric nuclei form short-lived hadrons that decay into photons, $e^{\mp}$, muons and neutrinos [9]. The UHECR spectrum and composition is inferred from the characteristics of the air shower that is measured in two ways: UHECR detector experiments like the **Pierre Auger Observatory** in Argentina [1] use a combination of surface detector arrays measuring the Cherenkov radiation and fluorescence detectors.

Composition

The composition of the cosmic rays — e.g. whether they are mainly protons or a mixture of heavier atomic nuclei — is important to understand in order to determine the sources, acceleration mechanisms and propagation effects for cosmic rays.

For cosmic rays with large enough fluxes, their composition can be measured directly in satellite and balloon experiments. As we go up in cosmic ray energy, their fluxes decrease, and the detectors must likewise increase in size, which leaves us with indirect ground-based detector experiments for UHECRs.

The composition of UHECRs is measured with extensive air shower experiments such as the above-mentioned Pierre Auger (PA) Observatory [15] and the Telescope Array (TA) [16]. Like PA, TA also measures the extensive air showers initiated when cosmic-ray particles collide with the particles of Earth's atmosphere. The mass of the primary particle can be inferred from the depth of the particle air shower maximum referred to as X_{max}. This depth is the distance from where the primary cosmic-ray particle enters the upper atmosphere to where the number of secondaries produced in the air shower is maximal. Since this distance depends on the mass or species of the initiating atomic nuclei, we can use it as a way to estimate the initial mass. The results will however strongly depend on the on the models used for CR interactions in atmosphere.

Measurements of the UHECR composition have had some tension between them, with the PA Observatory favouring a heavier composition at high energies than the one found by the TA experiment [15, 16, 14]. Recent data indicates that the UHECR composition gets lighter with increasing energy up until 2×10^{18} eV by the ankle. From the PA results, the composition gets heavier beyond this energy, while TA reports a light composition all the way to highest energies. A joint analysis between PA and TA indicated that the data from TA was also compatible with a heavier or mixed composition above $E \sim 10^{19}$ eV, in agreement with the results from PA [17]. There is hence compelling evidence against a proton-dominated composition at ultra-high energies.

Sources

UHECRs with energies above around $E = 5$ EeV are widely assumed to be of extragalactic origin due to two main reasons: There are no known sites in our galaxy able to produce cosmic rays of such high energies; and UHECRs appear to come from directions that lie outside of the galactic plane. As the Galactic magnetic field is not strong enough to deflect particles at these high energies, they cannot have originated within our galaxy. The reason for this is the Galactic magnetic field: Since cosmic rays are charged particles, they will be deflected in the magnetic field of the Galaxy before they can reach us – the higher the CR energy, the less deflection of their propagation path. This motion is described by the Larmor radius of curvature in a uniform magnetic field for a relativistic charged particle.

Cosmic rays with $E \sim 1$ PeV (around the knee in the cosmic ray spectrum) will have a Larmor radius r_L of the order of 1 parsec:

$$r_L \sim \frac{1.1 \text{ pc}}{Z} \left(\frac{E}{1 \text{ PeV}} \right) \left(\frac{B}{1 \, \mu\text{G}} \right)^{-1} , \tag{1.2}$$

where Z is the charge number of the cosmic ray and B is the magnetic field strength. Cosmic rays can be confined in the Galaxy by the Galactic magnetic field until r_L becomes larger than the typical size of the Galaxy ~ 10 kpc. For this reason, the knee feature of the cosmic ray spectrum on figure 1.1 is assumed to indicate the energies where galactic cosmic rays begin to escape our Galaxy. Above EeV energies, the CRs are believed to be extragalactic because their Larmor radius becomes larger than the typical size of the Galaxy ~ 10 kpc.

The transition between the galactic and extragalactic sources is not yet fully understood and can depend on e.g. the composition of the spectrum.

Sources of UHECRs are still unidentified, but a variety of possible candidates have been proposed and form an ongoing area of investigation. Current research by ref. [18] indicates that UHECR and HE neutrino data in combination favours sources that are small in size (< 10 pc) with strong

magnetic fields (> 1 mG). This is at the same time consistent with multimessenger constraints from γ-ray data. The types of source environments that match these requirements are e.g. Active Galactic Nuclei (AGN) (that make up 1% of all galaxies) and Tidal Disruption Events (TDEs).

The Hillas Criterion describes the necessary conditions for the confinement of cosmic rays in source environments. A particle can only stay within the region of acceleration responsible for its energy until its Larmor radius (equation (1.2)) exceeds the radius of the source region. We can thus convert the Larmor radius into a geometric condition for the maximum energy that can be reached by an accelerator characterised by its size R and the strength of its magnetic field B [19]:

$$E_{max} = 0.9\, Z\,(\beta_{sh}) \left(\frac{\Gamma\, R}{\mathrm{pc}}\right) \left(\frac{B}{\mu\mathrm{G}}\right) \mathrm{EeV}, \tag{1.3}$$

where Γ is the Lorentz factor of the flow and β_{sh} is the velocity of shocks in the environment relative to the speed of light. When particles trapped in a source environment reach this energy, they are able to escape the source and begin their propagation.

Figure 1.2 shows an updated version of a Hillas Plot [20] from ref. [19], a type of plot used to estimate which sources have a large enough combination of magnetic field and radius to be able to produce high CR energies, based on the Hillas Criterion. The Hillas plot in figure 1.2 shows what is required from a source environment in terms of the source size and magnetic field strength in order to be able to accelerate either protons or iron nuclei to an energy of $E = 10^{20}$ eV. The diagonal lines specify where the product of the size and magnetic field becomes large enough to meet this Hillas Criterion, whereby the source classes that lie to the left of the diagonal lines do not live up to the requirements.

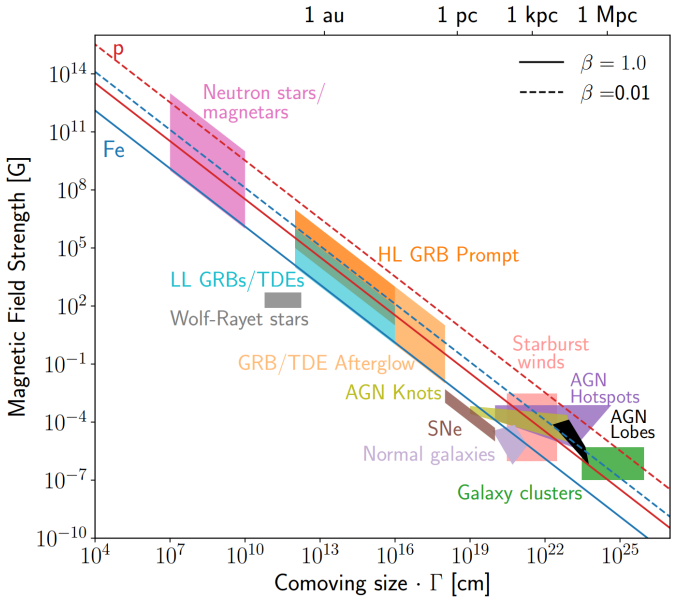

Figure 1.2: Hillas plot: The effective size R of a source environment, given as the product of the comoving size of the environment and the Lorentz factor Γ, plotted against its magnetic field strength B for various source classes. The diagonal lines indicate where the product $B\,R$ becomes large enough to confine protons and iron nuclei with energies $E = 10^{20}$ eV. The solid lines are for an outflow velocity of $\beta_{sh} = 1$ and the dashed lines are for slower shocks with $\beta_{sh} = 0.01$. From figure 10 in ref. [19].

From the equation (1.3), we see that E_{max} scales with charge number Z, meaning that a heavier UHECR composition will lower the requirements for the magnetic field and size of the source to reach a given energy. This is what we see in the figure 1.2, where the lines for iron nuclei are more inclusive of source classes.

When discussing the sources of UHECRs, another important aspect is their cosmological evolution with redshift. The source population responsible for UHECRs is typically assumed to follow the evolution of star formation. This assumes an evolution with redshift that goes as $\rho \sim (1+z)^m$ for

$m > 0$ [21]. The flux of UHECRs as well as the flux of cosmogenic neutrinos and γ-rays will depend on how their sources evolve with redshift. We will consider the effects of the redshift evolution of the sources of UHECRs and see how it impacts cosmogenic fluxes in section 3.4.1.

1.1 UHECR propagation

In this chapter we will start from the master equations of UHECR propagation — the Boltzmann equations — and introduce their building blocks: the interaction rates of UHECRs with background photon fields. After reviewing the different intergalactic photon fields, we will describe the key interaction processes for UHECRs and their secondaries, namely Bethe-Heitler pair production, pion-production and photodisintegration.

Since we will be working with cosmic rays traversing cosmological distances, we need to take into account the effect of the expansion of the universe. Because the expansion scales with distance, light from distant sources is redshifted.

We assume the standard ΛCDM cosmology, describing a universe made up of matter, a cosmological constant Λ and Cold Dark Matter. In this model, the rate of expansion is given by the Hubble parameter as:

$$H(z) = H(0)\sqrt{\Omega_\Lambda + \Omega_m(1+z)^3}, \tag{1.4}$$

where we use the parameter values given in [22]. Here the dark energy density parameter is $\Omega_\Lambda = 0.685 \pm 0.007$ and the pressureless matter (including cold dark matter) is given by the parameter $\Omega_m = 0.315 \pm 0.007$. The present-day Hubble expansion rate $H(0)$ is $100\,h\,\mathrm{km\,s^{-1}\,Mpc^{-1}}$, with scaling factor $h = 0.674 \pm 0.005$.

The Hubble parameter is necessary in order to calculate the light-travel distance from a source to us, given by:

$$d_{travel} = c\int_0^z \frac{dz'}{(1+z')H(z')}. \tag{1.5}$$

We will use this when we calculate Δt in equation (4.19) for propagation with our EM module.

Furthermore, cosmic rays with energy E will lose energy due to the expansion of the universe:

$$-\frac{1}{E}\frac{dE}{dt} = H_0. \tag{1.6}$$

We will refer to this as their adiabatic energy loss due to expansion.

1.1.1 The Boltzmann equations

The propagation of UHECRs, neutrinos and γ-rays over large distances through the universe can be described by a set of Boltzmann equations:

$$\dot{Y}_i = \partial_E(HEY_i) + \partial_E(b_iY_i) - \Gamma_iY_i + \int dE'\,\gamma_{i\to i}(E',E)\,Y_p(E') + \sum_j \int dE'\,\gamma_{j\to i}(E',E)\,Y_j(E') + \mathcal{L}_i. \tag{1.7}$$

Here Y_i is the comoving number density of particle type i. The first term in (1.7) governs the expansion of the universe and redshift energy losses that the particles suffer as a result. Continuous energy losses are described in the second term with energy loss rate $b = -\frac{dE}{dt}$. For UHECRs, these include Bethe-Heitler pair production on the Cosmic Microwave Background as described in the subsequent sections. Particle losses due to inelastic processes are described by the third term, where Γ_i is the interaction rate. The next two terms concern particle generation with the differential interaction rates $\gamma_{i\to i}$ and $\gamma_{j\to i}$. Finally, the last term is the emission rate density of CRs of type i per comoving volume, which contains information about the redshift evolution of the sources as well as their particle emission.

The comoving number density of the particle type i is related to the ordinary number density n_i through redshift as:

$$Y_i = \frac{a(z)^3}{a_0^3} n_i(z) = \frac{n_i}{(1+z)^3}. \tag{1.8}$$

The density n_i can always be converted to flux J_i, if we assume it to be isotropic, with the following units:

$$J_i = \frac{c}{4\pi} n_i, \tag{1.9}$$

$$[n_i] = \frac{\#\text{ particles}}{\text{cm}^3\cdot\text{eV}}, \tag{1.10}$$

$$[J_i] = \frac{\#\text{ particles}}{\text{s}\cdot\text{cm}^2\cdot\text{sr}\cdot\text{eV}}. \tag{1.11}$$

The Boltzmann equations thus describe the evolution of the flux of the CR particles.

Before they reach us, UHECRs from extragalactic sources must traverse the ambient background photon fields in the extragalactic space. How much they interact with these fields in different processes is described by the interaction rates Γ_i and $\gamma_{i\to j}$ that appear in the Boltzmann equations above.

The interaction rate for a highly relativistic charged particle of type i propagating through an isotropic photon background is given by the general formula [23]:

$$\Gamma_i(E_i) = \lambda_i^{-1}(E_i) = \frac{1}{2}\int_{\varepsilon_{th}}^{\infty} \mathrm{d}\varepsilon \int_{-1}^{1} \mathrm{d}\cos\theta\ (1-\beta_i\cos\theta)\, n_\gamma(\varepsilon)\, \sigma_{i\gamma}^{\text{tot}}, \tag{1.12}$$

where $\beta_i \approx 1$ is the (relativistic) velocity of the particle i with energy E_i, ε is the energy of the background photon (in the laboratory-frame), $n_\gamma(\varepsilon)$ is the photon energy distribution (from the differential photon density $\mathrm{d}n_\gamma = \frac{1}{2} n_\gamma(\varepsilon)\,\mathrm{d}\theta\,\mathrm{d}\varepsilon\sin\theta$), and $\sigma_{i\gamma}^{\text{tot}}$ is the total cross section of the interaction.

For a given process, ε_{th} is the minimum threshold energy for the background photons required in order for the process to take place.

The Boltzmann equations (1.7) act as the general master equations governing both the propagation of the UHECR primary particles and the secondaries they produce, namely neutrinos, electrons/positrons and photons. The equations depend on the interaction rates, which in turn depend on the cross sections (σ^{tot} in equation (1.12)). The solutions to the Boltzmann equations can be obtained by different means. We will use a Monte Carlo-based method via the framework in CRPropa for solving the equations for UHECR propagation. We will subsequently return to the Boltzmann equations for electromagnetic particles in chapter 2 in order to describe the electromagnetic cascades from cosmogenic fluxes, for which we will use a numerical framework — the EM module in chapter 4.

1.1.2 Photon backgrounds

An important component in the propagation of UHECRs and cosmogenic fluxes is the diffuse photon background radiation that permeates the universe. As the cosmic ray particles travel through the extragalactic space at high energies, the photons from the photon backgrounds in the universe are boosted in the CR frame leading to collisions and scattering processes.

These photon backgrounds range from the low-energy cosmic radio radiation (called Universal Radio Background or URB in the following) through the microwave region of the Cosmic Microwave Background (CMB) up to the infra-red and UV radiation that we will refer to as the Extragalactic Background Light (EBL). Figure 1.3 contains an overview of these backgrounds and show their overlap.

Cosmic Microwave background

Electrons and photons created in the interactions of primary cosmic ray particles with the CMB photons will in turn interact with the CMB photons continually until their energy is depleted below the threshold, creating the electromagnetic cascades responsible for the γ-rays in the GeV-TeV-range.

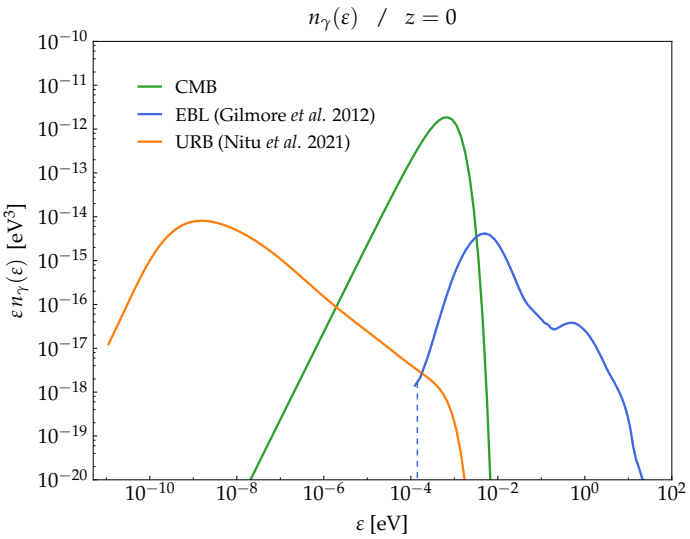

Figure 1.3: Photon background fields: Photon spectral number density $n_\gamma(\varepsilon)$ for the Cosmic Microwave Background, the Extragalactic Background Light (including the infra-red background) from Gilmore *et al.* 2012 [24] and the Universal Radio Background from Nitu *et al.* 2021 [25], at redshift $z = 0$. The dashed line shows the interpolation of the EBL model.

The photon energy spectral density in natural units ($[n_\gamma(\varepsilon)] = \text{eV}^2$) is given by the Planck spectrum:

$$n_{CMB}(\varepsilon) = \left(\frac{\varepsilon}{\pi}\right)^2 \left[\exp(\varepsilon/k_B T) - 1\right]^{-1} . \tag{1.13}$$

where T is the temperature of the photons of the CMB: $T = 2.7255\,\text{K}$, which in natural units becomes $T\,k_B = 0.2349\,\text{meV}$ [22]. As shown in figure 1.3, the CMB spectral density has a strong peak around this energy, which is referred to as the typical energy of a CMB photon.

Extragalactic background light

We use the EBL data from Gilmore *et al.* 2012 [24] in terms of the flux ϕ in units [erg sec^{-1}cm^{-2}ang^{-1}sr^{-1}] and the rest frame wavelength λ_0 in [ang]. We transform this to the spectral density $n_\gamma(\varepsilon)$ we need by:

$$n_\gamma(\varepsilon)\,[\text{MeV}^{-1}\,\text{m}^{-3}] = \phi\,[\text{erg s}^{-1}\text{cm}^{-2}\text{ang}^{-1}\text{sr}^{-1}] \cdot \frac{\lambda_0\,[\text{ang}]}{\varepsilon^2\,[\text{MeV}^2]} \frac{4\,\pi}{c\,[\text{m/s}]} \frac{624151\,[\text{MeV}]}{[\text{erg}]} \frac{[\text{m}^{-2}]}{10^{-4}\,[\text{cm}^{-2}]} \tag{1.14}$$

Finally, going to natural units, we get $n_\gamma(\varepsilon)\,[\text{MeV}^2]$. The EBL from Gilmore *et al.* 2012 is given as tabulated data (as is usually the case for EBL). We perform an interpolation over this data in order to include $n_{EBL}(\varepsilon)$ in the numerical integrations of interaction rates in the EM module (see chapter 4). The EBL model and its interpolation are shown in figure 1.3.

Universal radio background

UHECRs do not interact directly with the universal radio background, but as we will see in our treatment of electromagnetic cascades, the secondary particles created during propagation will have interactions with the radio background photons.

The radio foreground of our own galaxy makes it difficult to precisely model the radio background. We use a current estimate of the Universal Radio Background (URB) from Nitu *et al.* 2021 [25] that is shown in figure 1.3.

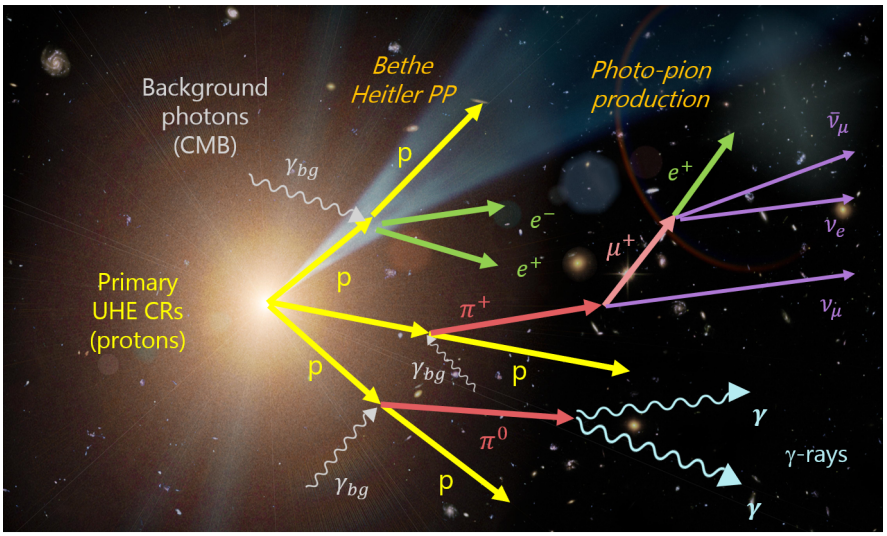

Figure 1.4: Illustration of interactions of a UHECR proton on the photon background fields: Bethe-Heitler pair production and photo-pion production[1]. Background image courtesy of NASA/JPL-Caltech.

1.1.3 Interactions

Bethe-Heitler pair production

For energies around the ankle in the cosmic ray spectrum, the dominant interaction is the Bethe-Heitler pair production [26] on the CMB. A cosmic ray proton or nucleus X, characterised by its mass number A and charge number Z, can reach high enough energies to interact with the low-energy photons in the CMB or the EBL and create an electron-positron pair:

$$ {}^A_Z X + \gamma_{bg} \rightarrow {}^A_Z X + e^+ + e^- . \tag{1.15} $$

This process is referred to as Bethe-Heitler pair production in this thesis in order to distinguish it from the Breit-Wheeler pair production relevant in the electromagnetic cascades (sec. 2.2).

The energy of the background photons will be boosted in the rest frame of the cosmic ray proton or nucleus. The threshold cosmic ray energy for this process is:

$$ E^{BH}_{thr} = \frac{m_e c^4 \, (m_X + m_e)}{\varepsilon} \approx 4.8 \times 10^{17} \, A \left(\frac{\varepsilon}{\text{meV}} \right)^{-1} \text{eV}, \tag{1.16} $$

where ε is the energy of the CMB photon [27, 28].

If we express the energy loss rate suffered by protons due to Bethe-Heitler pair production as $b^{BH}_p(E)$, the corresponding loss rate for a cosmic nucleus ${}^A_Z X$ will scale with the square of its charge number:

$$ b^{BH}_X(A) \simeq Z^2 \, b^{BH}_p(E/A). \tag{1.17} $$

The electrons and positrons created in Bethe-Heitler pair production can go on to produce high-energy photons via Inverse Compton scattering, which is described in detail in section 2.3 in the chapter on electromagnetic cascades.

Above 50 EeV, the Bethe-Heitler process becomes subdominant with respect to two other processes: photo-pion production and photodisintegration.

[1] Note that not all subsequent decay reactions of photo-pion production are included in the illustration – see equation (1.19) for the full reaction chain.

Photo-pion production

When UHECRs become energetic enough, they will see the photons from the background radiation fields boosted by large Lorentz factors causing them to interact. The UHECR energy needs to be high enough to produce pions in order for the cosmogenic fluxes to be created.

Photo-pion production is the production of pions in reactions of UHE nucleons with background photons γ_{bg}:

$$N + \gamma_{bg} \to N + \pi, \tag{1.18}$$

where N is a nucleon. The pion-production process peaks when it happens via the Δ resonance (Δ^+) at a threshold energy similar to the pion-production threshold:

$$p + \gamma_{CMB} \to \Delta^+ \to \begin{cases} \pi^+ + n & \begin{cases} \pi^+ \to \mu^+ + \nu_\mu, & \mu^+ \to e^+ + \nu_e + \bar{\nu}_\mu. \\ n \to p + e^- + \bar{\nu}_e. \end{cases} \\ \pi^0 + p & \begin{cases} \pi^0 \to \gamma + \gamma. \\ p. \end{cases} \end{cases} \tag{1.19}$$

The Δ^+ hadron decays immediately to either a charged pion and a neutron, or a neutral pion and a proton. The charged and neutral pions will continue to decay into an antimuon and muon neutrino and into photons, respectively, while the neutrons also decay into a proton, electron and electron antineutrino. Finally, the antimuon also decays, producing a further set of neutrinos: the electron neutrino and the muon antineutrino, together with a positron. As wee see from either of the two main branches in the reaction chain in equation (1.19), we always end up with a proton in the end. Because of this, the UHECRs are seen as losing energy while producing the cosmogenic fluxes [9].

The energy threshold for pion-production is high. From the square of the centre of momentum frame energy $s = (p_\pi + p_p)^2$, we get the energy threshold for a nucleon colliding head-on with a background photon: [29]

$$E_{thr}^{pion} = \frac{m_\pi c^4 (m_N + m_\pi/2)}{2\varepsilon} \approx 6.8 \times 10^{19} \left(\frac{\varepsilon}{\text{meV}}\right)^{-1} \text{eV}. \tag{1.20}$$

For CMB photons, their typical energy is around 1 meV, as we see from figure 1.3. When we consider UHECR protons, the pion-production process becomes important around $E_{GZK} = 50$ EeV, which is exactly what generates the GZK cutoff mentioned above. For nuclei, the threshold energy scales with the mass number A as $E_{thr}^{pion,\text{N}} \sim A \times E_{GZK}$, since the pion-production must take place for the nucleons in the UHECR nuclei, which will have an energy E/A [9]. We will use this effect when we describe the UHECR nucleon spectrum in section 3.3.

Photodisintegration

In the photodisintegration process, cosmic ray nuclei interact with background photons which leads to fragmentation of the nuclei. An example of the photodisintegration process is given by:

$$^{56}Fe + \gamma_{CMB} \to {}^{55}Mn + p, \; {}^{55}Mn + \gamma_{CMB} \to {}^{54}Mn + n, \; n \to p + e^- + \bar{\nu}_e. \tag{1.21}$$

Photodisintegration is an important production channel for photons from UHECRs. Photodisintegration of UHECR nuclei on the CMB dominates over photo-pion production and Bethe-Heitler pair production for higher energies above $E \sim E_{GZK} \approx 50$ EeV for nitrogen and above $E \sim 10^{20}$ eV for iron [30].

We can describe the length that a UHECR particle can travel from a source before it loses energy in interactions by the energy loss length $\left(\frac{1}{E}\frac{dE}{dx}\right)^{-1}$ [21]. The energy loss lengths for different processes depend on the corresponding cross sections and are typically computed by Monte Carlo simulation methods, an example of which is shown in figure 1.5. As the figure shows, the Bethe-Heitler pair production process dominates for energies from approx. 10^{18} eV to a little before the photo-pion production threshold energy at $E_{GZK} \sim 5 \times 10^{19}$ eV. Above this energy we see that the photo-pion

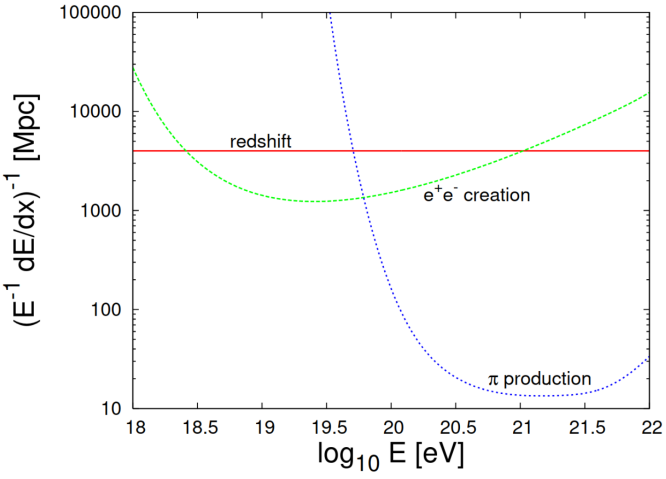

Figure 1.5: UHECR energy loss lengths: Energy loss lengths for UHECR protons interacting with the CMB for the processes Bethe-Heitler pair production (labeled "e^+e^- *creation*"), photo-pion production (labeled "π *production*") and energy loss length due to the Hubble expansion (labeled "*redshift*"). From figure 1 in ref. [31].

production dominates with energy loss lengths down to 10 Mpc, which creates the GZK cutoff effect for the highest energies.

All three processes, Bethe-Heitler pair production, photo-pion production and photodisintegration, as well as the adiabatic energy loss due to the expansion of the universe, are implemented in the propagation code CRPropa as described in [32, 29] – we return to this in Chapter 3.

1.2 Cosmogenic fluxes

The cosmogenic neutrinos predicted to be produced from UHECRs have not yet been observed. As seen from the photo-pion production process described above, high-energy neutrinos are sure indicators of hadronic sources — not only are they produced in the interactions between UHE cosmic rays and the ambient photon fields during propagation, but also in hadronic interactions with the photon fields inside the source environments.

Once the cosmogenic messengers have been created as secondaries in the interactions of UHECRs with the extragalactic background radiation, they will have very different fates in terms of their onward travels.

The cosmogenic photons and electrons/positrons will have eventful journeys full of encounters. After their creation by the UHECR interactions, they will in turn interact with the background photon fields and initiate electromagnetic cascades of large amounts of new electromagnetic particles. The main interaction processes relevant for their propagation are treated in chapter 2.

Neutrinos are important messengers in astroparticle physics as they are only weakly interacting particles. They interact weakly via the Z boson in neutral current interactions or in charged current interactions via the $W^{\pm}$ bosons. This makes them difficult to measure in a laboratory setting, but gives them advantages over other messengers when they arrive to us from space. Since the probabilities for the cosmogenic neutrinos to interact with anything they encounter in their path is so low, they will essentially propagate freely through the universe after their creation. They will only be affected by the adiabatic energy losses due to the cosmological expansion as described in section 1.1 as well as neutrino flavour oscillations which we will briefly describe below. Consequently, the cosmogenic neutrinos will have traveled largely unimpeded through space and thus point directly back to their sources.

Neutrinos are also important for cosmology, since they affect the structure formation in the early universe. They hold the potential for discoveries of new physics beyond the standard model.

Neutrinos are the lightest of all the fermions, but they are not massless – a crucial feature that was discovered via the observation of neutrino oscillations, a major milestone of modern particle physics and a deviation from the Standard Model.

The extraordinary property of neutrino oscillations allows a neutrino of one of three flavour eigenstates (ν_e, ν_μ and ν_τ) to oscillate into another flavour state (and correspondingly for their three anti-neutrino flavours). This happens as they travel through space where their propagation eigenstates are mass eigenstates, which are superpositions of the flavour eigenstates. We describe the oscillations via the neutrino mixing parameters: three mixing angles and a phase factor that can reveal if the neutrinos break the charge conjugation parity symmetry.

If the neutrino masses are slightly different from each other, they will travel at slightly different speeds so that their mass eigenstates will acquire slightly different phase shifts as they propagate. This then leads to a slightly different superposition of flavour states than the original one, which is what we see as an oscillation of a neutrino flavour.

In order for the neutrinos to undergo the oscillations we have detected experimentally, they must then have unequal masses. We do not know their absolute masses, but their mass difference and their mixing angles have been determined from observations.

If we use a simplified neutrino model with only 2 flavours, we can describe the finite probability that an initial flavour (e) transforms into the other flavour (μ) after travelling a distance x as:

$$P(\nu_e \to \nu_\mu) = \sin^2(2\theta) \sin^2\left(\frac{\delta m^2 x}{4E}\right), \tag{1.22}$$

where $\sin^2(2\theta)$ describes the amplitude, $\frac{\delta m^2 x}{4E}$ expresses the phase and δm^2 is the mass difference. Since the masses of the mass eigenstates are different, the phase can become non-zero, so for a given (non-zero) mixing angle θ, the probability of measuring a different flavour can change with the distance travelled. The expression thus shows that the probabilities oscillate over the propagation distance.

From the Δ resonance decay in pion-production from section 1.1.3, we saw that the cosmogenic neutrinos and antineutrinos are created as ν_e, $\bar{\nu}_e$, ν_μ and $\bar{\nu}_\mu$. As they propagate through space until they are detected at Earth, the cosmogenic neutrinos will also undergo flavour oscillations. Neutrino oscillations are not normally included in the calculations of cosmogenic neutrino fluxes, since they are assumed to travel very long distances. For this reason they can be approximated by assuming that equal flavour ratios $\nu_e : \nu_\mu : \nu_\tau = 1 : 1 : 1$ reach us at Earth [21].

For astrophysical and cosmogenic neutrinos, the higher-energy neutrinos have lower fluxes, as was also the case for UHECRs — but in addition, neutrinos also have very small cross-sections as they are only weakly interacting particles. Hence massive ground-based telescopes are needed in order enable detection, such as the **IceCube South Pole neutrino observatory** and its future extension, **IceCube-Gen2** [33]. Neutrino telescopes are built as a grid of detectors (Photo Multiplier Tubes) in either ice or water in order to have a large (cubic kilometre scale) transparent volume for the telescope while also shielding the detectors from photons and other secondary particles. Neutrinos that interact with the ice will produce secondary particles travelling faster through the ice than light does and thus emit Cherenkov light. The PMTs measure the numbers of photons from the Cherenkov light and their arrival times at different places in the telescope grid, wherefrom the properties of the parent neutrino such as energy, arrival direction and neutrino flavour can be reconstructed [9].

1.3 Multimessenger relations

The central idea in multimessenger astronomy is to take advantage of the intimate connections there are between the different cosmic messengers. The relations allow us for example to make estimations of neutrino and γ-ray fluxes from the measurements of UHECRs, or to estimate the expected flux of high-energy neutrinos from observations of γ-rays.

In other words, multimessenger astronomy is about making the most out of the precious data that we have. Measurements are expensive and hard to obtain. Even if we had the ideal instruments,

we would still always be limited in our possibilities for observing the universe due to our location; we will only ever be able to see the universe from our particular viewpoint, obscured for the rest of the universe by our Galaxy, magnetic fields, and even our motion through space. This is why we need to squeeze the signals we are able to obtain for every last drop of information, and to this end connecting multiple signals is a powerful method.

In this work, our focus is UHECRs and their relations to cosmogenic neutrinos and γ-rays. The fourth type of messenger besides cosmic rays, neutrinos and photons is the gravitational waves emitted from extreme events such as the merging of two black holes, and which lie outside the scope of this work.

As mentioned above, the GZK effect is responsible for the cosmogenic fluxes. UHECRs interact with the photons from the background radiation fields via Bethe-Heitler pair production, photo-pion production via the Δ-resonance and for the case of UHECR nuclei, by photodisintegration. All these interactions redistribute energy from the primary CR particle to the generated secondary particles. In Monte Carlo simulations of the propagation of UHECR protons, typical levels of the energies of the primary protons and resulting cosmogenic neutrinos and γ-rays are found to be related as:

$$E_p : E_\gamma : E_\nu = 1 \ : \ 0.1 \ : \ 0.05. \tag{1.23}$$

Ratios like these give us direct multimessenger relations between the observations of the different messengers. If we see UHECR protons at 50 EeV energies, we expect to also see cosmogenic neutrinos with 5% of this energy, i.e. with energies in the EeV range [9].

The cosmogenic fluxes are closely related to the source models of the UHECRs that produced them. Both the size and features of the fluxes will depend on the initial energy spectrum and composition of the UHECRs, as well as the source evolution with redshift. In this way, the cosmogenic fluxes function as useful probes for UHECRs, but as the predictions of the cosmogenic fluxes are model dependent, they have large variances. In this thesis we will investigate how the cosmogenic fluxes are affected by these different uncertainties of the UHECR source models.

When we consider the fluxes of the three messengers UHECRs, high-energy neutrinos and γ-rays simultaneously, we see a remarkable feature. As we will see in figure 4.6 in the summary of our results, their fluxes share the same absolute intensity. This indicates that they could be powered by the same source populations. The γ-rays observed by Fermi-LAT from extragalactic sources are dominated by emission from blazars [34]. Blazars are a subcategory of AGN that have jets (which holds for 10% of all AGN) that are pointed towards us (which is the case for approx. 1% of jetted AGN). This makes blazars rare and extreme objects. In fact, they are the most powerful objects in the universe in terms of emission, only surpassed for brief seconds by the emissions from Gamma Ray Bursts. The observations by Fermi could suggest that neutrinos and UHECRs could be dominated by blazars as well due to the correspondence of their fluxes, as we will see in figure 4.6. However, IceCube seems to disfavour blazars as the dominant source type for HE neutrinos based on the low level of observed fluxes; we should have detected more if they primarily came from blazars [35].

Individual blazars can still act as HE neutrino sources, however. This was demonstrated in 2017 with the detection by IceCube of a HE neutrino that coincided with γ-ray flaring from the blazar TXS 0506+056 detected by Fermi-LAT and other observatories. Subsequent analysis by IceCube of archival data for this source location showed a 3.5σ significance as they found a neutrino flare in 2014/15 (though with an absence of γ-ray flares in the same period) [6].

Currently we have no strong (5σ-level) discoveries of HE neutrino emission from known galactic or extragalactic sources, but several other candidates like TXS 0506+056 are being investigated through multimessenger networks and have shown compelling evidence for neutrino emission. When IceCube measures a HE neutrino, a public alert is sent out enabling e.g. Fermi-LAT to follow up and to look for blazars that coincide with the neutrino measurement. Through networks like these, multimessenger physics have a large potential for new discoveries. Hence improving our understanding of the connections between UHECRs and other messengers is becoming increasingly important.

Chapter 2

Electromagnetic cascades

The chapter presents calculations of interaction lengths and energy loss lengths for UHECR photons and electrons interacting with the background photon fields that lead to electromagnetic cascades.

The cascades are initiated by the first wave of photons and electrons that is generated in the processes described in the preceding chapter, when UHECR primaries undergo photodisintegration, photo-pion production and Bethe Heitler-pair production, as illustrated in figure 2.1.

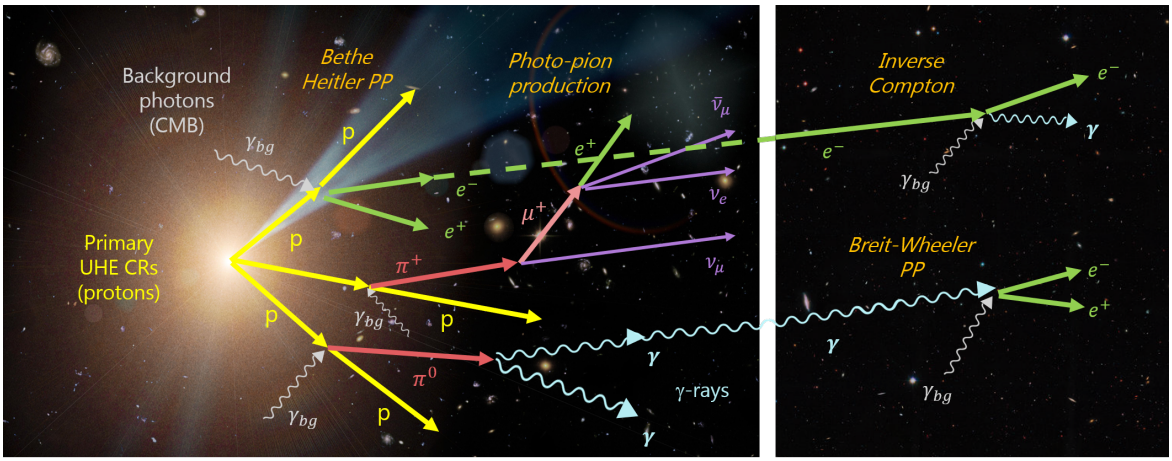

Figure 2.1: *Left:* Illustration of interactions for a UHECR proton on the background photon fields (Bethe-Heitler pair production and photo-pion production). *Right:* Subsequent electromagnetic interactions from the produced electrons and photons with the background photon fields (Inverse Compton scattering and Breit-Wheeler pair production). Background image courtesy NASA/JPL-Caltech.

The two processes responsible for the electromagnetic cascade development are Breit-Wheeler Pair Production (PP) for photons and Inverse Compton scattering (IC) for electrons [1]. Breit-Wheeler PP is given by the reaction: $\gamma + \gamma_{bg} \rightarrow e^- + e^+$, whereby a high-energy photon is absorbed by interacting with a low-energy background photon and create an electron-positron-pair. IC scattering is described by the reaction $e^- + \gamma_{bg} \rightarrow e^- + \gamma$, where a high-energy electron scatters on a low-energy background photon, producing a high-energy photon.

The evolution of electromagnetic cascades is the result of a combination of these two processes: A high-energy photon (γ-ray) will interact with the background photons in the intergalactic space creating cascade pairs of electrons and positrons via the PP process. The pairs of electrons and positrons will in turn interact with the background photons via IC scattering and produce cascade

[1] See chapter 5 for considerations about additional processes.

photons. If the upscattered photons have high enough energies to restart the PP process, they will initiate further Inverse Compton scatterings as well, whereby an electromagnetic cascade develops.

The detection of the electromagnetic cascades can take place both on the ground or in space. Electrons and γ-rays from the cascades will develop further electromagnetic cascades in the atmosphere of the Earth when they interact with the particles of the atmosphere. Ground-based experiments can give results for the TeV-range, whereas satellite detectors such as the **Fermi-LAT satellite** can directly measure γ-rays in the GeV range [9, 36].

Throughout this chapter we will be using natural units (Heaviside-Lorentz units): $\hbar = c = \varepsilon_0 = \mu_0 = 1$.

2.1 Cascade equations

The evolution of the flux of photons and electrons/positrons (referred to as electrons / e in the following) is governed by the master equations for CR transport, the Boltzmann equations in (1.7). From these we can form two equations for the comoving number densities of photons and electrons [40]:

$$\partial_t n_\gamma = -\Gamma_{PP}\, n_\gamma + \int \mathrm{d}E_e\, \gamma^{IC}_{e\to\gamma}(E_e, E_\gamma)\, n_e(E_e) \tag{2.1}$$

$$\partial_t n_e = -\Gamma_{IC}\, n_e + \int \mathrm{d}E_e\, \gamma^{IC}_{e\to e}(E_e, E_e)\, n_e(E_e) + \int \mathrm{d}E_\gamma\, 2\,\gamma^{PP}_{\gamma\to e}(E_\gamma, E_e)\, n_\gamma(E_\gamma). \tag{2.2}$$

In the equation for $\partial_t n_e$, we include a factor of 2 with the Pair Production differential interaction rate $\gamma^{PP}_{\gamma\to e}(E_\gamma, E_e)$ to account for the fact that we treat both electrons and positrons simultaneously. The differential interaction rate depends on the differential cross section, as we will see below. Due to symmetry, the differential cross section written in terms of the outgoing positron energy is identical to the one for outgoing electron energy in equation (2.15).

The total interaction rates $\Gamma(E_i)$, given by equation (1.12), are related to the differential interaction rates $\gamma(E_i, E_j)$ by [41]:

$$\Gamma_i(E_i) = \sum_j \int \mathrm{d}E_j\, \gamma_{i\to j}(E_i, E_j). \tag{2.3}$$

The integration strategy for the interaction rates that was used for optimising the calculations in the EM module is presented in detail in Appendix A.1.

In order to solve the system of equations in equations (2.1) and (2.2), we will need to define their main ingredients: the total and differential interaction rates, that in turn depend on the total and differential cross sections.

In the following sections we will present the cross sections and interaction lengths for the two processes, PP and IC, that will be implemented in the EM module for propagation of UHE photons and electrons/positrons.

2.2 Breit-Wheeler Pair Production

In the Breit-Wheeler Pair Production process, a UHE photon is absorbed by interacting with a background photon creating a pair of electrons and positrons.

The total PP interaction rate has the form given by equation (1.12). For the calculation of this total interaction rate, we follow Gould & Schréder (1967) [42] and change integration variable from $\cos\theta$ to the quantity:

$$\boxed{s_{\mathrm{GS}} \equiv \frac{\varepsilon E_\gamma (1-\cos\theta)}{2m_e^2} = \frac{s}{4m_e^2},} \tag{2.4}$$

a dimensionless version of the invariant squared centre of momentum frame energy $s = (p_i^\mu + p_j^\mu)(p_\mu^i + p_\mu^j) = (p_i + p_j)^2 = 2\varepsilon E_\gamma(1 - \cos\theta)$. Here E_γ is the energy of the γ-ray and ε is the energy of the background photon. In this parameterisation, the minimum value for $s_{\rm SG}$ (and integration limit) becomes $s_{\rm SG,min} = 1$, since if $s_{\rm GS} < 1$, we have $\varepsilon E_\gamma < m_e^2$, and hence the production of the e^+e^--pair cannot take place. The upper limit for the quantity $s_{\rm GS}$ is determined by the maximal scattering angle: $s_{\rm GS,max} = \frac{\varepsilon E_\gamma(1-\cos\theta_{\rm max})}{2m_e^2} = \frac{\varepsilon E_\gamma}{m_e^2}$. This transforms the expression for the total PP interaction rate into:

$$\Gamma_{PP}(E_\gamma) = \lambda_{PP}^{-1}(E_\gamma) = 2\left(\frac{m_e^2}{E_\gamma}\right)^2 \int_{\frac{m_e^2}{E_\gamma}}^{\infty} \mathrm{d}\varepsilon\ \frac{n_\gamma(\varepsilon)}{\varepsilon^2} \int_1^{\frac{\varepsilon E_\gamma}{m_e^2}} \mathrm{d}s_{\rm GS}\ s_{\rm GS}\,\sigma_{PP}(s_{\rm GS}). \tag{2.5}$$

The threshold condition (for head-on photon collision) for the PP process in terms of the background photon energy is thus: $\varepsilon_{th}\, E_\gamma = m_e^2 \ \Rightarrow\ \varepsilon_{th} = \frac{m_e^2}{E_\gamma}$. Translated to the γ-ray energy, this gives a threshold of [43]:

$$E_{\gamma,th} = \frac{m_e^2}{\varepsilon} \simeq 2.6 \times 10^{11} \left(\frac{\varepsilon}{\mathrm{eV}}\right)^{-1} \mathrm{eV}. \tag{2.6}$$

To obtain the total interaction rate we use the total cross section for Breit-Wheeler pair production from S. Lee (1998) [44], given by:

$$\sigma_{PP} = \sigma_T \cdot \frac{3}{16}(1-\beta^2)\left[(3-\beta^4)\ln\frac{1+\beta}{1-\beta} - 2\beta(2-\beta^2)\right], \quad \text{where} \tag{2.7}$$

$$\beta \equiv \left(1 - \frac{4m_e^2}{s}\right)^{1/2} = \left(1 - \frac{1}{s_{\rm GS}}\right)^{1/2}, \tag{2.8}$$

where σ_T is the Thompson cross section. The corresponding differential cross section for Breit-Wheeler pair production for a photon with energy E_γ to produce an electron of energy E'_e is given by [44]:

$$\frac{\mathrm{d}\sigma_{PP}}{\mathrm{d}E'_e} = \sigma_T \cdot \frac{3}{4}\frac{m_e^2}{s}\frac{1}{E_\gamma}\left[\frac{E'_e}{E_\gamma - E'_e} + \frac{E_\gamma - E'_e}{E'_e} + E_\gamma(1-\beta^2)\left(\frac{1}{E'_e} + \frac{1}{E_\gamma - E'_e}\right) - \frac{E_\gamma^2(1-\beta^2)^2}{4}\left(\frac{1}{E'_e} + \frac{1}{E_\gamma - E'_e}\right)^2\right], \tag{2.9}$$

restricted by the range: $\frac{1-\beta}{2} \le \frac{E'_e}{E_\gamma} \le \frac{1+\beta}{2}$.

For the calculation for the CMB, we introduce a parameter $\varepsilon_0 = \frac{\varepsilon}{k_B T}$ to perform the integration over the background photon energy over a normalised, dimensionless variable. For the other photon backgrounds, EBL and URB, we rescale the photon energy by the tabulated minimum energy instead of the characteristic CMB photon energy $k_B T$. Using the rescaled photon energy ε_0 and a reduced version of the cross section, we can write equation (2.5) as integrations over only dimensionless quantities times a prefactor. We refer the reader to Appendix A.1 for details of the calculation of the interaction rates. In natural units, Γ is given in units of eV, and we convert the interaction length $\Gamma^{-1}(E_\gamma) = \lambda(E_\gamma)$ to units of megaparsec by multiplying with $\hbar c$:

$$\lambda_{PP}(E_\gamma)\,[\mathrm{eV}^{-1}] = (\Gamma_{PP}(E_\gamma)\,[\mathrm{eV}])^{-1} \ \rightarrow\ \hbar c\,\Gamma_{PP}^{-1}(E_\gamma)\ \ [\mathrm{Mpc}]. \tag{2.10}$$

The interaction length is shown in figure 2.2. Pair Production on the Cosmic Microwave Background dominates for energies between $\sim 10^9$ MeV and 10^{12} MeV with interaction lengths down to below 10 kpc. For lower energies, the Extragalactic Background Light takes over and dominates, while the higher energies above $E \sim 10^{13}$ MeV are dominated by the Universal Radio Background. Here the radio background suppresses the cascade development with interaction lengths down to ~ 1 Mpc.

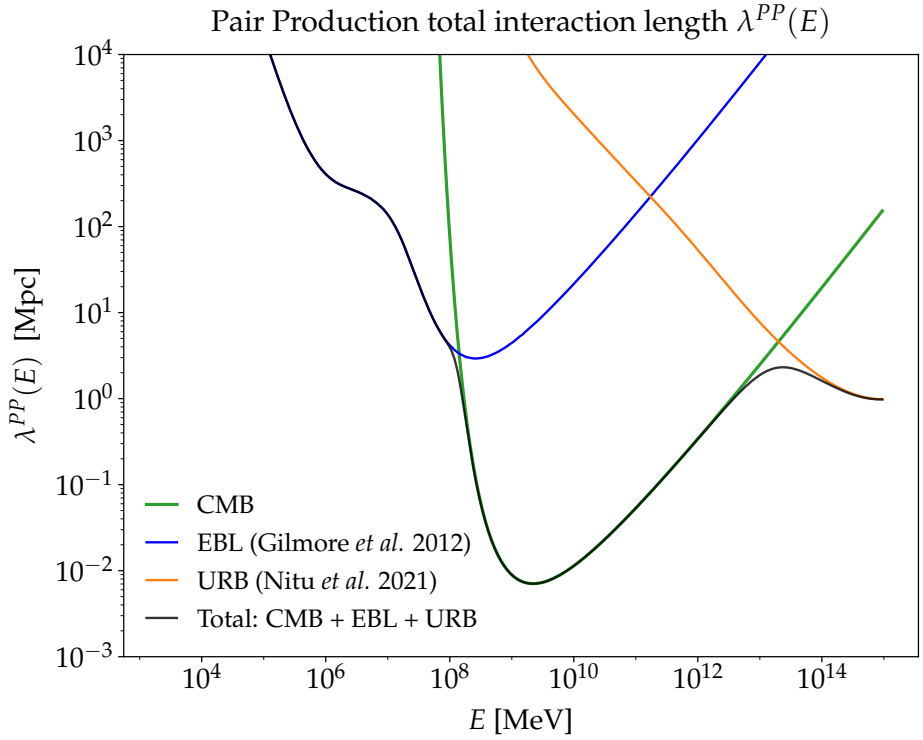

Figure 2.2: Pair Production: Interaction lengths for Breit-Wheeler Pair Production on the photon backgrounds CMB, EBL and URB.

The differential interaction rate $\gamma(E_i, E_j)$ from equation (2.3) likewise becomes:[2]

$$\begin{aligned}\gamma^{PP}_{\gamma\to e}(E_\gamma, E_e) &= \frac{1}{2}\int \mathrm{d}\varepsilon \int \mathrm{d}\cos\theta\,(1-\cos\theta)\,n_\gamma(\varepsilon)\,\frac{\mathrm{d}\sigma_{PP}}{\mathrm{d}E_e}(E_\gamma, E_e) \\ &= 2\left(\frac{m_e^2}{E_\gamma}\right)^2 \int_{\frac{m_e^2}{E_\gamma}}^{\infty} \mathrm{d}\varepsilon \int_1^{\varepsilon\, E_\gamma/m_e^2} \mathrm{d}s_{\mathrm{GS}}\;\frac{n_\gamma(\varepsilon)}{\varepsilon^2}\,s_{\mathrm{GS}}\,\frac{\mathrm{d}\sigma_{PP}}{\mathrm{d}E_e}(E_\gamma, E_e). \end{aligned} \tag{2.11}$$

2.3 Inverse Compton scattering

In the Inverse Compton scattering process, the electron colliding with a background photon can transfer a fraction of its energy to the photon. It is called the inverse of Compton scattering, since the electrons lose energy instead of the photons as in the ordinary Compton scattering.

Two regimes are defined for the IC process in terms of the energy of the incoming electron: the Thompson regime for low energies and Klein-Nishina regime for high energies. In the Thompson regime, the incoming electron collides with a background photon and up-scatters it to an energy proportional to the original background photon energy. In the Klein-Nishina regime, a fraction of energy is transferred from the electron to the photon, whereby the up-scattered photon energy depends less on its own original energy. This is the energy domain that will be most relevant for the calculations in our EM module.

We consider the interaction rate for Inverse Compton scattering. Following the integration strategy we used for Pair Production above, we start by changing integration variable from $\cos\theta$ to a dimensionless

[2] In Chapter 4 we will need the "one-bin integrated" differential interaction rate $\bar{\gamma}^{PP}(E, E')$. This is defined as: $\bar{\gamma}_{i\to j}(E, E') \equiv \int_{E'_L}^{E'_R} \mathrm{d}E'\;\gamma_{i\to j}(E, E') = 2\left(\frac{m_e^2}{E_\gamma}\right)^2 \int_{E'_L}^{E'_R} \mathrm{d}E'\;\int_{\frac{m_e^2}{E_\gamma}}^{\infty} \int_1^{\varepsilon\, E_\gamma/m_e^2} \frac{n_\gamma(\varepsilon)}{\varepsilon^2}\,s_{\mathrm{GS}}\,\frac{\mathrm{d}\sigma_{i\to j}}{\mathrm{d}E'}(E, E')\;\mathrm{d}s_{\mathrm{GS}}\;\mathrm{d}\varepsilon$, where E'_R and E'_L denote the right-bin edge and left-bin edge respectively.

version, this time called s', of the invariant squared total energy-momentum four-vector:

$$\boxed{s' \equiv \frac{s}{4m_e^2}.} \tag{2.12}$$

This quantity differs slightly from above due to an extra term from the mass of the electron in the process, where we in Pair Production had massless photons as initial particles. Under this parameterisation, the general expression for the interaction rate transforms to (analogously to (2.11) above):

$$\Gamma_{IC}(E_e) = \lambda_{IC}^{-1}(E_e) = 2\left(\frac{m_e^2}{E_e}\right)^2 \int_0^\infty \mathrm{d}\varepsilon \, \frac{n_\gamma(\varepsilon)}{\varepsilon^2} \int_{\frac{1}{4}}^{\frac{\varepsilon E_e}{m_e^2}+\frac{1}{4}} \mathrm{d}s' \left(s' - \frac{1}{4}\right) \sigma_{IC}(s'). \tag{2.13}$$

For more details, we refer the reader to Appendix A.2 and A.3.

For Inverse Compton scattering, there is not a threshold background photon energy ε_{th} in the way there was for Pair Production. Still following the integration strategy from Pair Production above, we substitute the integration variable $\varepsilon \to \varepsilon_0 = \frac{\varepsilon}{k_B T}$ for the case of interactions with CMB. With a reduced version of the cross section and the integration variable substitutions, we can write the interaction length for IC on the CMB in eqn. (2.13) as integrations over dimensionless quantities – see section A.2 in the Appendix for this derivation.

The cross section for Inverse Compton scattering in the Klein Nishina-regime is given by [44]:

$$\sigma_{IC} = \sigma_T \frac{3}{8} \frac{m_e^2}{s\,\beta} \left[\frac{2}{\beta(1+\beta)}(2 + 2\beta - \beta^2 - 2\beta^3) - \frac{1}{\beta^2}(2 - 3\beta^2 - \beta^3) \ln \frac{1+\beta}{1-\beta} \right], \tag{2.14}$$

where this time we have $\beta \equiv \frac{s-m_e^2}{s+m_e^2} = \frac{4s'-1}{4s'+1}$ as the velocity of the outgoing electron (center-of-mass frame). The corresponding differential cross section for an electron with energy E_e to produce an outgoing electron of energy E_e' is given by [44]:

$$\frac{\mathrm{d}\sigma_{IC}}{\mathrm{d}E_e'} = \sigma_T \cdot \frac{3}{8} \frac{1}{4s'} \frac{1}{E_e} \frac{1+\beta}{\beta} \left[\frac{E_e'}{E_e} + \frac{E_e}{E_e'} + \frac{2(1-\beta)}{\beta} \left(1 - \frac{E_e}{E_e'}\right) + \frac{(1-\beta)^2}{\beta^2} \left(1 - \frac{E_e}{E_e'}\right)^2 \right], \tag{2.15}$$

$$\frac{\mathrm{d}\sigma_{IC}}{\mathrm{d}z} = \pi r_c^2 \frac{1}{4s'} \frac{1+\beta}{\beta} \left[z + z^{-1} + \frac{2(1-\beta)}{\beta} \left(1 - z^{-1}\right) + \frac{(1-\beta)^2}{\beta^2} \left(1 - z^{-1}\right)^2 \right], \tag{2.16}$$

where in the second line we used the substitution for $z = \frac{E_e'}{E_e} \;\Rightarrow\; \frac{1}{E_e}\,\mathrm{d}E_e' = dz$. The differential cross section is restricted to the range: $\frac{1-\beta}{1+\beta} \leq \frac{E_e'}{E_e} = z \leq 1$.

Figure 2.3 shows the IC interaction length on the CMB, EBL and URB. The process is dominated by the contribution from interactions with CMB for all energies up to around 10^{11} MeV, where the radio background takes over as the dominant background. We see that the contribution from the EBL is overshadowed along the entire energy range by the CMB and radio counterparts, which give interaction lengths down to ~ 1 kpc for energies below $\sim 10^9$ MeV. The energy loss length on the CMB will be important in an approximation we use for the implementation of the IC process in the EM module, as described in section 4.1.2. The calculation of the URB interaction length becomes numerically unstable for values of s' that approach the lower limit $s'_{\mathrm{min}} = 1/4$. For this reason, the curve for the URB interaction length does not continue constantly into the Thomson regime for lower energies as we would expect. We show this expectation by the dashed orange line in figure 2.3. The divergent behaviour of the total interaction rate will have no effects on the calculations in the EM module, since the radio background contribution is completely drowned out by the shorter CMB interaction length for low energies.

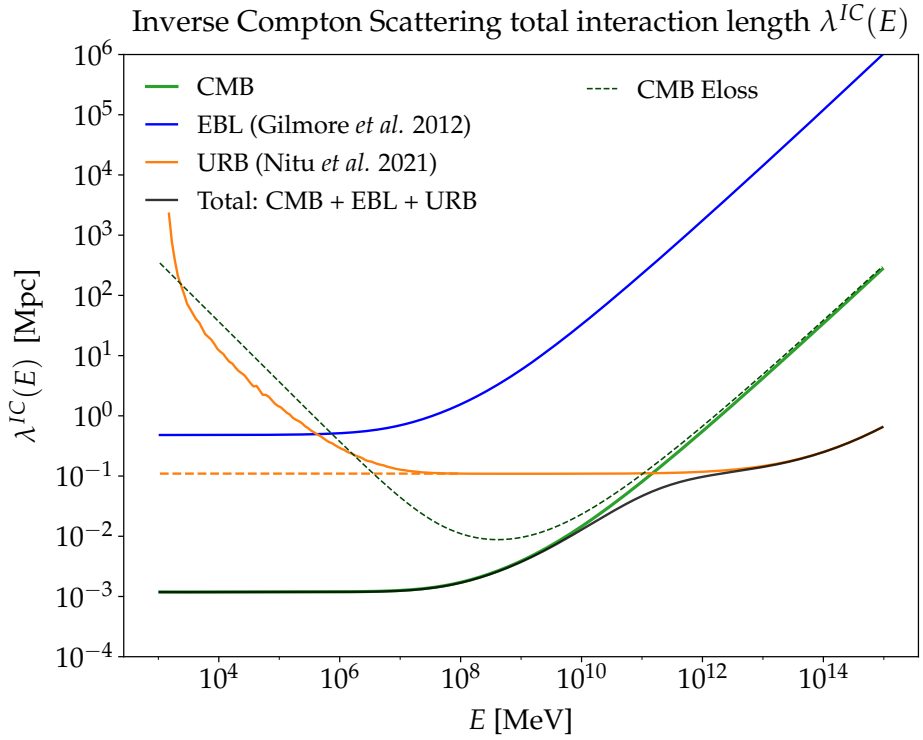

Figure 2.3: Inverse Compton scattering: Interaction lengths and energy loss length for Inverse Compton scattering on the photon backgrounds CMB, EBL and URB. The predicted continuation of the URB interaction length towards lower energies is shown as the dashed orange line. The dashed green line shows the Inverse Compton energy loss length for CMB.

IC energy loss length

We next consider the energy loss length for Inverse Compton scattering and take as our starting point the general formula:

$$\begin{aligned}\left(\lambda^{loss}(E)\right)^{-1} &= \frac{1}{E}\frac{dE}{dt} = \frac{1}{E}\int \mathrm{d}E'\,\gamma(E,E')\,(E-E') \\ &= \frac{1}{2}\int \mathrm{d}\varepsilon \int \mathrm{d}\cos\theta\,(1-\cos\theta)\,n_\gamma(\varepsilon)\int \mathrm{d}E'\,\frac{\mathrm{d}\sigma}{\mathrm{d}E'}\left(1-\frac{E'}{E}\right).\end{aligned} \tag{2.17}$$

Plugging the differential cross section from equation (2.16) into the expression for the energy loss length, we get:

$$\left(\lambda_{IC}^{loss}(E_e)\right)^{-1} = 2\left(\frac{m_e^2}{E_e}\right)^2\int_0^\infty \mathrm{d}\varepsilon\,\frac{n_\gamma(\varepsilon)}{\varepsilon^2}\int_{1/4}^{\frac{\varepsilon E_e}{m_e^2}+\frac{1}{4}} \mathrm{d}s'\,\left(s'-\frac{1}{4}\right)\int_{\frac{1-\beta}{1+\beta}}^1 \mathrm{d}z\,\frac{\mathrm{d}\sigma_{IC}}{\mathrm{d}z}\,(1-z). \tag{2.18}$$

The energy loss length is shown as a dashed green line in figure 2.3. Details of the derivation can be found in A.2.2.

Differential interaction rates γ_{IC}

From the general formula in equation (2.3), we get the differential interaction rate for Inverse Compton scattering $\gamma_{IC}(E_e, E_e')$, in terms of the ingoing and outgoing electron energies E_e and E_e':

$$\left(\lambda_{IC}^{loss}(E_e)\right)^{-1} = 2\left(\frac{m_e^2}{E_e}\right)^2\int_0^\infty \mathrm{d}\varepsilon\,\frac{n_\gamma(\varepsilon)}{\varepsilon^2}\int_{1/4}^{\frac{\varepsilon E_e}{m_e^2}+\frac{1}{4}} \mathrm{d}s'\,\left(s'-\frac{1}{4}\right)\int_{\frac{1-\beta}{1+\beta}}^1 \mathrm{d}z\,\frac{\mathrm{d}\sigma_{IC}}{\mathrm{d}z}\,(1-z). \tag{2.19}$$

$$\gamma^{IC}_{e\to e}(E_e, E'_e) = \frac{1}{2}\int \mathrm{d}\varepsilon \int \mathrm{d}\cos\theta\,(1-\cos\theta)\,n_\gamma(\varepsilon)\,\frac{\mathrm{d}\sigma_{IC}}{\mathrm{d}E'_e}(E_e, E'_e)$$
$$= 2\left(\frac{m_e^2}{E_e}\right)^2 \int_0^\infty \mathrm{d}\varepsilon\,\frac{n_\gamma(\varepsilon)}{\varepsilon^2}\int_{1/4}^{\frac{\varepsilon E_e}{m_e^2}+\frac{1}{4}} \mathrm{d}s'\,\left(s'-\frac{1}{4}\right)\frac{\mathrm{d}\sigma_{IC}}{\mathrm{d}E'_e}. \tag{2.20}$$

We use energy conservation (and neglect the low energy of the background photon) to get the differential interaction rate in terms of the energy of outgoing photon, letting $E'_e = E_e - E'_\gamma$:

$$\gamma^{IC}_{e\to\gamma}(E_e, E'_\gamma) = \frac{1}{2}\int \mathrm{d}\varepsilon \int \mathrm{d}\cos\theta\,(1-\cos\theta)\,n_\gamma(\varepsilon)\,\frac{\mathrm{d}\sigma_{IC}}{\mathrm{d}E'_\gamma}(E_e, E'_\gamma). \tag{2.21}$$

The differential cross section from equation (2.15) becomes:

$$\frac{\mathrm{d}\sigma_{IC}}{\mathrm{d}E'_\gamma} = \sigma_T\cdot\frac{3}{8}\frac{m_e^2}{s}\frac{1}{E_e}\frac{1+\beta}{\beta}\left[\frac{E_e-E'_\gamma}{E_e}+\frac{E_e}{E_e-E'_\gamma}+\frac{2(1-\beta)}{\beta}\left(1-\frac{E_e}{E_e-E'_\gamma}\right)+\frac{(1-\beta)^2}{\beta^2}\left(1-\frac{E_e}{E_e-E'_\gamma}\right)^2\right]. \tag{2.22}$$

The range that restricts the differential cross section then becomes:

$$0 \le E'_\gamma \le E_e\left(1-\frac{1-\beta}{1+\beta}\right). \tag{2.23}$$

More details on this derivation can be found in Appendix A.2.3.

For the low-energy regime below approximately $E \sim 10^7\,\mathrm{MeV}$, we will approximate the differential interaction rates for the IC process as a Continuous Energy Loss (CEL). For low energies for transitions $i \to i$, we can approximate $\gamma_{i\to i}(E', E)$ by [45]:

$$\gamma(E, E') \approx \delta(E - E' - \langle\Delta E\rangle)\,\Gamma(E). \tag{2.24}$$

Using this approximation, we can substitute the loss and gain term in the Boltzmann equations (1.7) by [45]:

$$-\Gamma(E)\,N_e(E) + \int_E^\infty \mathrm{d}E'\,\gamma(E', E)\,N_e(E') \;\to\; \partial_E(b(E)\,N_e(E)). \tag{2.25}$$

The full derivation of this identity is given in Appendix A.4.

Here we have introduced the continuous energy loss rate: $b(E_i) \equiv \frac{\mathrm{d}E_i}{dt} = E_i\,\Gamma_{loss}(E_i)$, where Γ_{loss} is the energy loss rate from equation (2.17). The motivation behind including the CEL approximation for IC is related to the numerical implementation of the interaction rates and is presented in section 4.1.2.

Chapter 3

UHECR propagation simulation and minimal cosmogenic neutrino fluxes

We will need three different tools to carry out our simulations and analyses in this work. First of all, we will simulate the propagation of primary UHECRs using an open-source Monte Carlo code. Second of all, we will perform a fit of the resulting UHECR particles after propagation to recent cosmic ray data. The fit results allow us to estimate the cosmogenic neutrino flux, as well as the flux of the first generation of electromagnetic particles. Lastly, in chapter 4, we will propagate these electromagnetic particles with our own custom-built Electromagnetic cascade module in order to obtain the γ-ray and electron/positron flux that would reach us at Earth.

The current chapter will present the first two of these tools: the Monte Carlo propagation code and the fitting procedure, together with the results we obtain for UHECRs and cosmogenic neutrinos. The custom-built Electromagnetic cascade module and the results from simulating electromagnetic emission is the subject of the subsequent chapter.

3.1 UHECR propagation simulation

To model the propagation of UHECRs as they travel from extragalactic sources until they reach us at Earth, different simulation tools are available. These include the Monte Carlo codes CRPropa [46, 47, 32, 7] and SimProp [48] as well as the numerical code PriNCe [49].

In this work we use CRPropa 3 which has the additional capabilities of propagating the secondary messengers from UHECRs, namely neutrinos, photons and electrons and positrons that we are interested in. CRPropa 3 has a modular structure as illustrated by Figure 3.1. The code can treat the galactic and extragalactic propagation of the different messengers by simulating their interactions in the background photon fields of CMB, EBL and URB as well as magnetic fields (the latter is, however, outside the scope of the current work).

The overall structure of CRPropa 3

CRPropa 3 works by taking a number of astrophysical inputs such as the source properties and the source distribution. It also takes into account the effects of the cosmological expansion of the universe and the redshift of the particles. A choice of interactions and photon backgrounds, as well as properties of magnetic fields if included, can be defined through which the particles will be propagated. The output of the code is the spectrum of particles and composition of cosmic rays arriving at the top of Earth's atmosphere together with information about their travel distance. These results can then be compared to observations from experiments.

We will refer to CRPropa 3 simply as CRPropa in the following.

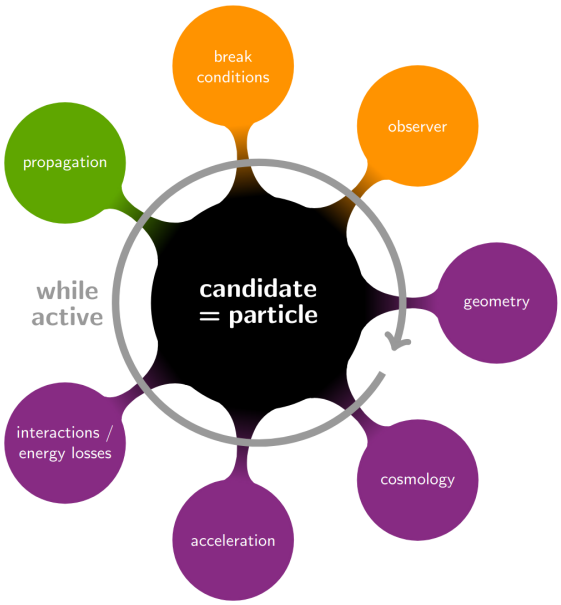

Figure 3.1: CRPropa 3: Overview of modular structure in CRPropa 3. From slides by R.A. Batista [50].

3.2 Simulation setup

For our investigation, two different simulation types are carried out with CRPropa: one using an injection model of pure protons and one using instead a mixed-composition injection from a model defined by a fit to recent UHECR data.

3.2.1 Proton-dominated spectra

Our first case to investigate focuses on a proton-dominated UHECR spectrum. We perform a simulation of 10^7 primary protons with CRPropa with energies from $E_{\min} = 4 \times 10^{19}$ eV to $E_{\max} = 4 \times 10^{21}$ eV with an ad-hoc injection spectrum $\frac{\mathrm{d}N}{\mathrm{d}E} \sim E^{-1}$ so that each energy bin on a logarithmic scale is populated by the same number of particles. We assume the sources to be uniformly distributed from redshift $z_{\min} = 0$ to $z_{\max} = 4$. We use the EBL model from [24] and include all relevant particle interactions as described in chapter 1.1.3: Photo-Pion production, Bethe-Heitler Pair Production, nuclear decay and redshift effects.

The resulting particles are binned in a 4D histogram with bins containing the initial energy of the primary cosmic ray proton E_0, the redshift z for each particle calculated by the comoving distance it has traveled before observation, the observed particle ID number[1] of each (resulting) particle ID (e.g. neutrinos, photons, electrons/positrons, protons), and the observed energy of each particle E_{obs}.

Finally, the 4D histogram is reduced to a 3D histogram that contains the source evolution as a function of initial energy E_0 and redshift z by applying weights:

$$N_w(E_0^j, ID^k, E^l) = \sum_{i=1} \sum_{j=1} w(z^i)\, N(z^i, E_0^j, ID^k, E^l). \tag{3.1}$$

The weights are functions of the redshift and depend on the source evolution model – they are defined in section 3.3 below. The resulting histogram $N_w(E_0^j, ID^k, E^l)$ gives the energy spectrum of each observed particle type as a function of both the initial and observed energy. We need all of this information in order to perform the fit to the UHECR nucleon spectrum as described further down in section 3.3.

[1] The particle ID numbers in CRPropa follow the PDG Monte Carlo numbering scheme: https://pdg.lbl.gov/2012/reviews/rpp2012-rev-monte-carlo-numbering.pdf. They are nuclear codes that have the form: $\pm 10LZZZAAAI$.

Parameter:	Expression:	CTG Global min:
Injection spectral index:	γ	$-1.03^{+0.35}_{-0.30}$
Rigidity cutoff:	$\log_{10}(R_{cut}/V)$	$18.21^{+0.05}_{-0.04}$
Injected nuclei	f_H	68%
fractions:	f_{He}	31%
	f_N	1%
	f_{Si}	0.06%
	f_{Fe}	0%

Table 3.1: Source model parameters: Source parameters and 68% uncertainties from [15] for model **CTG** for the best fit (main minimum) using **C**RPropa, cross sections from **T**ALYS and EBL model **G**ilmore 2012.

3.2.2 Mixed-composition models

For the next part of our analysis, we follow references [51, 15] and simulate UHECRs from uniformly distributed sources located between redshift $z = 0$ and $z = 1$ with energies from $E_{\min} = 10^{17.5}$ eV to $E_{\max} = Z \times 10^{21.5}$ eV, where Z is the charge number of the initial particle type. We include all relevant particle interactions, namely Photo-Pion production, Bethe-Heitler Pair Production, Photodisintegration, nuclear decay and redshift effects. A list of different source models and their fit parameters for fits to recent UHECR spectrum and composition is included in ref. [15]. We focus on the model **CTG**, named as such since it uses **C**RPropa, cross sections from **T**ALYS and the EBL model **G**ilmore 2012 [24]. Our CRPropa simulations use the same settings as the CTG model.

We use a generic population of identical extragalactic sources. We specify their energy spectrum by four different physical parameters: the fraction of nuclei species f_A, spectral index γ and rigidity cutoff $R_{\max}$ make up the first three. The source spectrum is modeled as:

$$J_i(E) = J_0 \; f_{A,i} \; f_{cut}(E_0, Z_{0,i}\, R_{cut}) \left(\frac{E_0^j}{10^{18}\,\mathrm{eV}} \right)^{-\gamma} . \tag{3.2}$$

The last parameter, J_0, is settled by normalising to data from the Pierre Auger Observatory. The cutoff function is defined as:

$$f_{cut}(E_0, Z_{0,i}\, R_{cut}) = \begin{cases} 1 & \text{for} \quad E_0 < Z_{0,i}\, R_{cut} \\ \exp\left(1 - \frac{E_0}{Z_{0,i}\, R_{cut}}\right) & \text{for} \quad E_0 > Z_{0,i}\, R_{cut}. \end{cases} \tag{3.3}$$

It is assumed that sources injecting five different nuclei types i, hydrogen, helium, nitrogen, silicon and iron, are representative of the full range of nuclei species from hydrogen to iron. We simulate the following initial events: $2 \cdot 10^6$ hydrogen (^{1}H) events, $1 \cdot 10^6$ helium (^{4}He) events, $4 \cdot 10^6$ nitrogen (^{14}N) events, $1 \cdot 10^6$ silicon (^{28}Si) events and $2 \cdot 10^6$ iron (^{56}Fe) events. The events follow the distribution used in [15], but do not affect the final results, as the number of events are compensated for in the calculations.

As for the proton-dominated spectrum, the primary events are initially simulated with a spectrum $\frac{\mathrm{d}N}{\mathrm{d}E} \sim E^{-1}$ to get an even amount of events in each energy bin on a logarithmic scale. After propagation we obtain datafiles with information about each particle produced in the propagation, after which we perform post-processing and analysis.

We bin all the generated particles in a histogram with 4 dimensions: the charge number of the initial primary nuclei Z_0, the initial energy of the primary nuclei E_0, the observed ID number of each

(resulting) particle ID, the observed mass number of each particle A_{obs} and the observed energy of each particle E_{obs}. For particles with $A = 0$, we use their particle ID number to separate them into their particle types: neutrinos, photons and electrons/positrons.[2]

We weight the 4D histogram by a set of weights defined by the vector in equation (3.2), where we add $+1$ to the spectral index γ to account for the simulation injection spectrum of $\frac{\mathrm{d}N}{\mathrm{d}E} \sim E^{-1}$. The result is then a 2D histogram $N^{\mathrm{mixed}}_{w,\mathrm{CTG}}$ containing an energy spectrum for each observed mass number A.

$$\text{Histogram of weighted events:} \quad N^{\mathrm{mixed}}_{w,\mathrm{CTG}}(A^k, E^l) = \sum_{i=1}\sum_{j=1} w_{\mathrm{CTG}}(Z^i_0, E^j_0)\, N^{\mathrm{mixed}}(Z^i_0, E^j_0, A^k, E^l). \tag{3.4}$$

We use the parameters from the combined fit of UHECR composition and energy spectrum from [15] listed in table 3.1.

3.3 Fitting procedure

Part of this procedure was presented at the 37th International Cosmic Ray Conference in 2021 [8] and the proceedings are enclosed as Appendix C.

We have simulated ad-hoc initial proton spectra as described in section 3.2.1, and now we wish to adjust the final, propagated spectra to UHECR data for the observed spectrum.

The cosmogenic fluxes from UHECRs with energies above 50 EeV will be dominated by two interactions in particular: pion-production on the CMB and photodisintegration of nuclei.

Since both of these can be approximated as incoherent processes to first order, we can treat the UHECR spectrum as a nucleon spectrum: we can consider interactions of UHECR nuclei with mass number A as an incoherent superposition of interactions of A nucleons, each with energy $E_{\mathrm{N}} = E_{\mathrm{CR}}/A$. If we were to go below 50 EeV, we enter the CR energy domain where the Bethe-Heitler pair-production process dominates. Since this process scales with Z^2 for a nucleus with charge number Z, we can no longer treat the cosmic rays as individual nucleons. As long as we stay at energies above 50 EeV, the production of cosmogenic fluxes will then be determined by the UHECR nucleon spectrum.

According to recent observations from the Pierre Auger Observatory, this high-end part of the cosmic ray spectrum (above $E_{suppr} \sim 46$ EeV) can be described as the power-law $J(E_{\mathrm{CR}}) \propto E^{-\gamma}_{\mathrm{CR}}$ with a spectral index of $\gamma = 5.1 \pm 0.3$ [1]. By considering this observed spectrum as a nucleon spectrum, we can approximate it as:

$$J_{\mathrm{N}}(E_{\mathrm{N}}) \simeq A^{2-\gamma}_{\mathrm{obs}}\, J_{\mathrm{CR}}(50\ \mathrm{EeV}) \left(\frac{E_{\mathrm{N}}}{50\ \mathrm{EeV}}\right)^{-\gamma}, \tag{3.5}$$

where A_{obs} is the observed mass group [52]. This can be approximated as the average observed mass at 50 EeV: $A_{\mathrm{obs}} \approx \langle A_{\mathrm{obs}} \rangle (50\ \mathrm{EeV})$.

By obtaining the composition at high energies from our simulations with CRPropa, we are then able to estimate how the corresponding cosmogenic fluxes scale with the average observed mass number. as was shown in ref. [52]. A heavier observed spectrum will quickly diminish the fluxes by a factor:

$$A^{2-(5.1\pm0.3)}_{\mathrm{obs}} \approx \langle A_{\mathrm{obs}} \rangle^{-3.1\mp0.3}. \tag{3.6}$$

This suppression is a result of the pion-production threshold: heavier nuclei will not have high enough energies to reach the threshold for pion-production and will thus not contribute to the cosmogenic fluxes of neutrinos and γ-rays. This effect is the GZK cutoff described in section (1.1.3).

[2] The dimensions for the ID number and the observed mass number are overlapping; the ID number contains the information of the mass number. We include a small subset of it as a separate dimension in order to separate particles with $A = 0$ into their particle types: neutrinos, photons and electrons/positrons. But instead of using ID numbers for all nuclei and isotopes, we group nuclei by mass numbers only out of memory considerations.

In order to fit the UHECR nucleon spectrum to protons from different source evolutions, we approximate the cosmological evolution of the source density per co-moving volume as:

$$\mathcal{L}_i(z, E) = \mathcal{H}(z)\mathcal{L}_i(0, E) = \mathcal{L}_p(z, E) = \mathcal{H}(z)Q_p(E), \tag{3.7}$$

where $\mathcal{H}(z)$ is the source evolution and $Q_p(E)$ is the source emission spectrum.

We define two cases that we perform separate fits for. First, the "no evolution" case assumes a constant comoving number density of UHECR sources, which we can express as:

$$\mathcal{H}(z) = \mathcal{H}(0) \quad \text{for } 0 \leq z \leq 4. \qquad \text{(no evolution)} \tag{3.8}$$

The other case is the "SFR evolution", where we assume the source evolution to follow the Star Formation Rate based on the model in [53, 45]:

$$\mathcal{H}_{\text{SFR}}(z) = \begin{cases} (1+z)^{3.4} & \text{for } z < 1, \\ 2^{3.7} \cdot (1+z)^{-0.3} & \text{for } 1 < z \leq 4. \end{cases} \qquad \text{(SFR evolution)} \tag{3.9}$$

These cases define the weights $w(z)$ applied to the 4D histogram obtained from CRPropa simulations in equation (3.1) in order to include the source evolution in the fits.

The "no evolution" case provides our most conservative source scenario for the cosmogenic fluxes.

To perform the fit we use the histogram of observed particles that we obtained from a simulation with CRPropa and apply the weights for one of the two cases of source evolution. We then focus on the observed protons only – this means taking the 3D histogram defined in equation (3.1), $N_w(E_0^j, ID^k, E_{\text{obs}}^l)$, and considering only the subset $N_w^p(E_0^j, E_{\text{obs}}^l) \equiv N_w(E_0^j, ID = \text{proton}, E_{\text{obs}}^l)$. This forms a square matrix $\bar{N} \equiv \left(N_w^p(E_0^j, E_{\text{obs}}^l)\right)^\intercal$ with the observed energy on one axis and the initial energy on the other axis:

$$\bar{N} = \begin{bmatrix} N(E_{\text{obs},0}, E_{0,0}) & 0 & 0 & \dots \\ N(E_{\text{obs},1}, E_{0,0}) & N(E_{\text{obs},1}, E_{0,1}) & 0 & \dots \\ N(E_{\text{obs},2}, E_{0,0}) & N(E_{\text{obs},2}, E_{0,1}) & N(E_{\text{obs},2}, E_{0,2}) & \dots \\ \vdots & \vdots & \vdots & \ddots \end{bmatrix}. \tag{3.10}$$

We use the CR fit from [2] that parameterises the Pierre Auger UHECR data to define a vector: $\vec{N}_{\text{PA}}(E_{\text{obs}}) \equiv J_{\text{PA}}(E_{\text{obs}})\, E_{\text{obs}}$. This vector then contains the UHECR nucleon data that we want to fit to as a function of observed energy, in units of flux times energy.

We perform the fit of our initial proton spectrum to the UHECR nucleon data by solving the matrix equation below to get the injection spectrum weights $\vec{Q}(E_0)$:

$$\bar{N}(E_{\text{obs}}, E_0) \cdot \vec{Q}(E_0) = \vec{N}_{\text{PA}}(E_{\text{obs}}). \tag{3.11}$$

The matrix equation is solved using the Python package Numpy. The injection spectrum weights $\vec{Q}(E_0)$ are then applied to our proton spectrum and to the corresponding cosmogenic fluxes.

3.4 Results for UHECRs and cosmogenic neutrinos

Our aim with this work is to study the secondary emission from UHECRs in the form of cosmogenic neutrinos, photons and electrons and the cascade emission from the latter two. From this study we can estimate the minimal cosmogenic fluxes.

The strategy for obtaining the minimal flux predictions is to perform a fit to the UHECR nucleon spectrum and obtain the prediction for cosmogenic fluxes for the case of proton-dominated source emission. The cosmogenic neutrinos function as good probes for UHECRs due to their unperturbed journey from the sources to observation at Earth, so we can use observations of UHECRs to predict the corresponding flux of cosmogenic neutrinos and — should we detect cosmogenic neutrinos — vice versa.

As the cosmogenic fluxes are intrinsically linked to the UHECR source models, the predictions we obtain will be strongly model-dependent. We consider in the following different model uncertainties: the evolution of the sources with redshift and the composition of the UHECR spectrum.

In this section we will begin by presenting our results for estimation of the cosmogenic neutrino flux. From a fit to the UHECR nucleon spectrum we show our prediction for the minimal cosmogenic neutrino flux and consider the effect of the source evolution model. We can compare our predictions with the sensitivities from future experiments and use this to estimate our prospects for measuring the cosmogenic neutrino flux. Part of this analysis was presented at the 37th International Cosmic Ray Conference in 2021 [8] and the proceedings are enclosed as Appendix C.

The minimal cosmogenic flux limits depend on the observed UHECR mass composition. Next, we will therefore consider the a mixed-composition UHECR scenario and the effects that a heavier composition will have on the cosmogenic fluxes.

We use our results from this section in the following chapter, where we show the resulting cascades from propagation of the proton spectrum generated by simulations with CRPropa as well as of generic electromagnetic spectra.

3.4.1 Proton dominated spectra and source evolution

Our simulation of the propagation of UHECR protons in CRPropa, as described in section 3.2.1, is fitted to the UHECR spectrum from the Pierre Auger Observatory above 50 EeV with the method presented in section 3.3.

Figure 3.2 shows our fit of protons (black line) to the Pierre Auger CR fit (green dashed line) from [1, 2] of the all-particle UHECR spectrum. The shaded bands in the figure come from the 68% statistical uncertainties from the Pierre Auger CR fit. The corresponding cosmogenic fluxes are shown in the red band for neutrinos, in the blue band for unattenuated γ-rays and in the orange band for electrons/positrons. Both of the latter components represent only the first generation of EM particles from the UHECRs – they will subsequently initiate electromagnetic cascades on the photon backgrounds (CMB, EBL and URB) that will create cascade emissions in the GeV-TeV range. We will return to the results from the cascades by using our own EM Cascade module in section 4.5 below.

When the UHECR sources follow an evolution given by the Star Formation Rate [53, 45] (right panel of figure 3.2), their resulting cosmogenic fluxes become a factor 5 larger than the "no evolution" case (left panel of figure 3.2).

Comparison with sensitivity limits

The cosmogenic neutrino fluxes that we get from the two different source evolution models in figure 3.2 are compared to the ranges of current and future detectors in figure 3.3. We show the neutrino upper limits from the IceCube detector [54] and the Pierre Auger Observatory [55] in addition to the sensitivities from the two future neutrino detector experiments IceCube-Gen2[3] [33] and GRAND200k[4] [56]. The figure demonstrates that the next-generation neutrino observatories will be able to detect the cosmogenic neutrino flux in the EeV range that will scale with the factor in equation (3.6). If we compare the neutrino fluxes to the sensitivity limits, we see that a proton contribution of 10% gives measurable fluxes for the no evolution case, and correspondingly having a proton contribution of at least 2% gives measurable fluxes for the SFR evolution case.

3.4.2 Mixed-composition spectra

As a way to investigate the UHECR source model uncertainty we simulate a mixed-composition model based on a combined fit to recent UHECR spectrum and composition data from the Pierre Auger Observatory [15]: the CTG model presented in section 3.2.2.

[3] IceCube-Gen2 is an enhancement of the current IceCube observatory at the South Pole that combines an 8 km^3 Cherenkov light detector array with a 500 km^2 radio array, expected to be fully operational by 2033 [33].

[4] The GRAND200k is a radio antenna array with a total area of 200,000 km^2 for air-shower detection of UHECRs, neutrinos and γ-rays, expected to be completed in the 2030s [56].

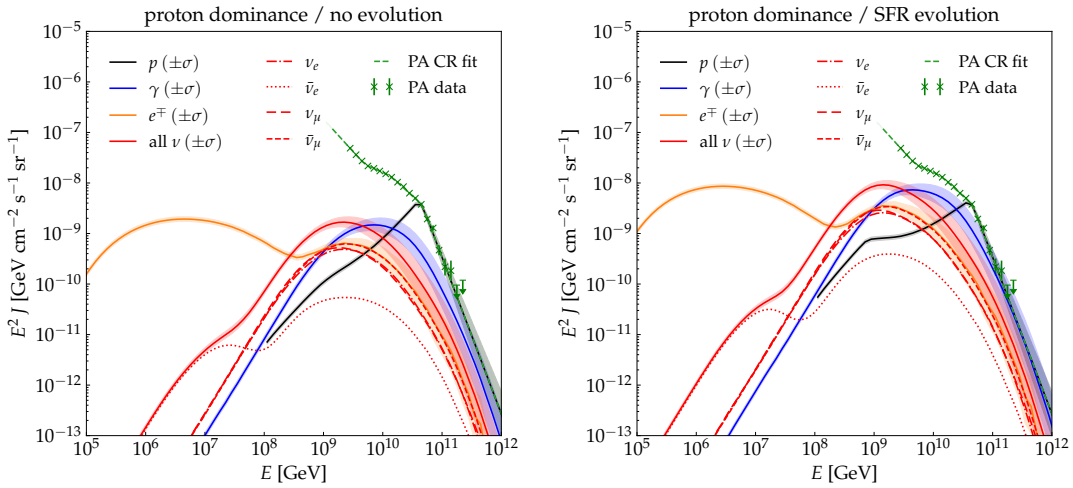

Figure 3.2: Proton dominated spectra. Cosmogenic neutrino, electron/positron and γ-ray fluxes from UHECR dominated by protons above 50 EeV including 68% statistical uncertainties from the CR fit (green dashed line). Our fit of the proton flux (black line) to the CR fit from the Pierre Auger Observatory of the all-particle spectrum [1, 2] (green points) is shown assuming two different source evolution models. Contributions from individual neutrino flavours on production are shown as red dashed, dotted and dash-dotted lines that sum up to the all-flavour flux given by the solid red line. *Left:* The "no evolution" case assumes a constant comoving number density of sources. *Right:* The source evolution follows the Star Formation Rate in [53, 45].

We simulate the model with CRPropa using the method described in section 3.2.2. Figure 3.4 shows the results for the UHECR spectra from the CTG model at the top of Earth's atmosphere grouped by the observed mass number A_o. The four groupings correspond to the ones presented in [15]. The total UHECR spectrum from the CTG model is shown in orange, the sum of all the mass groupings. We see a deficit of data in the energies above 10^{20} eV that is caused by a lack of Monte Carlo statistics due to limited resources for the CRPropa simulation that does not affect the analysis.

From this source model, we obtain the average value $\langle A_o \rangle$ at the energy $E = 50$ EeV:

$$\langle A_o \rangle (50\ \text{EeV}) = 21.3. \tag{3.12}$$

3.4.3 Cosmogenic fluxes reweighted by A_o

A heavier UHECR spectrum will produce a lower cosmogenic neutrino flux since the energy threshold for pion-production of nucleons scales with mass number: $\frac{E_{CR}}{A} > E_{th}$. For this reason, many CRs will not reach the pion-production threshold which causes a strong suppression of the cosmogenic neutrino flux.

Using the average observed mass number from equation (3.12), we can reweight the proton spectrum and corresponding cosmogenic neutrino flux by the scale factor $\langle A_{obs}^{2-\gamma} \rangle$, as described in section 3.3. With a value for $\langle A_o \rangle$ of 21.3, the scaling factor will reduce the flux by:

$$\langle A_{obs} \rangle^{2-\gamma} = 21.3^{2-(5.1\pm0.3)} \approx 0.008\%. \tag{3.13}$$

The results from the rescaling are presented in figure 3.5 (blue and purple lines for nucleons and neutrinos respectively) together with the original predictions from a pure proton case (black and red lines for protons and neutrinos respectively).

The fluxes in the figure demonstrate the expected suppression by mass number scaling. The rescaled neutrino flux represents a conservative lower limit as the UHECR emission spectrum is limited to energies of 50 EeV and above.

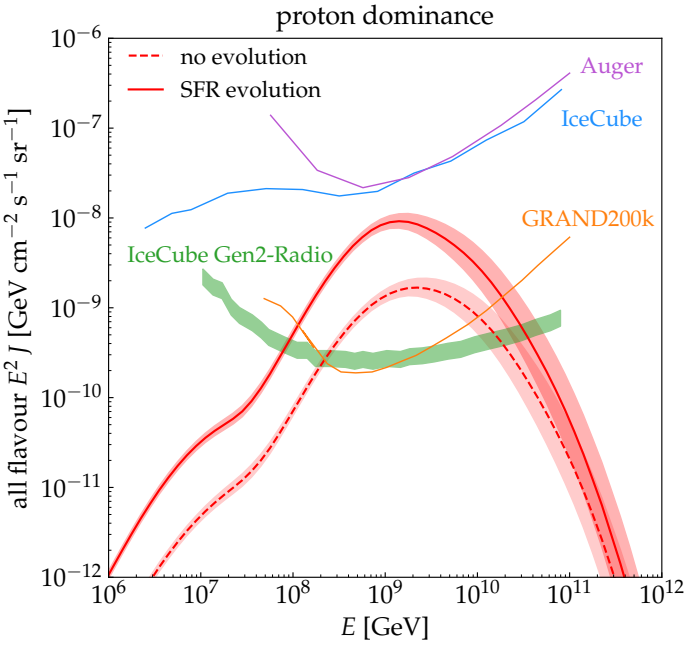

Figure 3.3: Cosmogenic neutrino fluxes. The cosmogenic neutrino fluxes from UHECRs dominated by protons above 50 EeV from two different course evolution models: the "no evolution" case (dashed red line) assumes a constant comoving source number density, whereas the "SFR evolution" case (solid red line) uses the source density evolution modeled by the star formation rate in [53, 45]. The cosmogenic fluxes from both models are consistent with sensitivity limits from the two current experiments, IceCube [54] and Pierre Auger Observatory [55], as well as within the range of the two future experiments IceCube Gen2-Radio [33] and GRAND200k [56]. Presented at the 37th International Cosmic Ray Conference [8] – enclosed as Appendix C.

Next, we compare our rescaled cosmogenic neutrino flux to the original neutrino prediction from CRPropa.

Figure 3.6 shows the lower limit on the cosmogenic neutrino flux (in purple) from the mixed composition described by the CTG model compared to the prediction for the same model from CRPropa (in blue). Our limit undershoots the CRPropa prediction, by e.g. ~ 4 orders of magnitude at $E \sim 10^8$ GeV, and thus proves to be a very conservative lower limit – arguably too conservative to be very useful. When comparing the limit to the prediction is it important to note that our fit only considers energies from 50 EeV and onwards, meaning that CR interactions with the EBL are left out. These are present in the CRPropa calculation, which necessarily leads to a larger cosmogenic neutrino flux prediction in the sub-EeV range ($E < 10^9$ GeV).

Furthermore, the figure shows that our cosmogenic neutrino limit continues at higher energies beyond the prediction from CRPropa. This is related to the fact that our injection spectrum used for the limit does not include any cut-off at higher energies such as the cutoff function in equation (3.3).

It is worth noting that the cosmogenic neutrino flux shown here is conservative also in its choice of source evolution model. Including source evolution following the Star Formation Rate or other evolution models would increase the predicted cosmogenic neutrino fluxes.

The cosmogenic neutrino fluxes found for the proton dominated case agree well with the minimal cosmogenic neutrino fluxes in ref. [52] for both the case of no evolution and of SFR evolution.

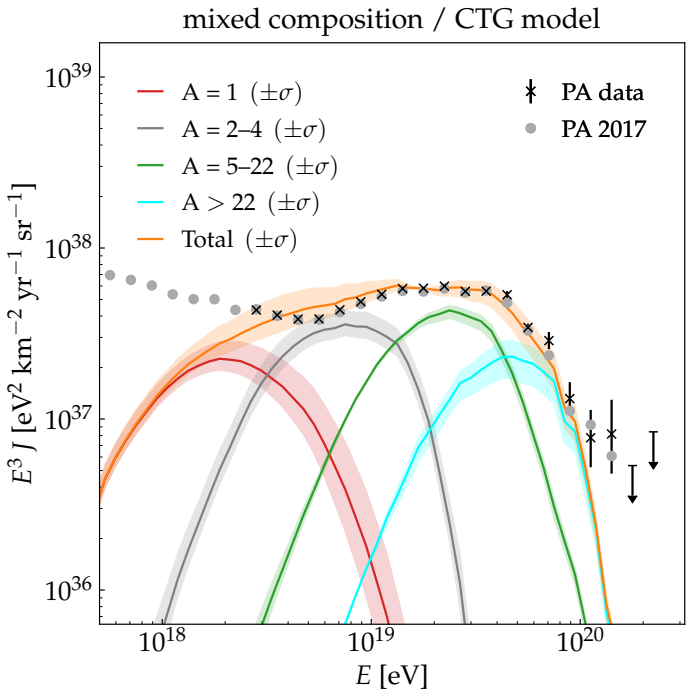

Figure 3.4: Mixed-composition spectra. The UHECR spectrum at the top of Earth's atmosphere including 68% uncertainties from a source model with parameters listed in table 3.1 (with spectral index $\gamma = -1.03^{+0.35}_{-0.30}$ and rigidity cutoff: $\log_{10}(R_{cut}/V) = 18.21^{+0.05}_{-0.04}$). The spectrum is grouped by observed mass number A for four different groupings, and the orange line shows the total UHECR spectrum, i.e. the sum of all four groupings. Also shown are the data from the Pierre Auger Observatory [38, 57] used to obtain the fit in [15] together with updated data from the Pierre Auger Observatory [1, 2].

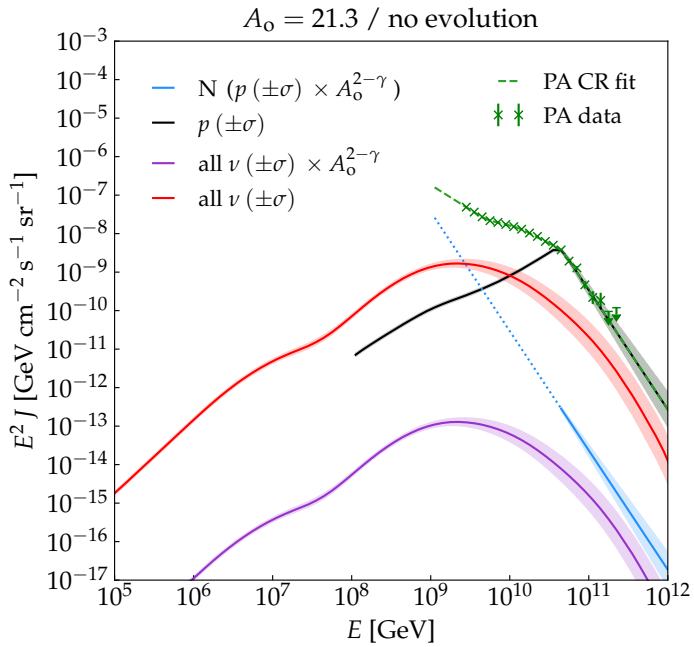

Figure 3.5: Spectra rescaled by A_o. The proton-dominated CR spectrum (in black) compared to the mixed-composition nucleon spectrum rescaled by the average observed mass number (in blue) from the CTG model in equation (3.12). The resulting cosmogenic neutrino fluxes are shown in red (proton case) and purple (mixed-composition case) respectively. Recent data from the Pierre Auger Observatory and a corresponding fit from [1, 2] are shown in green.

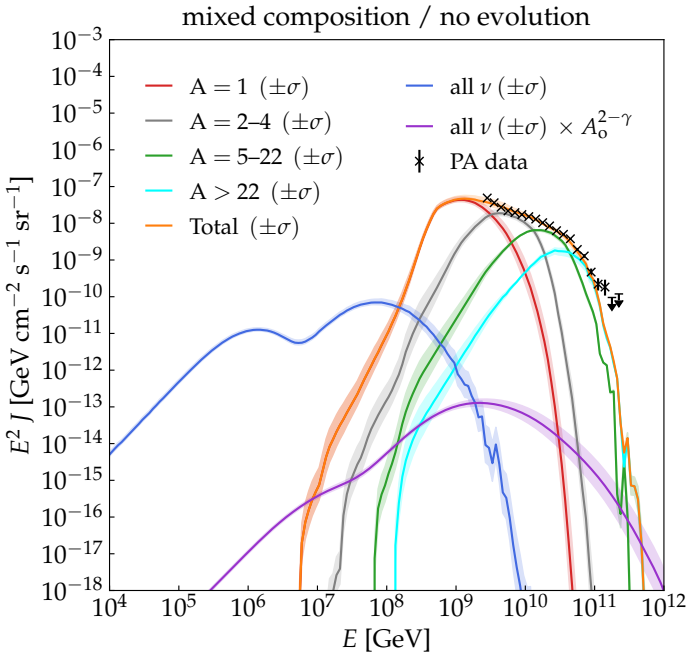

Figure 3.6: Mixed-composition spectra and neutrinos. The UHECR spectrum from the CTG source model in figure 3.4 with the predicted cosmogenic neutrino flux from simulation with CRPropa (in blue) compared to the minimal cosmogenic neutrino flux prediction (in purple). Recent data from the Pierre Auger Observatory are shown in black [1, 2].

Chapter 4

Electromagnetic cascades simulation

Monte Carlo methods (like CRPropa) in principle require tracking every particle. With electromagnetic cascades large quantities of particles are generated, and tracking them all becomes computationally expensive.

An alternative to Monte Carlo codes is to use the spectra from CRPropa as the initial spectra and then develop their resulting electromagnetic cascades with our own code based on numerical solution of the Boltzmann equations for the secondary particles: electrons, positrons and photons.

The method we present here is based on the matrix doubling method from [58] and [23] and developed further in [40]. The basis for this method is to define a set of transfer matrices that describe gains and losses for the spectra of secondary particles as they propagate through space and interact with the photon backgrounds. With the matrix doubling method, we can develop the cascades over very large distance scales while calculating interaction lengths for the interaction processes on very small scales.

In the present chapter we well first describe the motivation behind building our own module for computing the electromagnetic cascades, before we turn to the custom-built Electromagnetic cascade module itself.

Monte Carlo vs numerical approach for EM cascades

Being a Monte Carlo code, the CRPropa simulation tracks each individual particle through its journey from the source to Earth, as well as each individual secondary particle created in interactions along the way. This can become expensive computationally, both memory-wise and time-wise.

This is less of a problem if we only consider the first generation of particles to be created in interactions with the background photon fields, i.e. neutrinos, photons and electrons/positrons as well as secondary nuclei created through photodisintegration of the primary nuclei. Whereas the neutrinos and secondary nuclei will continue to propagate largely unhindered by any other type of interactions, this is not the case for the electromagnetic (EM) particles. These will undergo electromagnetic cascades on the photon backgrounds that will create huge numbers of second-generation photons and electrons/positrons. Tracking all of these electromagnetic particles puts a large strain on the required memory resources as they quickly produce datafiles of many GBs even for relatively small numbers of primary particles (e.g. $N \sim 10^4$), as also described in [29]. The computations of the electromagnetic cascades with CRPropa are also costly time-wise; as a quick example, tracking 10^7 initial γ-rays cascading on the CMB from sources 800 Mpc away, as we do with our own EM module in chapter 2, would take an estimated 227 hours to finish and would generate enormously large datafiles.

The simulation of electromagnetic cascades have up until and including CRPropa version 3.1.6 (which is the version used for this thesis) been handled by the external codes DINT, a transport-equation solver, for lower energy EM particles and EleCa, a Monte Carlo code, for higher energy EM particles. Both of the two codes have only a small selection of photon backgrounds to choose from

and are thus incompatible with many of the choices of newer photon backgrounds otherwise available in CRPropa 3.

These two aspects, computational requirements and limited photon backgrounds, are both impedimental to our objective of studying the cosmogenic fluxes from UHECRs. Since we are interested in the high-energy particles from large enough source numbers to get good Monte Carlo statistics and, at the same time, in using the new and updated models for the EBL and radio photon backgrounds, we have chosen to develop our own numerical electromagnetic cascade simulation code. This code is to be combined with the resulting first generation of particles mentioned above from CRPropa.

During the course of this work, a new version of CRPropa 3 was released: version 3.1.7 in February 2021 [59], that was updated to now include native CRPropa Monte Carlo modules for propagation of the EM particles in electromagnetic cascades. A thinning module was implemented to handle the copious amounts of secondary EM particles to be tracked and stored by the code. However, due to a subsequently discovered bug in the implementations of the background photon fields (see ticket #340 on the GitHub page [7]) that especially affects cosmogenic neutrinos, version 3.1.7 was not taken into use for this work. An upcoming release of CRPropa, version 3.2, was presented at the 37th International Cosmic Ray Conference in July 2021 and is expected to resolve the aforementioned bug as well as introduce a new range of extensions to the code [60].[1]

While the new releases present a method of getting around the two aspects mentioned above, there are both advantages and disadvantages compared to using a numerical solver like the one outlined in this work. The method of thinning can be said to introduce new uncertainties into the calculations and the Monte Carlo handling of EM cascades remains computationally expensive/time-consuming. For this reason, we believe a numerical solver can provide a useful counterpart to the Monte Carlo approach for EM cascades.

4.1 Matrix equation setup

We follow the method of matrix doubling outlined in [58, 23] and [40] to transform the set of Boltzmann equations to a matrix equation. We start from the two equations for the comoving number densities of photons and electrons/positrons given by equations (2.1) and (2.2).

4.1.1 Discretisation

Time discretisation

We begin our steps towards discretising the equations by expressing the time-derivate as:

$$\frac{\partial n}{\partial t} = \frac{n(t+\Delta t) - n(t)}{\Delta t}, \tag{4.1}$$

where the time step is Δt. Using this on our equations for photons and electrons in (2.1) and (2.2), we get:

$$n_\gamma(E, t+\Delta t) = n_\gamma(E,t) - \Delta t\, \Gamma_{PP}(E)\, n_\gamma(E,t) + \Delta t \int \mathrm{d}E_e\, \gamma^{IC}_{e\to\gamma}(E_e, E)\, n_e(E_e, t), \tag{4.2}$$

$$n_e(E, t+\Delta t) = n_e(E,t) - \Delta t\, \Gamma_{IC}(E)\, n_e(E,t) + \Delta t \int \mathrm{d}E_\gamma\, 2\,\gamma^{PP}_{\gamma\to e}(E_\gamma, E)\, n_\gamma(E_\gamma, t) + \Delta t \int \mathrm{d}E_e\, \gamma^{IC}_{e\to e}(E_e, E)\, n_e(E_e, t). \tag{4.3}$$

For the time step Δt, we choose a maximum distance appropriate in relation to the relevant scale of interaction lengths: $\Delta x = 0.1$ kpc, and convert to a time step in natural units by:

$$\Delta t = \frac{\Delta x}{\hbar \cdot c} = 0.1\,\mathrm{kpc} \cdot \frac{3.086 \times 10^{19}\,\mathrm{m}}{\mathrm{kpc}} \cdot \frac{1}{\hbar \cdot c} = 1.564 \times 10^{31}\,\mathrm{MeV}^{-1}.$$

[1] As of mid-August 2021, the new version has yet to be officially released.

The choice of 0.1 kpc comes from the dip of the interaction lengths on the CMB at around 10 kpc as seen in figure 2.2 and down to around 1 kpc at seen in figure 2.3. In other words, we want to make sure that all calculations use a time step that is shorter than 1 to 10 kpc.

Energy discretisation and matrix doubling

We are interested in the energy range from ~ 1 GeV to 1000 EeV, i.e. $\sim 10^3$ MeV to 10^{15} MeV, for the initial particle energy spectra.

To discretise the energy, we divide the energy range into logarithmic bins. In this way we get energy bins of equal width on a logarithmic scale. Deciding the resolution for the energy grid, i.e. the width of the logarithmic energy bins, is a balance between computational efforts on one side and precision on the other. The finer the resolution of the energy grid, the less effect on the computations due to the finite bin size, but at the price of increased computational resources. We find that a resolution with an energy bin width of $\Delta \log_{10} E = 0.05$ is satisfactory on both parameters.

For our discretised spectra, we can relate the number of particles N in a logarithmic energy bin to the flux $J(E)$ by:

$$\begin{aligned} J(E) = \partial_E N = \frac{\partial N}{\partial E} &\simeq \frac{\Delta N}{\Delta E} \\ &= \frac{\partial \log_{10} E}{\partial E} \frac{\partial N}{\partial \log_{10} E} = \frac{1}{E} \frac{\partial N}{\partial \log_{10} E} \simeq \frac{1}{E} \frac{\Delta N}{\Delta \log_{10} E}. \end{aligned} \tag{4.4}$$

In the last expression, the denominator $\Delta \log_{10} E$ is determined by the choice of bins in the energy grid, and when the flux is normalised to data in the end, this constant will simply be absorbed by the normalisation.

We approximate the integrals in (4.2) and (4.3) by Riemann sums with an integration over one energy bin of the outgoing energy:

$$\int \mathrm{d}E_j \ \gamma(E_j, E_i) \quad \simeq \quad \sum_j \Delta E_j \ \frac{1}{\Delta E_i} \int_{E_{i,L}}^{E_{i,R}} \mathrm{d}E_i \ \gamma(E_j, E_i) \simeq \quad \sum_j \frac{\Delta E_j}{\Delta E_i} \bar{\gamma}(E_j, E_i), \tag{4.5}$$

where we define:

$$\bar{\gamma}(E_j, E_i) \quad \equiv \quad \int_{E_{i,L}}^{E_{i,R}} \mathrm{d}E_i \ \gamma(E_j, E_i), \tag{4.6}$$

and where $E_{i,L}$ designates the left bin-edge of the energy bin i, so that E_i is the center of the bin. Likewise, $E_{i,R}$ is the right bin-edge of the energy bin i. The extra factor $\frac{1}{\Delta E_i}$ makes up for the binwise-integration over the outgoing energy.

The integration over one energy bin gives a more precise approximation for the integral over $\gamma^{IC}_{e\to e}(E_j, E_i)$ than the Riemann sums can provide. The derivation of the Boltzmann equations for the one-bin integrated differential interaction rates is presented in detail in Appendix B.1.1.

We define:

$$N_{\gamma,i} \simeq \Delta E_i \ n_\gamma(E_{\gamma,i}), \tag{4.7}$$

$$N_{e,i} \simeq \Delta E_i \ n_e(E_{e,i}). \tag{4.8}$$

With this we transform equations (4.2) and (4.3) by multiplying with ΔE_i and reach the final discretised equations:

$$N_{\gamma,i}(t + \Delta t) \simeq N_{\gamma,i}(t) - \Delta t \, \Gamma^{PP}_{\gamma,i} \, N_{\gamma,i}(t) + \Delta t \sum_j \bar{\gamma}^{IC}_{e\to\gamma;ji} \, N_{e,j}(t), \tag{4.9}$$

$$N_{e,i}(t + \Delta t) \simeq N_{e,i}(t) - \Delta t \, \Gamma^{IC}_{e,i} \, N_{e,i}(t) + \Delta t \sum_j \bar{\gamma}^{IC}_{e\to e;ji} \, N_{e,j}(t) + \Delta t \sum_j 2 \, \bar{\gamma}^{PP}_{\gamma\to e;ji} \, N_{\gamma,j}(t). \tag{4.10}$$

These equations form the basis of our treatment of the electromagnetic cascades as they describe the evolution of the spectra on short timescales. In order to connect these short timescales to propagation

over cosmological distances, we follow [58, 23, 40] and implement the equations by splitting them into the four upper-triangular[2] transfer matrices:

$$[T_{\gamma\gamma}(\Delta t)]_{ji} \equiv \left(1 - \Delta t \ \left[\Gamma_{\gamma}^{PP}\right]_i\right) \delta_{ji}, \tag{4.11}$$

$$[T_{e\gamma}(\Delta t)]_{ji} \equiv \Delta t \ \left[\bar{\gamma}_{e\to\gamma}^{IC}(E_j, E_i)\right], \tag{4.12}$$

$$[T_{\gamma e}(\Delta t)]_{ji} \equiv \Delta t \ \left[2\,\bar{\gamma}_{\gamma\to e}^{PP}(E_j, E_i)\right], \tag{4.13}$$

$$[T_{ee}(\Delta t)]_{ji} \equiv \left(1 - \Delta t \ \left[\Gamma_{e}^{IC}\right]_i\right) \delta_{ji} \ + \ \Delta t \ \left[\bar{\gamma}_{e\to e}^{IC}(E_j, E_i)\right]. \tag{4.14}$$

With these transfer matrices, we can write the equations for the evolution of spectra of photons and electrons as a matrix equation:

$$\begin{bmatrix} N_\gamma \\ N_e \end{bmatrix}_i (\Delta t) \simeq \sum_j \begin{bmatrix} T_{\gamma\gamma}(\Delta t) & T_{e\gamma}(\Delta t) \\ T_{\gamma e}(\Delta t) & T_{ee}(\Delta t) \end{bmatrix}_{ji} \begin{bmatrix} N_\gamma \\ N_e \end{bmatrix}_j (0). \tag{4.15}$$

Taking another time step Δt is equivalent to squaring the original four transfer matrices:

$$\begin{bmatrix} N_\gamma \\ N_e \end{bmatrix}_i (2\Delta t) \simeq \sum_j \begin{bmatrix} T_{\gamma\gamma}(\Delta t) & T_{e\gamma}(\Delta t) \\ T_{\gamma e}(\Delta t) & T_{ee}(\Delta t) \end{bmatrix}^2_{ji} \begin{bmatrix} N_\gamma \\ N_e \end{bmatrix}_j (0). \tag{4.16}$$

We generalise this procedure by combining the four original transfer matrices into one transition matrix $\mathcal{T}(\Delta t)$:

$$\mathcal{T}(\Delta t) \equiv \begin{bmatrix} T_{\gamma\gamma}(\Delta t) & T_{e\gamma}(\Delta t) \\ T_{\gamma e}(\Delta t) & T_{ee}(\Delta t) \end{bmatrix}. \tag{4.17}$$

To compute the fluxes N_γ and N_e after the time interval $2^n\,\Delta t$, we square $\mathcal{T}(\Delta t)$ iteratively n times, so we get:

$$\begin{bmatrix} N_\gamma \\ N_e \end{bmatrix} (2^n\,\Delta t) \simeq \left[\left[\left[\left[\mathcal{T}(\Delta t)\right]^2 \right]^2 \right]^{2\cdots} \right]^2 \begin{bmatrix} N_\gamma \\ N_e \end{bmatrix} (0). \tag{4.18}$$

In this way, we can use the squaring of the transition matrix $\mathcal{T}(\Delta t)$ to efficiently propagate the EM particles and develop their cascades over long distances.

The reader is referred to Appendix B.1.2 for further details on the matrix multiplication method and the full derivation of equation (4.18).

The matrix doubling method allows us to develop the cascades over light-travel distances d_{travel} cf. equation (1.5) as a function of the chosen Δt. For a given distance to a source, we find the corresponding minimum number $n_{\min}$ of matrix doublings needed to reach the distance for the upper limit of $\Delta t_{\max} = 0.1$ kpc. We next use this $n_{\min}$ to calculate the value of Δt required to propagate the chosen distance with high precision:

$$\begin{aligned} d_{travel} &= 2^{n_{\min}}\,\Delta t_{\max} \quad \Rightarrow \\ n_{\min} &= \left\lceil \log_{10}\left(\frac{d_{travel}}{\Delta t_{\max}}\right) / \ \log_{10}(2) \right\rceil \quad \Rightarrow \\ \Delta t &= \frac{d_{travel}}{2^{n_{\min}}}. \end{aligned} \tag{4.19}$$

[2] All differential interaction rates $\bar{\gamma}(E_j, E_i)$ are assumed to be matrices with dimensions of E_i on the first axis and E_j on the second axis in the definitions of the transfer matrices given here.

Numerical computation of interaction rates

We use the integration methods from the Python package SciPy to obtain all total interaction rates Γ^{IC}, Γ^{PP} as well as the one-bin integrated differential interaction lengths $\bar{\gamma}^{IC}_{e\to e}$, $\bar{\gamma}^{IC}_{e\to\gamma}$ and $\bar{\gamma}^{PP}_{\gamma\to e}$, and finally the energy loss length $\Gamma^{IC}_{\text{loss}}$.

All rates are calculated separately for each of the three photon background fields CMB, EBL and URB.

The differential Inverse Compton scattering interaction rate for outgoing electrons, $\bar{\gamma}^{IC}_{e\to e}$, suffers from numerical instabilities at lower energies as a result of the finite resolution of the energy grid. An additional normalisation is applied for this interaction rate, before it is combined with the Continous Energy Loss Approximation described in the section below:

$$\tilde{\gamma}^{IC}_{e\to e}(E_i, E_j) = \frac{\Gamma^{IC}(E_i)\cdot\bar{\gamma}^{IC}_{e\to e}(E_i, E_j)}{\sum_j \bar{\gamma}^{IC}_{e\to e}(E_i, E_j)}. \tag{4.20}$$

4.1.2 CEL approximation in the matrix doubling method

The numerical computation of the differential interaction rates for Inverse Compton scattering on the CMB is affected by finite resolution of the energy grid. For this reason, the integrated IC differential interaction rate $\gamma^{IC}_{e\to e}(E, E')$ does not match the total IC interaction rate at lower energies of the computation with CMB, as shown in figure B.2 in the Appendix chapter on the CEL approximation. In other words, the differential interaction rates do not fulfill the relation $\int \mathrm{d}E'\gamma^{IC}_{e\to e}(E, E')\,\mathrm{d}E' = \Gamma^{IC}(E)$ for lower energies.

This has the effect of creating unphysical results at lower energies for particles, when these differential interaction rates are used in the transfer matrices.

We solve this issue by introducing the Continuous Energy Loss approximation for the lower-energy regime of the Inverse Compton scattering interaction rates Γ_{IC} and $\gamma^{IC}_{e\to e}$.

We use the approximation from equation (2.25):

$$\partial_t n_e = -\Gamma_{IC}\, n_e + \int \mathrm{d}E_e\, \gamma^{IC}_{e\to e}(E_e, E'_e)\, n_e(E_e) \;\simeq\; \partial_E(b(E)\cdot n_e). \tag{4.21}$$

For the energy loss parameter b, we use the energy loss length Γ^{IC}_{loss} for Inverse Compton scattering:

$$\begin{aligned} \Gamma_{loss}(E_e) &= \frac{1}{E_e}\frac{\mathrm{d}E_e}{\mathrm{d}t} \quad \Rightarrow \\ b(E_i) \equiv \frac{\mathrm{d}E_i}{dt} &= E_i\,\Gamma_{loss}(E_i). \end{aligned} \tag{4.22}$$

We describe the implementation of the Continuous Energy Loss approximation with a forward difference method as well as the numerical implementation in Python in detail in Appendix B.2.

We use a forward difference on the time derivative and for the energy derivative, defined as follows:

$$\begin{aligned} \partial_t u &\approx \frac{u^{n+1}_j - u^n_j}{\Delta t} \\ \partial_E u &\approx \frac{u^n_{j+1} - u^n_j}{E_{j+1} - E_j} \end{aligned} \tag{4.23}$$

Implementing these, the matrix equation for the CEL approximation for Inverse Compton scattering can be expressed as:

$$\begin{aligned} \partial_t n_e &\simeq \partial_E(b(E)\cdot n_e) \\ \frac{n_e(t+\Delta t) - n_e(t)}{\Delta t} &\simeq \frac{b(E_{i+1})n(E_{i+1}) - b(E_i)n(E_i)}{E_{i+1} - E_i} \quad \Rightarrow \\ N_i(\Delta t) &= \left[1 - \Delta t\frac{E_i}{E_{i+1} - E_i}\,\Gamma^{IC\,loss}_i\right] N_i(0) + \Delta t\frac{\Delta E^{bin}_i}{\Delta E^{bin}_{i+1}}\frac{E_{i+1}}{E_{i+1} - E_i}\,\Gamma^{IC\,loss}_{i+1}\,N_{i+1}(0). \end{aligned} \tag{4.24}$$

By writing the CEL approximation as a transfer matrix $T_{ee,CEL}$, we can define a new CEL transition matrix $\mathcal{T}_{CEL}(\Delta t)$ that replaces T_{ee} by its CEL counterpart:

$$[T_{ee,CEL}(\Delta t)] \equiv \begin{bmatrix} 1 - \frac{\Delta t\, E_0}{E_1 - E_0}\,\Gamma_0^{IC\,loss} & \frac{\Delta E_0^{bin}}{\Delta E_1^{bin}}\frac{\Delta t\, E_1}{E_1 - E_0}\,\Gamma_1^{IC\,loss} & 0 & 0 & \dots \\ 0 & 1 - \frac{\Delta t\, E_1}{E_2 - E_1}\,\Gamma_1^{IC\,loss} & \frac{\Delta E_1^{bin}}{\Delta E_2^{bin}}\frac{\Delta t\, E_2}{E_2 - E_1}\,\Gamma_2^{IC\,loss} & 0 & \dots \\ 0 & 0 & 1 - \frac{\Delta t\, E_2}{E_3 - E_2}\,\Gamma_2^{IC\,loss} & \frac{\Delta E_2^{bin}}{\Delta E_3^{bin}}\frac{\Delta t\, E_3}{E_3 - E_2}\,\Gamma_3^{IC\,loss} & \dots \\ 0 & 0 & 0 & 1 - \frac{\Delta t\, E_3}{E_4 - E_3}\,\Gamma_3^{IC\,loss} & \dots \\ \vdots & \vdots & \vdots & \vdots & \ddots \end{bmatrix}, \tag{4.25}$$

$$\mathcal{T}_{CEL}(\Delta t) \equiv \begin{bmatrix} T_{\gamma\gamma}(\Delta t) & T_{e\gamma}(\Delta t) \\ T_{\gamma e}(\Delta t) & T_{ee,CEL}(\Delta t) \end{bmatrix}. \tag{4.26}$$

4.1.3 Interpolating between the exact calculation and the CEL approximation

Armed with our new CEL transition matrix $\mathcal{T}_{CEL}(\Delta t)$, we are now able to describe the Inverse Compton scattering process also for lower energies without running into the issues of unphysical results.

As this approximation applies for *lower energies* only, we need to settle two aspects: which part of the energy range it should be implemented on and how we wish to transition from the exact calculation at higher energies to the CEL approximation at lower energies.

Determining the critical energy

We seek to define a critical energy E_{crit} that specifies the limit where we change from the exact calculation to the CEL approximation.

We shall define this energy when the typical loss of energy becomes smaller than the energy bin width ΔE_{bin}.

To investigate when this is, we consider the average energy loss, defined as the following quantity:

$$\begin{aligned} \langle \Delta E_j \rangle &= \frac{\Gamma^{IC}_{loss}(E_j) \cdot E_j}{\Gamma^{IC}(E_j)} \\ &= \frac{\int \mathrm{d}E_i\, \gamma^{IC}_{e\to e}(E_j, E_i)\,(E_j - E_i)}{\int \mathrm{d}E_i\, \gamma^{IC}_{e\to e}(E_j, E_i)} \quad \approx \quad \frac{\sum_i \left(\bar{\gamma}^{IC}_{e\to e}(E_j, E_i)\,(E_j - E_i)\,\Delta E_{i,bin}\right)}{\sum_i \bar{\gamma}^{IC}_{e\to e}(E_j, E_i)\Delta E_{i,bin}}. \end{aligned} \tag{4.27}$$

The first line in the expression above uses the exact calculation of the total rates, whereas the final expression uses the one-bin integrated differential interaction rates. These two versions are found to differ by two energy bins consistently throughout the energy range.

We compare the average energy loss to the energy bin width ΔE_{bin}:

$$E_{crit} \equiv \max\{E_i\} \text{ for which } \frac{\langle \Delta E_i \rangle}{\Delta E_{bin}} < \alpha, \tag{4.28}$$

where α is a value from 0 to 1. We let E_{crit} be defined as the lowest energy that satisfies this requirement. We find that a value for α of 0.4 gives the best results for where the exact and CEL approximation match and a smooth transition can be performed. This fixes the value for the critical energy at:

$$E_{crit} = 1.68 \times 10^7 \text{ MeV}. \tag{4.29}$$

The critical energy is defined for Inverse Compton scattering on the CMB. For the EBL background, the Inverse Compton scattering process was found to be insignificant compared to the contributions from the other two backgrounds, CMB and URB, along the entire energy range, as demonstrated in figure 2.3. For the URB contribution, we only include the contribution from energies above $E \sim 10^{10}$

MeV where it begins to dominate over the CMB contribution. The reason behind this decision is the numerically unstable behaviour of the IC interaction rate on URB as described in section 2.3. We found that only including the high-energy contribution for the IC process on URB did not affect the final results. As a result, we only employ the CEL approximation for Inverse Compton scattering on the CMB.

Interpolation through a smooth transition

Having determined the value at which the transition from the exact calculation to the CEL approximation should occur, we need an interpolation method to get a smooth transition between the two regimes.

To this end we use a transition function $s(i)$ for the energy index i that uses hyperbolic tangent to obtain a smooth transition:[3]

$$s(i) = 0.5 + 0.5 \cdot \tanh\left(\frac{i - i_{cr}}{b}\right). \tag{4.30}$$

The transition function is characterised by the two index parameters i_{cr} and b. The index for the critical energy i_{cr} defines the point where we switch from the CEL approximation to the exact calculation. The parameter b determines the width of the interpolation, i.e. how many energy bins the interpolation should take place over. Setting the value $b = 1$ gives a sharp, step function-like transition, and higher values of b gives a wider, softer transition. We fix b at the value 3 for the calculations in the subsequent chapters.

We apply the transition function $s(i)$ for the energy index i on the transition matrices to interpolate from the exact calculation $\mathcal{T}$ to the CEL approximation $\mathcal{T}_{CEL}$:

$$\mathcal{T}_{int}(E_i, E_j, \Delta t) = s(i) \cdot \mathcal{T}(E_i, E_j, \Delta t) + (1 - s(i)) \cdot \mathcal{T}_{CEL}(E_i, E_j, \Delta t). \tag{4.31}$$

We evaluate our cascade computations by taking advantage of the fact that the processes involved should conserve the energy density $N\,E$, where N refers to the number of particles and E to their energy.

We define the error percentage for our calculations by comparing the initial energy density to the final energy density as:

$$\epsilon = \frac{\left(N_{in}^{e^\mp} E + N_{in}^{\gamma} E\right) - \left(N_{out}^{e^\mp} E + N_{out}^{\gamma} E\right)}{N_{in}^{e^\mp} E + N_{in}^{\gamma} E}\ \%. \tag{4.32}$$

4.2 Inverse Compton Scattering and Breit-Wheeler Pair Production

We apply the matrix doubling method to propagate the EM particles by performing the doubling procedure on each of the total transition matrices $\mathcal{T}_{int}$, $\mathcal{T}_{CEL}$ and $\mathcal{T}_{int}$ independently. We show the outcome from the three different transition matrices in figure 4.1 below, with additional figures (B.4, B.5 and B.6) in Appendix B.3.

For all these figures, we consider the outcome from applying our EM module to an initial spectrum of either photons, electrons or both with an injection spectrum of $\frac{\mathrm{d}N}{\mathrm{d}E} \sim E^{-2}$. When we plot the initial spectra on a y-axis of $E^2 \cdot \frac{\mathrm{d}N}{\mathrm{d}E}$, we then get a flat, constant/horizontal spectrum. We propagate the spectra for a distance of 0.1 Mpc, which corresponds to a number of doublings of $n = 10$ and a stepsize of $\Delta t = 0.0977$ kpc, cf. equation (4.19).

In the four-paneled figure 4.1 we consider the outcome from applying our EM module using Inverse Compton scattering on an initial spectrum of electrons only on CMB photons. We do this in order to assess the interpolation which only applies to Inverse Compton scattering on the CMB.

[3] The webpage www.j-raedler.de/2010/10/smooth-transition-between-functions-with-tanh/ gives an excellent brief review of using tanh to get smooth transitions. Alternative transition functions were tested in this work as well, including transitions that reach 0 truly and not just asymptotically, but these were found to create small features around the critical energy while otherwise giving the same results.

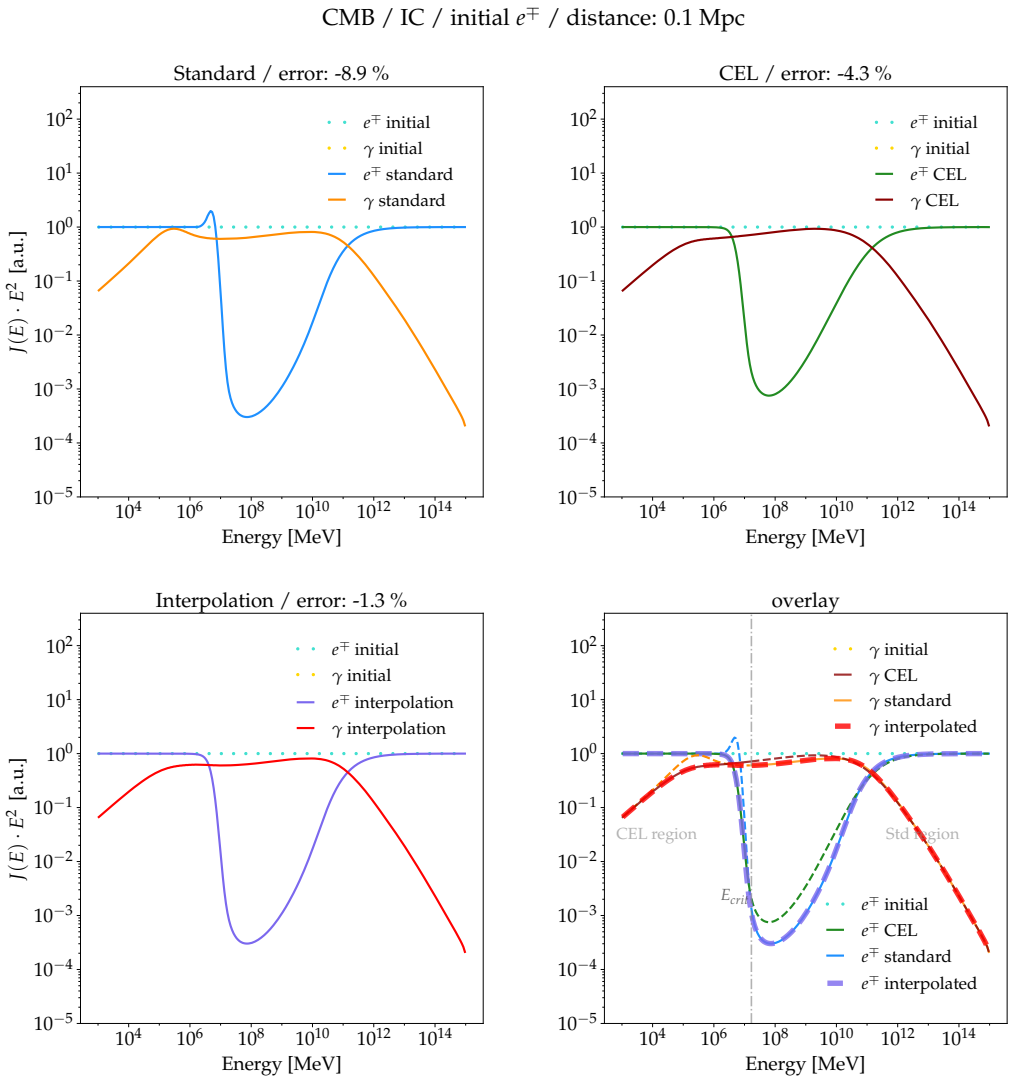

Figure 4.1: IC on CMB: The results from the EM module for an initial spectrum $\frac{\mathrm{d}N}{\mathrm{d}E} \sim E^{-2}$ of electrons/positrons only, propagated for 0.1 Mpc with the Inverse Compton scattering process active on the CMB and other processes (and backgrounds) deactivated.

The Inverse Compton scattering process: $e^- + \gamma_{CMB} \rightarrow e^- + \gamma$ is seen to give the expected conversion of higher-energy electrons to photons, with the dip in the spectrum coinciding with the dip in the energy loss length as shown in figure 2.3.

The figure (4.1) illustrates the effect of the CEL approximation. As indicated on the lower right panel, the CEL region is to the left of the critical energy, while the "standard" region using the exact calculation is to the right. We expect the CEL spectra to describe the physical results well in the CEL region, so the interpolation follows the CEL approximation in this region. At E_{crit}, the interpolation should transition smoothly into the spectra from the exact calculation in the standard region. As indicated by the figure, we conclude that our interpolation has the desired behaviour throughout the entire energy range. For this example, we see that the interpolation leaves out the small artifact just after 10^6 MeV in the electron/positron spectrum, while retaining the deeper dip in the electron/positron spectrum around 10^8 MeV from the exact calculation compared to the CEL approximation. The error-percentage is lowest for the interpolation (compared to CEL only or standard calculation only), indicating that the interpolation does the best job of conserving the

energy density as described in equation (4.32).

The result of the interpolation in the panel to the lower left hence represents our best model for the EM cascade spectra after propagating the initial photons for 0.1 Mpc.

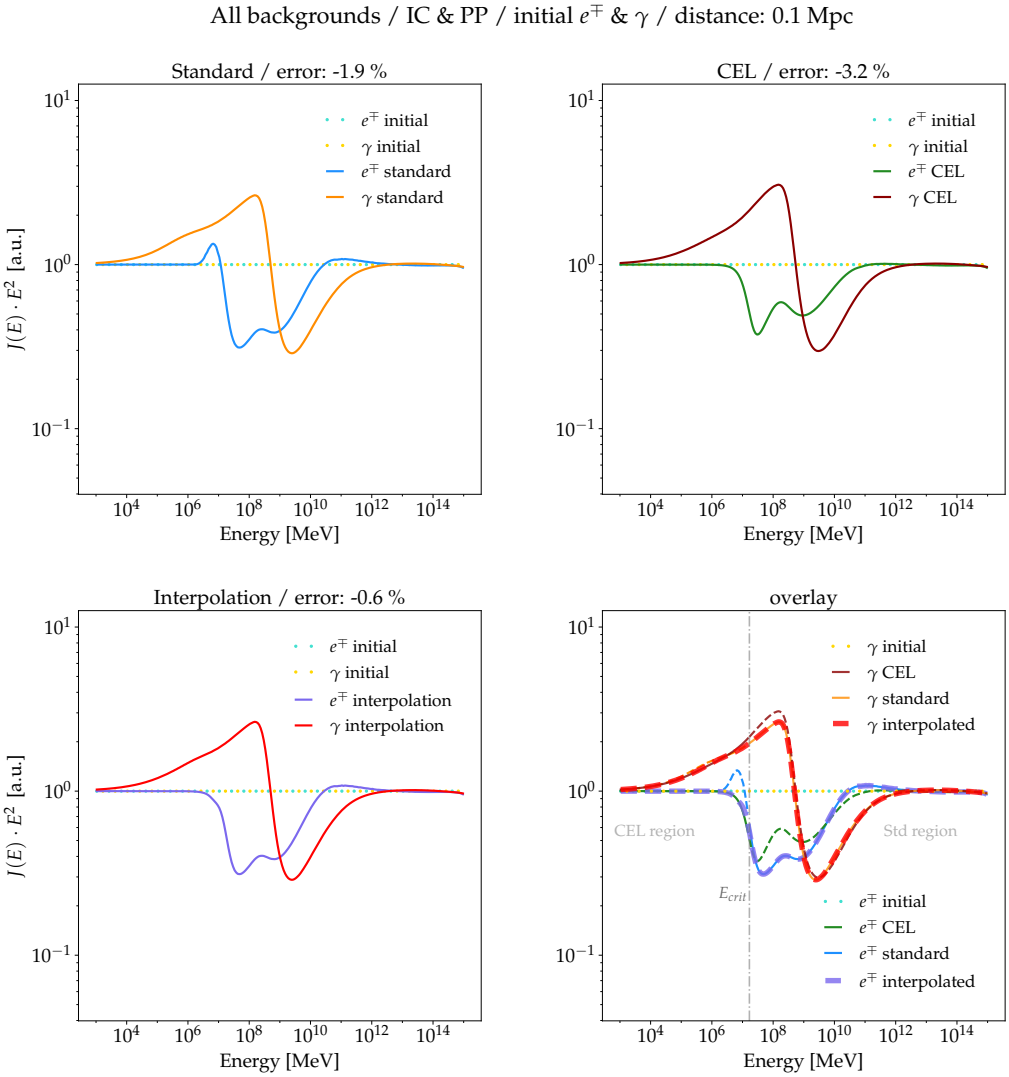

Figure 4.2: All backgrounds: The resulting spectra from the EM module applied to initial spectra of electrons/positrons and photons with $\frac{dN}{dE} \sim E^{-2}$ that have been propagated for 0.1 Mpc. The propagation uses all three backgrounds: CMB, EBL and URB for both processes: Inverse Compton scattering and Pair Production.

In figure 4.2, we consider the outcome from the full calculation, meaning that we include both of the interaction processes: Inverse Compton scattering and Pair Production, as well all three photon backgrounds: CMB, EBL (infrared) and URB (radio), applied to initial spectra of both photons and electrons.

The Appendix chapter B.3 contains additional plots in three categories: 1) Inverse Compton scattering and Pair Production for the CMB only, for further examples of the interpolation in action, 2) further examples using all three photon backgrounds and finally 3) an example using only the Pair Production process.

4.3 Comparisons with simulated data

In order to verify the results from our EM module, we turn to CRPropa to generate a small amount of EM particles and track their propagation and the resulting electromagnetic cascades. We use an initial spectrum of $\frac{\mathrm{d}N}{\mathrm{d}E} \sim E^{-1}$ and reweight it by initial energy to obtain an injection spectrum of $\frac{\mathrm{d}N}{\mathrm{d}E} \sim E^{-2}$. We include Inverse Compton scattering and Pair Production on the CMB in the simulation.

As described in section 4, we are only able to simulate small quantities of EM particles over short distances when we use the CRPropa modules for EM cascade propagation, out of resource considerations. We are thus limited to these small-scale comparisons of the cascade computations. This is the reason behind the low Monte Carlo statistics used for the figures, causing noisy CRPropa spectra.

Inspection of the comparisons in figures 4.3 and 4.4 show that our interpolations (dotted lines) agree well with the results from the CRPropa cascade simulation.

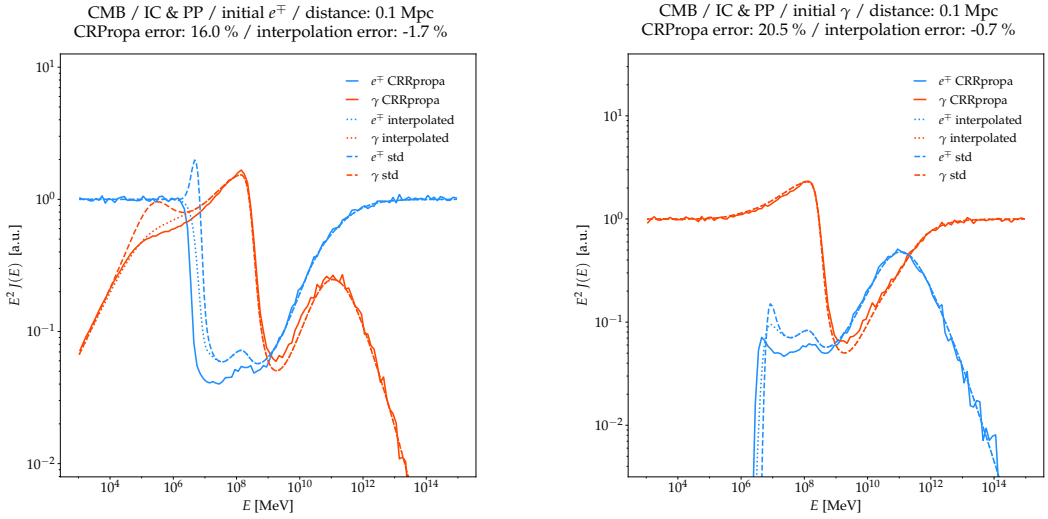

Figure 4.3: Comparison of EM module and CRPropa output for initial electrons: Comparison of resulting spectra from initial particles with injection spectrum $dN/dE \sim E^{-2}$ after propagating a distance of 0.1 Mpc with the EM module and with CRPropa. Inverse Compton scattering and Pair Production on the CMB are considered. Error percentages listed are given by the expression (4.32). *Left:* Results using only initial electrons. *Right:* Results using only initial photons.

4.4 Combination of EM module with CRPropa: Redshift effects

We have now presented the simulation setup for generating UHECRs and propagating them with the Monte Carlo Code CRPropa, as well as our numerical Boltzmann-solver EM module for propagating the EM cascades. This section will briefly lay out the combination of these two techniques with redshift effects — the implementation of which is still a work in progress.

So far we have focused on the treatment of cascade evolution using photon backgrounds and interaction rates at $z = 0$. A full treatment of EM cascades would include redshifts of the photon backgrounds and of the interaction rates for Inverse Compton scattering and Pair Production.

The photon backgrounds depend on redshift in different ways. For the CMB, the photon field has a simple scaling with redshift, so that knowing the photon density at $z = 0$ immediately gives the redshift evolution of it as well [45]:

$$n_\gamma(z, \varepsilon) = (1+z)^2 \, n_\gamma(0, \, \varepsilon/(1+z)\,). \tag{4.33}$$

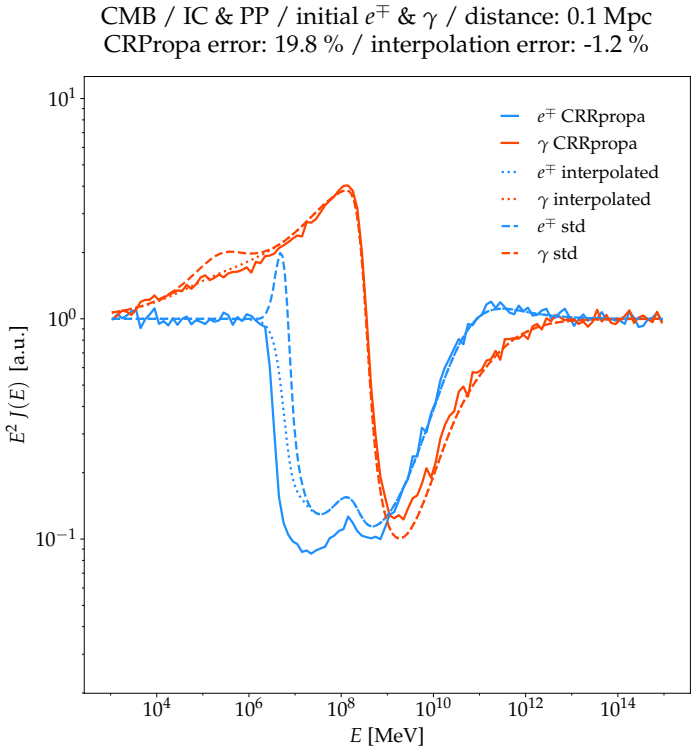

Figure 4.4: Comparison of EM module and CRPropa output for simultaneous input of electrons and photons: As in figure 4.3, but here showing the results for a simultaneous injection of initial photons of electrons.

This will scale the total and differential interaction rates in the following way:

$$\Gamma_i(z, E_i) = (1+z)^3\, \Gamma_i(0,\, (1+z)E_i), \tag{4.34}$$

$$\gamma_{ij}(z, E_i, E_j) = (1+z)^4\, \gamma_{ij}(0,\, (1+z)E_i,\, (1+z)E_j). \tag{4.35}$$

For the EBL and URB backgrounds however, the redshift scaling does not have this simple form. Usually the photon densities are given as tabulated data for different redshift steps. As an approximation, a redshift scaling can be used for the EBL as was done in [45].

In order to implement redshift effects in our EM module, we need to account for both the redshift evolution of the photon backgrounds and the interaction rates in the Boltzmann equations (4.2) and (4.3). The first step in this implementation is to place the spectra of photons, electrons and positrons obtained from the Monte Carlo simulation in redshift bins. Each redshift bin thus represents a redshift "slice" of the particles. The idea is then to take the output of EM particle fluxes from one redshift step and make a prediction using the Boltzmann cascade equations for what the flux would be at redshift $z - \Delta z$. Then we use this result as the input for the next redshift step, and so forth all the way to redshift $z = 0$ to get the final cascade spectrum.

The next step is to include the redshift effects in the Boltzmann equations that govern the evolution of the cascades in the EM module.

We will here briefly outline how to derive a solution for a given redshift slice by starting from the Boltzmann equations and accounting for redshift evolution, following ref. [45]. We replace the comoving densities $Y = n\,\frac{a^3}{a_0^3}$ in the Boltzmann equations (1.7) by their redshift-dependent counterparts Z:

$$Z(z, E) \equiv (1+z)Y((1+z)E). \tag{4.36}$$

From the evolution of Z, we obtain the expression:

$$\dot{Z} = (1+z)\left[\partial_t Y(t,\mathcal{E}) - \partial_{\mathcal{E}}(H\,\mathcal{E}\,Y(t,\mathcal{E}))\right], \tag{4.37}$$

where $\mathcal{E}$ is the energy that a particle had at redshift z, if we today observe it with the energy E, defined as $\mathcal{E} = (1+z)E$, and H is the Hubble parameter [45]. Next, we can express the Boltzmann equations as:

$$\dot{Z} = -\Gamma_i(z,(1+z)E_i)Z(z,E_i) + \int \mathrm{d}E_j\left[(1+z)\gamma(z,(1+z)E_j,(1+z)E_i)\right]Z(z,E_j) \\ +(1+z)\mathcal{L}_i(z,(1+z)E_i). \tag{4.38}$$

Here $\mathcal{L}_i$ is the source term emitting CRs of type i. From the last term we identify:

$$(1+z)\mathcal{L}_i(z,(1+z)E_i) = \frac{(1+z)H(z)}{\Delta z}\,n_\gamma(E), \tag{4.39}$$

where n_γ is the photon density from the Boltzmann equations in (4.2).

As a final step, we consider the evolution of $Z(z,E)$ with redshift: $\frac{\mathrm{d}Z}{\mathrm{d}z} = \frac{\mathrm{d}t}{\mathrm{d}z}\frac{\mathrm{d}Z}{\mathrm{d}t} = -\frac{1}{H}\,\mathcal{L}(z,(1+z)E)$. Integrating this quantity over all redshift allows us to identify, for sufficiently small Δz:

$$n_\gamma(E) = Z(0,E) = \frac{\Delta z}{H(z)}\mathcal{L}(z,(1+z)E). \tag{4.40}$$

Rearranging this gives us the final expression:

$$(1+z)\mathcal{L}_i(z,(1+z)E) = \frac{(1+z)H(z)}{\Delta z}\,n_\gamma(E), \tag{4.41}$$

where the source term $\mathcal{L}_i(z,(1+z)E)$ is given by the EM output from CRPropa per redshift slice. In this way we get the $n_\gamma(E)$ that we can propagate with the EM module using the equation (4.18). The aim is then to calculate the transition matrices in equation (4.17) once at $z = 0$ and then rescale them by redshift instead of having to recalculate them at each redshift step.

4.5 Results for electromagnetic cascades

Equipped with our EM module, we can now combine the results from chapter 3 with the implementation of the cascade emission. By taking the spectra of photons, electrons and positrons we generated with the Monte Carlo-based simulation of UHECR propagation and using that as the input in our EM module, we can compute the electromagnetic cascades for cosmogenic γ-rays and electrons/positrons.

This allows us to combine the different elements we have studied in this thesis and highlight the multimessenger relations between UHECRs and cosmogenic fluxes. We show these final results in the section below.

4.5.1 EM cascades from proton dominated spectra

To investigate the EM cascade emission from different types of initial spectra, we compare the results from the EM module for particles obtained with a simulation to particles obtained from generic injection spectra.

Figure 4.5 shows the results for the two types of initial spectra, each for two different simulation setups: The first setup (left panels) propagates the initial EM spectra over a distance of 100 Mpc with both interactions, Inverse Compton scattering and Pair Production, on all three photon backgrounds CMB, EBL and URB. The second setup (right panels) uses a propagation distance of 1 Gpc and otherwise has the same parameter settings as setup 1.

The first row in the figure 4.5 shows the electromagnetic cascades resulting from propagating initial injections of first-generation cosmogenic photons and electrons (dotted lines) from a proton-dominated UHECR spectrum with no source redshift evolution, the "no evolution" case in figure 3.2. The injection settings described in 3.2.1 were used.

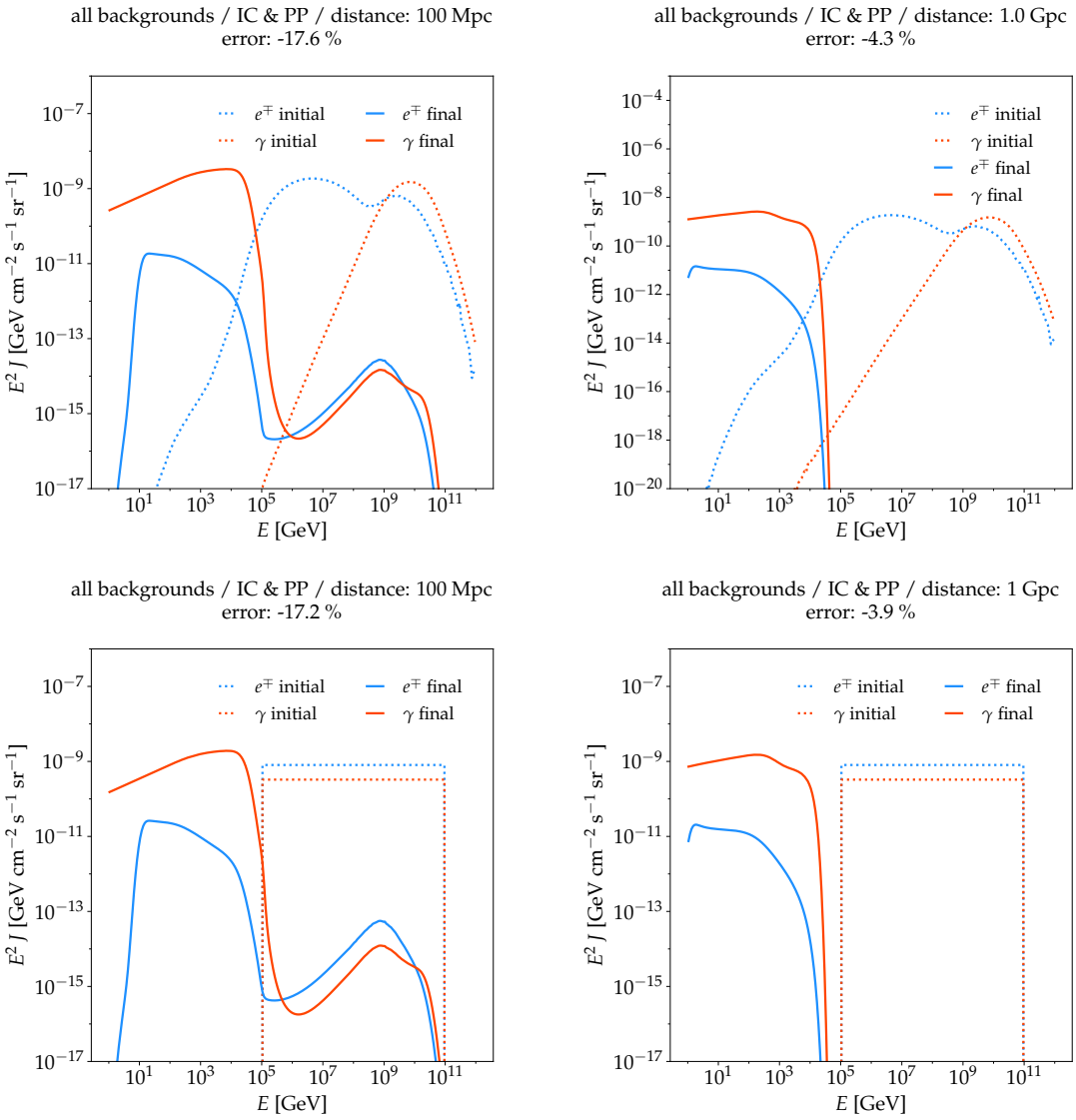

Figure 4.5: Electromagnetic cascades. *The first row* of plots show the results of propagating the first generation of γ-rays and electrons produced by protons from the no-evolution case in figure 3.2 with the EM module for two different distances. *The second row* of plots show the corresponding results when propagating photons and electrons with simple $\frac{\mathrm{d}N}{\mathrm{d}E} \propto E^{-2}$ injection spectrum for the same set of distances. The error percentage for the energy density conservation is calculated with the expression in (4.32).

In the second row of the figure, we show the results from the same two propagation setups for initial generic spectra of photons and electrons (dotted lines) with $\frac{\mathrm{d}N}{\mathrm{d}E} \propto E^{-2}$ for energies from $0.1\,\mathrm{PeV} = 10^5\,\mathrm{GeV}$ to $100\,\mathrm{EeV} = 10^{11}\,\mathrm{GeV}$.

Comparing the top row to the bottom row, we see a clear universality of the cascades (solid lines) independent of the details or form of the injection spectrum; the initial spectrum gets washed out at larger distances with a resulting pile-up of photons and electrons in the GeV-TeV range. This is expected due to the short interaction lengths of Inverse Compton scattering and Pair Production compared to the large propagation distance scales. The cascades evolve so rapidly over cosmological distances that in effect, what happens after around 1 kpc – the peak of the interaction length (figures 2.3 and 2.2) – will have very limited consequences.

Since we see qualitatively the same spectra from different initial injections, we can conclude that

including more details about the source injection would not impact the resulting cascade spectra to a high degree.

4.5.2 Multimessenger relations

We present a summary plot in figure 4.6 that combines the different elements in our analysis to highlight their mutual relations and comparisons to the relevant data.

Our fit to UHECR data dominated by protons (in black) is shown together with the data from ref. [15] (in green) and our predictions for the corresponding cosmogenic neutrino flux (in red). The prospective sensitivity limit from the future detector IceCube-Gen2 Radio [33] is included to demonstrate our predictions for the possibility of observing the cosmogenic neutrino flux. For a UHECR source population without source evolution with redshift, we would need a proton contribution to the UHECR flux above 50 EeV of around 10 % in order for the cosmogenic neutrino fluxes to be observable by IceCube-Gen2 Radio, as we saw in figure 3.3.

For the electromagnetic particles we show the cascade emission, obtained with our EM module and plotted as the orange line for cascade γ-rays and blue line for cascade electrons/positrons, as well as the high-energy γ-ray component (in dark blue) accounting for CMB attenuation. The two photon components – the HE photons together with the cascade photon flux – are an approximation for the full cosmogenic γ-ray flux. We include the isotropic γ-ray background data from the Fermi-LAT satellite [34] (blue arrows) for comparison with our prediction for the cascade γ-rays, as well as the upper limits for the diffuse flux of UHE photons from Pierre Auger [61] (cyan arrows) for comparison of our HE cosmogenic γ-ray prediction.

For the high-energy part of the spectrum, above $E \sim 10^7$ GeV, the cosmogenic γ-rays will be dominated by the first generation of γ-rays attenuated by the cosmic photon backgrounds. In our calculations for this first γ-ray generation, we include a redshift dependence in the attenuation by Pair Production on the CMB, but mostly omit secondary production via the Inverse Compton scattering process that would generate the EM cascades. We are currently investigating the effect from implementing attenuation on the URB as well. As figure 4.6 shows, our results provide a low contribution to the HE γ-ray flux, and we conclude that our prediction is consistent with the upper limits on the diffuse flux of UHE photons given by ref. [61] from Pierre Auger Observatory data. Since photons create showers with a different $X_{\max}$ than CRs, they can be distinguished by the Pierre Auger Observatory observations.

The EM cascade emission gives the contribution of cosmogenic electrons/positrons and γ-rays to the isotropic γ-ray background (IGRB). For figure 4.6 we have simulated the EM cascades for the first generation of EM particles from a CRPropa simulation of the proton spectrum for the "no evolution" case over a distance of 1 Gpc. Based on the results above, the EM cascade spectrum shows universality over long distances – even though the UHECRs that reach us can only come from within $\sim$ 100 Mpc due to their deflections by galactic and extragalactic magnetic fields, the cosmogenic neutrinos and γ-rays can travel much longer distances before arriving at Earth.[4] Our simulations with the EM module produce a broad γ-ray spectrum that peaks in the GeV-TeV range. We see from the figure that the predicted cascade γ-ray flux stays below the Fermi-LAT IGRB data. The IGRB has contributions not only from cosmogenic photons but from many different sources such as blazars. In relation to UHECR models it thus constitutes an upper limit to the corresponding cosmogenic γ-ray flux. Including more protons in the UHECR flux, for example, will increase the cascade γ-ray emission, so in order for predictions to be consistent with the Fermi-LAT data, an upper limit on the proton content can be determined. In this way our minimal model for cosmogenic γ-ray flux is consistent with the data but does not provide a strong constraint.

We use the approximation with two cosmogenic photon components (cascades and HE γ-rays) in order to emulate the total, continuous EM production over the full redshift range. The implementation of the redshift effects in our EM module was beyond the timeframe of this thesis, but would otherwise be able to provide the full cosmogenic EM emission in terms of both cascades and UHE γ-rays. It is expected that a full calculation of the EM emission that also includes redshift effects would

[4] The UHE electrons would emit synchrotron radiation when deflected by magnetic fields, but this process has not been implemented in the EM module as we have considered 1D simulations only [19, 29].

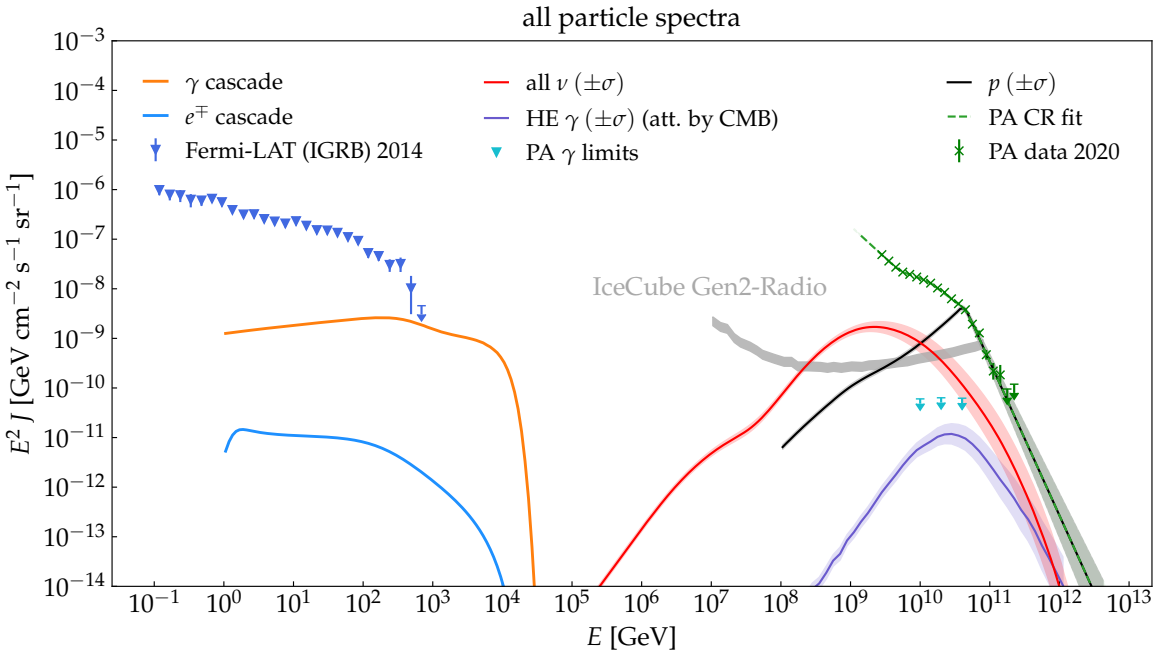

Figure 4.6: Multimessenger plot: Comparison of the flux of cosmogenic neutrinos, UHECRs, cosmogenic γ-rays and cascade photons and electrons with all-particle UHECR data and fit [1] as well as upper limits for UHE diffuse photon flux [61] from the Pierre Auger Observatory, isotropic γ-ray background data from Fermi-LAT [34] and the sensitivity of the IceCube-Gen2 Radio [33]. The "no evolution" case for the UHECR protons was used. The cascade photons and electrons are the result of propagating the first generation of γ-rays and electrons with the EM module for a distance of 1 Gpc. The cosmogenic high-energy γ-rays are attenuated by pair-production on the CMB.

introduce some features in the spectrum that are not seen in the results here, but since the emission is calorimetric and thus conserves the total energy, the overall intensity of the emission would not change.

Chapter 5

Conclusion and outlook

Multimessenger studies are becoming more central in the field of UHECR physics as we increase our possibilities for observing UHE messengers. Taking advantage of their mutual relations provides us with stronger constraints on UHECR source models and propagation effects. Combined analyses of multiple messengers can help deepen our understanding of some of the most powerful processes and objects in the universe.

In this thesis we have investigated cosmogenic fluxes from UHECRs and their dependencies on different source model uncertainties.

We have presented a combined framework of Monte Carlo methods and a numerical Boltzmann-solver. By using the Monte Carlo code CRPropa to propagate the primary UHECRs and combining it with a numerical EM Boltzmann-solver module, we are able to perform faster and less resource-heavy computation of the propagation of EM particles, while at the same time allowing for a fast and easy upgrade of the applied photon backgrounds. Since the generation of secondary particles by UHECRs depends strongly on the interactions with photon background fields, it is an advantage to have a flexible way of exchanging these to updated models.

The first part of our results considered UHECRs with energies above 50 EeV. For these energies we could estimate the UHECR nucleon spectrum directly from the observed mass composition at Earth and obtain the corresponding cosmogenic fluxes. We found that the source evolution of the UHECR sources affects the predicted cosmogenic fluxes by a factor 5 when comparing sources without evolution to the case of Star Formation Rate evolution.

When it comes to the prospects for observing cosmogenic neutrino fluxes, we found that next-generation neutrino observatories will be capable of observing cosmogenic neutrinos if the observed proton contribution is 2% (for sources with an SFR source evolution) or 10% (for sources without source evolution). Our result shows that while the minimal cosmogenic neutrino flux from a mixed-composition UHECR scenario is not guaranteed to be detectable, the prospects would improve if source evolution with redshift is allowed.

Using the model for a combined fit of recent UHECR spectrum and composition data, we found an average observed mass number of $A_{\rm obs} = 21.3$ at the energy 50 EeV. Rescaling the minimal cosmogenic neutrino flux by the observed mass number gave us a very conservative lower limit for the predicted neutrino flux from the mixed-composition model.

In the second part of our results, we turned our attention to the cosmogenic γ-rays. We implemented a module for propagating EM particles from UHECRs. The module includes the processes Breit-Wheeler Pair Production and Inverse Compton scattering on three different photon backgrounds (CMB, EBL and URB) designed as functions that are easily exchanged for later, upgraded measurements.

With results from our EM module, we found a universality of the cascade spectra of γ-rays and electrons/positrons across different initial injections propagated over large distances. The minimal cosmogenic γ-ray flux was found to be consistent with isotropic γ-ray data. The high-energy γ-ray

emission component was likewise found to be consistent with the upper limits on the HE photon flux from CR observatories.

In conclusion, our minimal models for cosmogenic fluxes of neutrinos and γ-rays constrain the models of UHECRs. While the constraints we obtained are not strong, they provide a framework for testing multiple contributions to the observed data simultaneously. This can be used to estimate the required sensitivity of future neutrino and CR observatories necessary for their detection.

A full treatment of the electromagnetic cascades would include redshift effects as a direct continuation of the work presented within this thesis on the Electromagnetic Cascades Module. This would improve the predictions for the γ-ray flux from UHECR sources, but since the EM emission is calorimetric, it would not change the overall intensity.

An outlook for the use of the EM module in its current version is to study local sources, where the effects from redshift scaling will be of less importance. As an example of this, we propagate the photon emission from the blazar 1ES 0229+200 as shown in figure 5.1. This blazar has a redshift of $z = 0.14$ and has been studied by ref. [62] (and subsequently others) to give lower bounds on the strength of the intergalactic magnetic field.

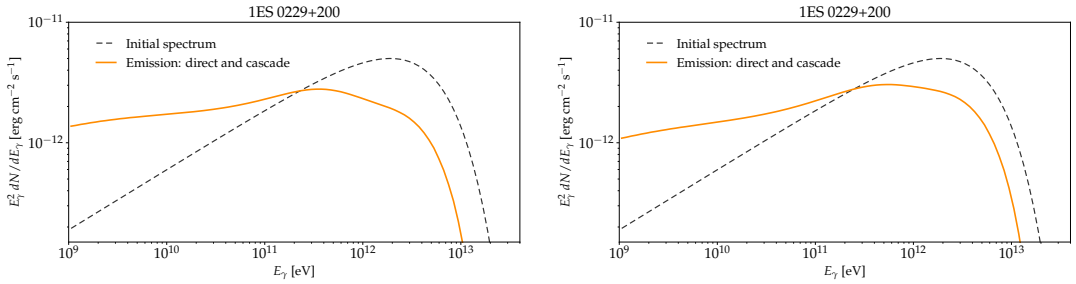

Figure 5.1: Blazar 1ES 0229+200. The emission from the blazar 1ES 0229+200 modeled by the initial γ-ray spectrum from [62]: $\frac{dN_\gamma}{dE} \sim E^{-\Gamma} \exp(-E/E_{cut})$, with $\Gamma = 1.5$ and $E_{cut} = 3.8$ TeV. The initial spectrum is propagated with the EM module taking into account Inverse Compton scattering and Breit-Wheeler Pair Production on different photon backgrounds. *Left:* Only the photon backgrounds EBL and CMB are included in the interactions in order to compare to the results from [62] fig. 1. *Right:* Interactions take place on all three photon backgrounds EBL, CMB and URB.

Modeling processes taking place over vast distances in universe is of course no simple undertaking, and there are several ways to extend our analysis to include more aspects of the physics of UHECR sources and UHECR propagation. Two important extensions are currently works-in-progress for the EM module: incorporating redshift effects, as described in the previous sections, and including additional higher-order interaction processes.

The planned implementation of the redshift effects was described in section 4.4. For the second extension, we would like to include the higher-order processes Double Pair Production (DPP; $\gamma + \gamma_{bg} \rightarrow e^- + e^+ + e^- + e^+$) and Triple Pair Production (TPP; $e^\mp + \gamma_{bg} \rightarrow e^\mp + e^- + e^+$) as well [44]. While we do not expect major changes from including DPP, since it has a longer interaction length across the energy scale than the competing Pair Production interaction that dominates, we would expect TPP to influence UHE electron spectra at energies above $E \sim 10^{18}$ eV, as seen in [29].

Further potential extensions include modeling the source environments of UHECRs themselves and taking into account the extragalactic and galactic magnetic fields and the synchrotron energy losses they would cause for charged particles.

The aim of extending the EM module and its combination with UHECR propagation simulations is to take advantage of the correlations and dependencies between the three messengers – UHECRs, cosmogenic neutrinos and cosmogenic γ-rays – to learn more about their potential sources in the universe – and what we must prepare for here at Earth if we wish to detect their signals.

Appendix A

Interaction rates

The following sections give detailed derivations of the calculations found in chapter 2, as well as some technical derivations implemented for increased numerical stability. Note that the CMB background is used as an example in many of the calculations.

A.1 Pair production: Interaction rate integration strategy

Figure B.3 in the next Appendix chapter shows the interaction rates for Breit-Wheeler pair production (PP) on the CMB, EBL and URB.

Below, we go into details on the derivations of the interactions rates that were implemented in the EM module.

A.1.1 Total interaction rate Γ_{PP}

Step 1: Changing integration variable from $\cos\theta \to s_{GS}$*:*

We follow Gould & Schréder (1967) [42] and change integration variable from $\cos\theta$ to the quantity $s_{\rm GS} = \frac{s}{4m_e^2}$, a dimensionless version of the invariant squared centre of momentum frame energy $s = (p_i^\mu + p_j^\mu)(p_\mu^i + p_\mu^j) = (p_i + p_j)^2 = 2\varepsilon E_\gamma(1-\cos\theta)$:[1]

$$s_{\rm GS} \equiv \frac{\varepsilon E_\gamma(1-\cos\theta)}{2m_e^2} \;\Leftrightarrow\; \frac{1-\cos\theta}{2} = s_{\rm GS}\frac{m_e^2}{E_\gamma\varepsilon} \quad \Rightarrow \tag{A.1}$$

$$\frac{\mathrm{d}s_{\rm GS}}{\mathrm{d}\cos\theta} = \frac{\mathrm{d}}{\mathrm{d}\cos\theta}\frac{\varepsilon E_\gamma(1-\cos\theta)}{2m_e^2} = -\frac{\varepsilon E_\gamma}{2m_e^2} \;\Leftrightarrow\; \mathrm{d}\cos\theta = -\left(\frac{2m_e^2}{E_\gamma\varepsilon}\right)\mathrm{d}s_{\rm GS} \tag{A.2}$$

Substituting both of these equations into the integral in $\Gamma(E)$ (equation (1.12)), we get:

$$\begin{aligned}
\Gamma_{PP}(E_\gamma) = \lambda_{PP}^{-1}(E_\gamma) &= \frac{1}{2}\int_{\varepsilon_{th}}^{\infty}\int_{-1}^{1}(1-\cos\theta)\,n_\gamma(\varepsilon)\,\sigma_{PP}\,\mathrm{d}\cos\theta\,\mathrm{d}\varepsilon \\
&= \int_{\varepsilon_{th}}^{\infty}\int_{s_{\rm min}}^{s_{\rm max}} s_{\rm GS}\,\frac{m_e^2}{E_\gamma\varepsilon}\,n_\gamma(\varepsilon)\,\sigma_{PP}(s_{\rm GS})\left(\frac{2m_e^2}{E_\gamma\varepsilon}\right)\mathrm{d}s_{\rm GS}\,\mathrm{d}\varepsilon \\
&= 2\left(\frac{m_e^2}{E_\gamma}\right)^2\int_{\varepsilon_{th}}^{\infty}\frac{n_\gamma(\varepsilon)}{\varepsilon^2}\int_{s_{\rm min}}^{s_{\rm max}} s_{\rm GS}\,\sigma_{PP}(s_{\rm GS})\,\mathrm{d}s_{\rm GS}\,\mathrm{d}\varepsilon.
\end{aligned}$$

Here $s_{\rm min}$ is the minimum value for the dimensionless version of the centre of momentum energy, and the corresponding maximum, e.g. for a head-on collision, is given by $s_{\rm max}$. The minus sign from (A.2) flips the limits of integration over cosine in the second line above[2], so we go from $-(-1,1) \to (1,-1) \to (s_{\rm min}, s_{\rm max})$.

[1] We use the convention for four-vector notation from [63].

[2] Since $\cos\theta$ is an even function, it holds that: $\int_{-1}^{1} -\cos(x)\,f(y)\,\mathrm{d}x = \int_{1}^{-1}\cos(x)\,f(y)\,\mathrm{d}x$.

For the integration limits, we change from $\cos\theta$ to $s_{\rm GS}$ in the following way:

- The lower integration limit becomes: $\theta_{\rm min} = 0 \;\; (\cos\theta = 1) \;\rightarrow\; s_{\rm min} = 1$,

  since if $s_{\rm GS} < 1$ and with $\frac{1-\cos\theta}{2} \in [0,1]$, we get from the definition of $s_{\rm GS}$:

$$s_{\rm GS} \equiv \frac{\varepsilon E_\gamma (1-\cos\theta)}{2m_e^2} < 1 \;\Leftrightarrow\; \frac{\varepsilon E_\gamma}{m_e^2} < 1 \;\Leftrightarrow\; \varepsilon E_\gamma < m_e^2,$$

  and hence the production of the e^+e^--pair cannot take place.

- Following from this, the threshold condition (for head-on photon collision) is thus: $\varepsilon_{th}\, E_\gamma = m_e^2 \;\Rightarrow\; \varepsilon_{th} = \frac{m_e^2}{E_\gamma}$. Switching to $s_{\rm GS}$, the threshold condition in the center-of-mass frame comes from the requirement that enough energy is needed to create the pair of electrons: $\sqrt{2\varepsilon E_\gamma(1-\cos\theta)} \geq 2m_e c^2 \Rightarrow \varepsilon_{th} = \frac{2m_e^2c^4}{E_\gamma(1-\cos\theta)} \Rightarrow s_{th} = 1$

- We find the upper integration limit when the angle is maximal: $\theta_{\rm max} = \pi \;\; (\cos\theta = -1) \;\rightarrow\; s_{GS,\rm max} = \frac{\varepsilon E_\gamma (1-\cos\theta_{\rm max})}{2m_e^2} = \frac{\varepsilon E_\gamma 2}{2m_e^2} = \frac{\varepsilon E_\gamma}{m_e^2}$.

The interaction rate is then:

$$\Gamma_{PP}(E_\gamma) = \lambda_{PP}^{-1}(E_\gamma) = 2\left(\frac{m_e^2}{E_\gamma}\right)^2 \int_{\frac{m_e^2}{E_\gamma}}^{\infty} \frac{n_\gamma(\varepsilon)}{\varepsilon^2} \int_1^{\frac{\varepsilon E_\gamma}{m_e^2}} s_{\rm GS}\, \sigma_{PP}(s_{\rm GS})\; {\rm d}s_{\rm GS}\, {\rm d}\varepsilon. \tag{A.3}$$

Step 2: Changing integration variable from $\varepsilon \rightarrow \varepsilon_0 = \frac{\varepsilon}{k_B T}$*:*

We introduce a parameter to perform the integration over the background photon energy over a dimensionless variable:

$$\varepsilon \;\rightarrow\; \varepsilon_0 = \frac{\varepsilon}{k_B T} \;\Rightarrow\; \frac{{\rm d}\varepsilon_0}{{\rm d}\varepsilon} = \frac{1}{k_B T} \;\Leftrightarrow\; {\rm d}\varepsilon = k_B T\, {\rm d}\varepsilon_0.$$

With this substitution the integral in $\Gamma(E)$ over the background photon energy for CMB from (1.13) becomes:

$$\int \frac{n(\varepsilon)}{\varepsilon^2}\, {\rm d}\varepsilon = \int \frac{1}{\varepsilon^2}\frac{\varepsilon^2}{\pi^2}\left(e^{\varepsilon/k_BT} - 1\right)^{-1} {\rm d}\varepsilon = \frac{k_B T}{\pi^2}\int (e^{\varepsilon_0} - 1)^{-1}\; {\rm d}\varepsilon_0. \tag{A.4}$$

We now return to the interaction length $\Gamma_{PP}(E_\gamma)$. The integral over $s_{\rm GS}$ does not depend on ε except for the upper limit $s_{\rm max} = \frac{\varepsilon E_\gamma}{m_e^2}$. To make the substitution $\varepsilon \rightarrow \varepsilon_0 = \frac{\varepsilon}{k_B T}$, we need to express $s_{\rm max}$ and ε_{th} in terms of ε_0. To this end we introduce a new variable, $x(E_i) \equiv \frac{m_e^2}{E_i k_B T}$:

$$s_{\rm max} = \frac{\varepsilon E_\gamma}{m_e^2} = \frac{\varepsilon_0\, k_B T\, E_\gamma}{m_e^2} \;=\; \frac{\varepsilon_0}{x(E_\gamma)} \tag{A.5}$$

$$\varepsilon_{th} = \frac{m_e^2}{E_\gamma} \;\Rightarrow\; \varepsilon_{0,th} = \frac{\varepsilon_{th}}{k_B T} = \frac{m_e^2}{E_\gamma k_B T} \;\equiv\; x(E_\gamma). \tag{A.6}$$

Finally, we substitute the expressions (A.4), (A.5) and (A.6) into the interaction rate $\Gamma_{PP}(E_\gamma)$ in equation (A.3) and arrive at the interim expression:

$$\begin{aligned}\Gamma_{PP}(E_\gamma) = \lambda_{PP}^{-1}(E_\gamma) &= 2\left(\frac{m_e^2}{E_\gamma}\right)^2 \int_{\frac{m_e^2}{E_\gamma}}^{\infty} \frac{n_\gamma(\varepsilon)}{\varepsilon^2} \int_1^{\frac{\varepsilon E_\gamma}{m_e^2}} s_{\rm GS}\, \sigma_{PP}(s_{\rm GS})\; {\rm d}s_{\rm GS}\, {\rm d}\varepsilon \\ &= 2\,\frac{k_B T}{\pi^2}\left(\frac{m_e^2}{E_\gamma}\right)^2 \int_x^{\infty} (e^{\varepsilon_0} - 1)^{-1} \int_1^{\varepsilon_0/x} s_{\rm GS}\, \sigma_{PP}(s_{\rm GS})\; {\rm d}s_{\rm GS}\, {\rm d}\varepsilon_0. \end{aligned} \tag{A.7}$$

Cross section σ_{PP}

The total cross section for pair production from S.Lee (1998) is given by: [44]

$$\sigma_{PP} = \sigma_T \cdot \frac{3}{16}(1-\beta^2)\left[(3-\beta^4)\ln\frac{1+\beta}{1-\beta} - 2\beta(2-\beta^2)\right], \quad \text{where} \tag{A.8}$$

$$\beta \equiv \left(1 - \frac{4m_e^2}{s}\right)^{1/2} = \left(1 - \frac{1}{s_{\mathrm{GS}}}\right)^{1/2}, \tag{A.9}$$

and where σ_T is the Thompson cross section. We pull out the prefactor and define, analogously to Gould & Schréder (1967), the reduced cross section as the dimensionless $\bar{\sigma}_{PP}$:

$$\bar{\sigma}_{PP}(s_{\mathrm{GS}}) \equiv \frac{1}{\sigma_T}\frac{16}{3}\,\sigma_{PP} = \frac{2}{\pi r_c^2}\,\sigma_{PP},$$

where r_c is the classical electron radius.

Pair Production total interaction rate and interaction length

Using the reduced cross section, we can write equation (A.7) as integrations over only dimensionless quantities times a prefactor:

$$\begin{aligned}\Gamma_{PP}(E_\gamma) = \lambda_{PP}^{-1}(E_\gamma) &= 2\left(\frac{\pi r_c^2}{2}\right)\frac{k_B T}{\pi^2}\left(\frac{m_e^2}{E_\gamma}\right)^2 \int_x^\infty (e^{\varepsilon_0}-1)^{-1}\int_1^{\varepsilon_0/x} s_{\mathrm{GS}}\,\bar{\sigma}_{PP}(s_{\mathrm{GS}})\;\mathrm{d}s_{\mathrm{GS}}\,\mathrm{d}\varepsilon_0 \\ &= \frac{k_B T}{\pi}\left(\frac{m_e^2\, r_c}{E_\gamma}\right)^2 \int_x^\infty (e^{\varepsilon_0}-1)^{-1}\int_1^{\varepsilon_0/x} s_{\mathrm{GS}}\,\bar{\sigma}_{PP}(s_{\mathrm{GS}})\;\mathrm{d}s_{\mathrm{GS}}\,\mathrm{d}\varepsilon_0. \end{aligned} \tag{A.10}$$

This is our final expression for the interaction rate. In natural units, Γ is given in units of eV, and we convert the interaction length $\Gamma^{-1}(E_\gamma) = \lambda(E_\gamma)$ to units of megaparsec by multiplying with $\hbar c$:

$$\lambda_{PP}(E_\gamma)\,[\mathrm{eV}^{-1}] = (\Gamma_{PP}(E_\gamma)\,[\mathrm{eV}])^{-1} \;\rightarrow\; \hbar c\,\Gamma_{PP}^{-1}(E_\gamma)\;[\mathrm{Mpc}]. \tag{A.11}$$

Changing to logarithmic integration variable

To improve the numerical integration, we change to a logarithmic formulation of the integrals. We first transform from ε to a logarithmic quantity, and subsequently transform s' to a logarithmic expression as well.

Setting:

$\varepsilon \rightarrow \log(\varepsilon) = x \quad \Rightarrow \quad \varepsilon = \exp(x)$,

$\mathrm{d}\log\varepsilon = \frac{1}{\varepsilon}\,\mathrm{d}\varepsilon \quad \Rightarrow \quad \mathrm{d}\varepsilon = \varepsilon\,\mathrm{d}\log\varepsilon$, we can transform the total interaction rate as:

$$\Gamma_{PP}(E_\gamma) = 2\left(\frac{m_e^2}{E_\gamma}\right)^2 \int_{\frac{m_e^2}{E_\gamma}}^\infty \frac{n_\gamma(\varepsilon)}{\varepsilon^2}\int_1^{\frac{\varepsilon E_\gamma}{m_e^2}} s_{\mathrm{GS}}\,\sigma_{PP}(s_{\mathrm{GS}})\;\mathrm{d}s_{\mathrm{GS}}\,\mathrm{d}\varepsilon \tag{A.12}$$

$$= 2\left(\frac{m_e^2}{E_\gamma}\right)^2 \int_{\log\left(\frac{m_e^2}{E_\gamma}\right)}^\infty \frac{n_\gamma(\exp(x))}{\exp(x)}\int_1^{\frac{\exp(x)E_\gamma}{m_e^2}} s_{\mathrm{GS}}\,\sigma_{PP}(s_{\mathrm{GS}})\;\mathrm{d}s_{\mathrm{GS}}\,\mathrm{d}x \tag{A.13}$$

$$= \frac{2}{k_B T}\left(\frac{m_e^2}{E_\gamma}\right)^2 \int_{\log\left(\frac{m_e^2}{E_\gamma k_B T}\right)}^\infty \frac{n_\gamma(k_B T\,\exp(x))}{\exp(x)}\int_1^{\frac{\exp(x)\,k_B T\,E_\gamma}{m_e^2}} s_{\mathrm{GS}}\,\sigma_{PP}(s_{\mathrm{GS}})\;\mathrm{d}s_{\mathrm{GS}}\,\mathrm{d}x \tag{A.14}$$

$$= \frac{2}{k_B T}\left(\frac{m_e^2}{E_\gamma}\right)^2 \int_{\log\left(\max\left[\varepsilon_{\min}^{tab}\,k_B T\,,\,\frac{m_e^2}{E_\gamma\,k_B T}\right]\right)}^{\log\left(\max\left[\varepsilon_{\max}^{tab}\,k_B T\,,\,\max\left[\varepsilon_{\min}^{tab}\,k_B T\,,\,\frac{m_e^2}{E_\gamma\,k_B T}\right]\right]\right)} \frac{n_\gamma(k_B T\,\exp(x))}{\exp(x)}$$
$$\int_1^{\frac{\exp(x)\,k_B T\,E_\gamma}{m_e^2}} s_{\mathrm{GS}}\,\sigma_{PP}(s_{\mathrm{GS}})\;\mathrm{d}s_{\mathrm{GS}}\,\mathrm{d}x. \tag{A.15}$$

The last expression above is written in a pseudo-code format corresponding to how it was implemented numerically.

For the differential interaction rate, the logarithmic version for the ε parameter can be expressed as:

$$\gamma_{PP}(E,E') = \pi\,\left(r_e\,m_e^2\right)^2 \int_{\frac{m_e^2}{E_\gamma}}^{\infty}\int_1^{\varepsilon\,E_\gamma/m_e^2} \frac{1}{E_\gamma^2}\frac{n_\gamma(\varepsilon)}{\varepsilon^2}\,s\,\frac{\mathrm{d}\sigma_i}{\mathrm{d}E'}(E,E')\;\mathrm{d}s\;\mathrm{d}\varepsilon \tag{A.16}$$

$$= \pi\,\left(r_e\,m_e^2\right)^2 \int_{\log\left(\frac{m_e^2}{E_\gamma}\right)}^{\infty}\int_1^{\exp(x)\,E_\gamma/m_e^2} \frac{1}{E_\gamma^2}\frac{n_\gamma(\exp(x))}{\exp(x)}\,s\,\frac{\mathrm{d}\sigma_i}{\mathrm{d}E'}(E,E')\;\mathrm{d}s\;\mathrm{d}x. \tag{A.17}$$

Recasting in log values, for s'

Next, we transform the s' parameter (which we will label simply as s in the following) to a logarithmic expression:

$s \to \log(s) = z \quad \Rightarrow \quad s = \exp(z)$,

$\mathrm{d}\log s = \frac{1}{s}\,\mathrm{d}s \quad \Rightarrow \quad \mathrm{d}s = s\,\mathrm{d}\log s$,

so the resulting total interaction rate for the PP process can be written as:

$$\Gamma_{PP}(E_\gamma) = 2\left(\frac{m_e^2}{E_\gamma}\right)^2 \int_{\log\left(\frac{m_e^2}{E_\gamma}\right)}^{\infty} \frac{n_\gamma(\exp(x))}{\exp(x)} \int_{\log(1)}^{\log\left(\frac{\exp(x)E_\gamma}{m_e^2}\right)} \exp(z)^2\,\sigma_{PP}(\exp(z))\;\mathrm{d}z\,\mathrm{d}x. \tag{A.18}$$

A.1.2 Differential interaction rate γ_{PP}

We will use a unitless version of the differential interaction rate:

$$\frac{\mathrm{d}\bar{\sigma}_{PP}}{\mathrm{d}E'_e} \equiv \frac{2}{\pi r_c^2}\frac{\mathrm{d}\sigma_{PP}}{\mathrm{d}E'_e}(s_{\mathrm{GS}}) = \frac{4}{3\,\sigma_T\,m_e^2}\frac{\mathrm{d}\sigma_{PP}}{\mathrm{d}E'_e}(s) \tag{A.19}$$

$$= \frac{1}{s_{\mathrm{GS}}}\frac{1}{E_\gamma}\left[\frac{E'_e}{E_\gamma - E'_e} + \frac{E_\gamma - E'_e}{E'_e} + E_\gamma(1-\beta^2)\left(\frac{1}{E'_e} + \frac{1}{E_\gamma - E'_e}\right)\right.$$
$$\left. - \frac{E_\gamma^2(1-\beta^2)^2}{4}\left(\frac{1}{E'_e} + \frac{1}{E_\gamma - E'_e}\right)^2\right]. \tag{A.20}$$

The differential interaction rate $\gamma(E,E')$ is exactly what it sounds like, defined as:

$$\Gamma_i(E) = \int \mathrm{d}E'\gamma_{ij}(E,E') \tag{A.21}$$

$$\gamma(E,E') = \frac{1}{2}\int \mathrm{d}\varepsilon \int \mathrm{d}\cos\theta\,(1-\cos\theta)\,n_\gamma(\varepsilon)\,\frac{\mathrm{d}\sigma_i}{\mathrm{d}E'}(E,E') \tag{A.22}$$

$$= \pi\,\left(r_c\,m_e^2\right)^2 \int_{\frac{m_e^2}{E_\gamma}}^{\infty}\int_1^{\varepsilon\,E_\gamma/m_e^2} \frac{1}{E_\gamma^2}\frac{n_\gamma(\varepsilon)}{\varepsilon^2}\,s_{\mathrm{GS}}\,\frac{\mathrm{d}\bar{\sigma}_i}{\mathrm{d}E'}(E,E')\;\mathrm{d}s_{\mathrm{GS}}\;\mathrm{d}\varepsilon \tag{A.23}$$

$$= \frac{\left(r_c\,m_e^2\right)^2\,k_BT}{\pi} \int_{\frac{m_e^2}{E_\gamma k_B T}}^{\infty}\int_1^{\varepsilon_0\,k_B\,T\,E_\gamma/m_e^2} \frac{1}{E_\gamma^2}\left(\exp\varepsilon_0 - 1\right)^{-1}\,s_{\mathrm{GS}}\,\frac{\mathrm{d}\bar{\sigma}_i}{\mathrm{d}E'}(E,E')\;\mathrm{d}s_{\mathrm{GS}}\;\mathrm{d}\varepsilon_0. \tag{A.24}$$

One-bin integrated differential interaction rate $\gamma(E,E')$

In order to handle numerical instabilities in the differential interaction rate, we integrate over one energy bin, i.e.:

$$\int_{E'_L}^{E'_R}\mathrm{d}E'\;\gamma(E,E') = \pi\,\left(r_e\,m_e^2\right)^2 \int_{E'_L}^{E'_R}\mathrm{d}E'\;\int_{\frac{m_e^2}{E_\gamma}}^{\infty}\int_1^{\varepsilon\,E_\gamma/m_e^2} \frac{1}{E_\gamma^2}\frac{n_\gamma(\varepsilon)}{\varepsilon^2}\,s_{\mathrm{GS}}\,\frac{\mathrm{d}\bar{\sigma}_i}{\mathrm{d}E'}(E,E')\;\mathrm{d}s_{\mathrm{GS}}\;\mathrm{d}\varepsilon. \tag{A.25}$$

A.2 Interaction rate for Inverse Compton scattering

Figure B.2 in the next Appendix chapter shows the interaction rates for Inverse Compton scattering on the CMB, EBL and URB.

Below, we go into details on the derivations of the interactions rates and energy loss rates that were implemented in the EM module.

A.2.1 Total interaction rate Γ_{IC}

We consider the interaction rate for Inverse Compton scattering.

Following the integration strategy we used for Pair Production above, we start by changing integration variable from $\cos\theta$ to a dimensionless version, this time called s', of the invariant squared total energy-momentum four-vector. This quantity differs slightly from above due to an extra term from the mass of the electron in the process, where we in Pair Production had massless photons as initial particles.

From the invariant squared total energy-momentum four-vector:

$$s = (\vec{P}_i + \vec{P}_j)^2 = 2\varepsilon E_e(1-\cos\theta) + m_e^2,$$

we define a parameterisation:

$$\boxed{s' \equiv \frac{s}{4m_e^2}.}$$

Inserting the definition of s, we get:

$$s' \equiv \frac{\varepsilon E_e(1-\cos\theta)}{2m_e^2} + \frac{1}{4} \;\Leftrightarrow\; \frac{1-\cos\theta}{2} = \left(s' - \frac{1}{4}\right)\frac{m_e^2}{E_e\varepsilon}$$
$$\frac{\mathrm{d}s'}{\mathrm{d}\theta} = \frac{\mathrm{d}}{\mathrm{d}\theta}\left(\frac{\varepsilon E_e(1-\cos\theta)}{2m_e^2} + \frac{1}{4}\right) \;\Leftrightarrow\; \sin\theta\ \mathrm{d}\theta = \left(\frac{2m_e^2}{E_e\varepsilon}\right)\mathrm{d}s'$$

Under this parameterisation, the general expression for the interaction rate transforms to:

$$\Gamma_{IC}(E_e) = \lambda_{IC}^{-1}(E_e) = 2\left(\frac{m_e^2}{E_e}\right)^2 \int_0^\infty \frac{n_\gamma(\varepsilon)}{\varepsilon^2} \int_{\frac{1}{4}}^{\frac{\varepsilon E_e}{m_e^2}+\frac{1}{4}} \left(s' - \frac{1}{4}\right)\sigma_{IC}(s')\ \mathrm{d}s'\ \mathrm{d}\varepsilon.$$

The integration limits are then:

- $\theta_{\min} = 0 \;\rightarrow\; s'_{\min} = \frac{\varepsilon E_e(1-\cos\theta_{\min})}{2m_e^2} + \frac{1}{4} = \frac{1}{4}$
- $\theta_{\max} = \pi \;\rightarrow\; s'_{\max} = \frac{\varepsilon E_e(1-\cos\theta_{\max})}{2m_e^2} + \frac{1}{4} = \frac{\varepsilon E_e}{m_e^2} + \frac{1}{4}.$

For Inverse Compton scattering, there is not a threshold background photon energy ε_{th} in the way there was for Pair Production.

Still following the integration strategy from Pair Production above, we substitute the integration variable $\varepsilon \rightarrow \varepsilon_0 = \frac{\varepsilon}{k_B T}$. As before, we recast the upper integration limit for the inner integral over s' by using the variable, $x(E_e) \equiv \frac{m_e^2}{E_e k_B T}$. This gives us $s'_{\max} = \frac{\varepsilon_0}{x} + \frac{1}{4}$. The interaction rate for Inverse Compton can then be expressed as (analogously to (A.7) above):

$$\Gamma_{IC}(E_e) = \lambda_{IC}^{-1}(E_e) = 2\,\frac{k_B T}{\pi^2}\left(\frac{m_e^2}{E_e}\right)^2 \int_0^\infty (e^{\varepsilon_0}-1)^{-1} \int_{1/4}^{\varepsilon_0/x+1/4} \left(s' - \frac{1}{4}\right)\sigma_{IC}(s')\ \mathrm{d}s'\ \mathrm{d}\varepsilon_0. \quad \text{(A.26)}$$

IC total interaction rate

With the reduced cross section and the integration variable substitutions, we can write the interaction length for IC as integrations over dimensionless quantities, with all the constants out in front:

$$\Gamma_{IC}(E_e) = \lambda_{IC}^{-1}(E_e) = \frac{k_B T}{2\pi}\left(\frac{m_e^2\, r_c}{E_e}\right)^2 \int_0^\infty (e^{\varepsilon_0}-1)^{-1} \int_{1/4}^{\varepsilon_0/x+1/4} \left(s' - \frac{1}{4}\right)\bar{\sigma}_{IC}(s')\ \mathrm{d}s'\ \mathrm{d}\varepsilon_0. \quad \text{(A.27)}$$

Recasting in log:

As above, a logarithmic formulation of the interaction rates is used to optimise the numerical integration computations:

$$\varepsilon \to \log(\varepsilon) = x \quad \Rightarrow \quad \varepsilon = \exp(x),$$
$$\mathrm{d}\log\varepsilon = \tfrac{1}{\varepsilon}\,\mathrm{d}\varepsilon \quad \Rightarrow \quad \mathrm{d}\varepsilon = \varepsilon\,\mathrm{d}\log\varepsilon = \varepsilon\,\mathrm{d}x,$$

which gives us the following expression for the total interaction rate:

$$\begin{aligned}\Gamma_{IC}(E_e) &= \frac{\pi r_c^2}{2}\left(\frac{m_e^2}{E_e}\right)^2 \int_0^\infty \frac{n_\gamma(\varepsilon)}{\varepsilon^2} \int_{1/4}^{\frac{\varepsilon E_e}{m_e^2}+\frac{1}{4}} \left(s' - \frac{1}{4}\right) \bar{\sigma}_{IC}(s')\ \mathrm{d}s'\ \mathrm{d}\varepsilon \\ &= \frac{\pi r_c^2}{2}\left(\frac{m_e^2}{E_e}\right)^2 \int_{\log(\varepsilon_{\min})}^{\log(\varepsilon_{\max})} \frac{n_\gamma(\exp(x))}{\exp(x)} \int_{1/4}^{\frac{\exp(x)E_e}{m_e^2}+\frac{1}{4}} \left(s' - \frac{1}{4}\right) \bar{\sigma}_{IC}(s')\ \mathrm{d}s'\ \mathrm{d}\log\varepsilon.\end{aligned}$$

For the 1-bin integrated differential interaction rate,

$$\int_{E'_L}^{E'_R} \mathrm{d}E'\ \gamma(E,E') = \pi\ \left(r_e\, m_e^2\right)^2 \int_{E'_L}^{E'_R} \mathrm{d}E'\ \int_{\frac{m_e^2}{E_\gamma}}^\infty \int_1^{\varepsilon\, E_\gamma/m_e^2} \frac{1}{E_\gamma^2}\frac{n_\gamma(\varepsilon)}{\varepsilon^2}\frac{\mathrm{d}\sigma_i}{\mathrm{d}E'}(E,E')\ \mathrm{d}s\ \mathrm{d}\varepsilon, \quad \text{(A.28)}$$

the logarithmic version becomes:

$$\begin{aligned}\int_{\log_{10} E'_L}^{\log_{10} E'_R} 10^y\ \log(10)\,\gamma(E,E')\,\mathrm{d}y = \pi\ \left(r_e\, m_e^2\right)^2\ \times \\ \int_{\log_{10} E'_L}^{\log_{10} E'_R} 10^y\ \log(10)\ \mathrm{d}y\ \int_{\log\left(\frac{m_e^2}{E_\gamma}\right)}^\infty \int_1^{\exp(x)\, E_\gamma/m_e^2} \frac{1}{E_\gamma^2}\frac{n_\gamma(\exp(x))}{\exp(x)}\frac{\mathrm{d}\sigma_i}{\mathrm{d}E'}(E_\gamma, 10^y)\ \mathrm{d}s\ \mathrm{d}x\ \mathrm{d}y.\end{aligned} \quad \text{(A.29)}$$

Including the β_i factor:

We investigate the effect of including the (relativistic) velocity of the particle i with energy E_i with respect to the restframe of the photon background that we have otherwise set to 1:

$$s_i = 2\varepsilon E_i(1 - \beta_i\cos\theta) + m_e^2,$$

and define a parameterisation:

$$\boxed{s'_i \equiv \frac{s_i}{4m_e^2},}$$
$$\beta_i \equiv \sqrt{1 - \frac{1}{\gamma_i^2}}, \qquad \gamma_i = \frac{E_i}{m_i}$$

Inserting the definition of s_i, we get:

$$s'_i \equiv \frac{\varepsilon E_i(1-\beta_i\cos\theta)}{2m_e^2} + \frac{1}{4} \;\Leftrightarrow\; \frac{1-\beta_i\cos\theta}{2} = \left(s'_i - \frac{1}{4}\right)\frac{m_e^2}{E_i\varepsilon}$$
$$\frac{\mathrm{d}s'_i}{\mathrm{d}\cos\theta} = \frac{\mathrm{d}}{\mathrm{d}\cos\theta}\left(\frac{\varepsilon E_i(1-\beta_i\cos\theta)}{2m_e^2} + \frac{1}{4}\right) \;\Leftrightarrow\; \mathrm{d}\cos\theta = -\frac{1}{\beta_i}\left(\frac{2m_e^2}{E_i\varepsilon}\right)\mathrm{d}s'_i$$

We substitute these into our general expression for the interaction rate and get:

$$\Gamma_{IC}(E_i) = 2\,\frac{1}{\beta_i}\left(\frac{m_e^2}{E_i}\right)^2 \int_0^\infty \frac{n_\gamma(\varepsilon)}{\varepsilon^2} \int_{s'_{i,\min}}^{s'_{i,\max}} \left(s'_i - \frac{1}{4}\right)\sigma_{IC}(s'_i)\ \mathrm{d}s'_i\ \mathrm{d}\varepsilon.$$

The integration limits are then:

- $\theta_{\min} = 0 \;\rightarrow\; s'_{i,\min} = \frac{\varepsilon E_i(1-\beta_i \cos\theta_{\min})}{2m_e^2} + \frac{1}{4} = \frac{\varepsilon E_i(1-\beta_i)}{2m_e^2} + \frac{1}{4}$
- $\theta_{\max} = \pi \;\rightarrow\; s'_{i,\max} = \frac{\varepsilon E_i(1-\beta_i \cos\theta_{\max})}{2m_e^2} + \frac{1}{4} = \frac{\varepsilon E_i(1+\beta_i)}{2m_e^2} + \frac{1}{4}$

In order to stabilise the numerical treatment of the interaction rate calculation, we series expand $1-\beta_i$ at $\gamma_i = \infty$ (Laurent series):

$$1-\beta_i = 1 - \sqrt{1-\frac{1}{\gamma_i^2}} \quad \simeq \quad 1 - \left(1 - \frac{1}{2\gamma_i^2}\right) \;\simeq\; \frac{1}{2\gamma_i^2},$$

with which we define a function $\bar{\beta}_i(E_e)$:

$$\bar{\beta}_i(E_e) \equiv 1-\beta_i = \begin{cases} 1 - \sqrt{1-\frac{1}{\gamma_i^2}} & \text{if } \gamma_i < 10^3, \\ \frac{1}{2\gamma_i^2} & \text{if } \gamma_i \geq 10^3, \end{cases}$$

For photons, β_i is exactly 1 and thus does not play a role in the calculations of the Pair Production interaction rates.

Our results showed that including this beta factor gave indistinguishable interaction rates from the version with beta set to 1.

A.2.2 IC energy loss length

We next consider the energy loss length for Inverse Compton scattering and take as our starting point the general formula:

$$\begin{aligned} \left(\lambda^{loss}(E)\right)^{-1} &= \frac{1}{E}\frac{dE}{dt} = \frac{1}{E}\int \mathrm{d}E'\,\gamma(E,E')\,(E-E') \\ &= \frac{1}{2}\int \mathrm{d}\varepsilon \int \mathrm{d}\cos\theta\,(1-\cos\theta)\,n_\gamma(\varepsilon)\int \mathrm{d}E'\,\frac{\mathrm{d}\sigma}{\mathrm{d}E'}\left(1-\frac{E'}{E}\right). \end{aligned} \tag{A.30}$$

The differential cross section for an with energy E_e to produce an outgoing electron of energy E'_e is given by [44]:

$$\begin{aligned} \frac{\mathrm{d}\sigma_{IC}}{\mathrm{d}E'_e} &= \sigma_T \cdot \frac{3}{8}\frac{1}{4s'}\frac{1}{E_e}\frac{1+\beta}{\beta}\left[\frac{E'_e}{E_e} + \frac{E_e}{E'_e} + \frac{2(1-\beta)}{\beta}\left(1-\frac{E_e}{E'_e}\right) + \frac{(1-\beta)^2}{\beta^2}\left(1-\frac{E_e}{E'_e}\right)^2\right] \\ \frac{\mathrm{d}\sigma_{IC}}{\mathrm{d}z} &= \pi r_c^2 \frac{1}{4s'}\frac{1+\beta}{\beta}\left[z + z^{-1} + \frac{2(1-\beta)}{\beta}\left(1-z^{-1}\right) + \frac{(1-\beta)^2}{\beta^2}\left(1-z^{-1}\right)^2\right], \end{aligned} \tag{A.31}$$

where in the second line we used the substitution for $z = \frac{E'_e}{E_e} \;\Rightarrow\; \frac{1}{E_e}\,\mathrm{d}E'_e = dz$. The differential cross section is restricted to the range: $\frac{1-\beta}{1+\beta} \leq \frac{E'_e}{E_e} = z \leq 1$. Plugging this into the energy loss length, we get:

$$\left(\lambda_{IC}^{loss}(E_e)\right)^{-1} = \frac{k_B T}{2\pi}\left(\frac{m_e^2\, r_c}{E_e}\right)^2 \int_0^\infty (e^{\varepsilon_0}-1)^{-1} \int_{1/4}^{\varepsilon_0/x+1/4} \left(s'-\frac{1}{4}\right) \int_{\frac{1-\beta}{1+\beta}}^1 \frac{\mathrm{d}\sigma_{IC}}{\mathrm{d}z}\,(1-z)\;\mathrm{d}z\;\mathrm{d}s'\;\mathrm{d}\varepsilon_0,$$

as shown in figure B.2.

A.2.3 Differential interaction rate γ_{IC}

From the general formula in equation (A.24), we get the differential interaction rate for Inverse Compton scattering $\gamma_{IC}(E_e, E'_e)$, in terms of the ingoing and outgoing electron energies E_e and E'_e:

$$\begin{aligned} \gamma^{IC}_{e\to e}(E_e, E'_e) &= \frac{1}{2}\int \mathrm{d}\varepsilon \int \mathrm{d}\cos\theta\,(1-\cos\theta)\,n_\gamma(\varepsilon)\,\frac{\mathrm{d}\sigma_{IC}}{\mathrm{d}E'_e}(E_e, E'_e) \\ &= \frac{k_B T}{2\pi}\left(\frac{m_e^2\, r_c}{E_e}\right)^2 \int_0^\infty (e^{\varepsilon_0}-1)^{-1} \int_{1/4}^{\varepsilon_0/x+1/4} \left(s'-\frac{1}{4}\right)\frac{\mathrm{d}\sigma_{IC}}{\mathrm{d}E'_e}\;\mathrm{d}s'\;\mathrm{d}\varepsilon_0. \end{aligned}$$

Here we again used the definition $x(E_e) \equiv \frac{m_e^2}{E_e k_B T}$.

Differential interaction rate for photons

We use energy conservation (and neglect the low energy of the background photon) to get the differential interaction rate in terms of the energy of outgoing photon: $E'_e = E_e - E'_\gamma$:

$$\gamma^{IC}_{e\to\gamma}(E_e, E'_\gamma) = \frac{1}{2}\int \mathrm{d}\varepsilon \int \mathrm{d}\cos\theta\,(1-\cos\theta)\,n_\gamma(\varepsilon)\,\frac{\mathrm{d}\sigma_{IC}}{\mathrm{d}E'_\gamma}(E_e, E'_\gamma).$$

The differential cross section from equation (A.31) becomes:

$$\frac{\mathrm{d}\sigma_{IC}}{\mathrm{d}E'_\gamma} = \sigma_T \cdot \frac{3}{8}\frac{m_e^2}{s}\frac{1}{E_e}\frac{1+\beta}{\beta}\left[\frac{E_e - E'_\gamma}{E_e} + \frac{E_e}{E_e - E'_\gamma} + \frac{2(1-\beta)}{\beta}\left(1 - \frac{E_e}{E_e - E'_\gamma}\right) + \right. \tag{A.32}$$

$$\left. \frac{(1-\beta)^2}{\beta^2}\left(1 - \frac{E_e}{E_e - E'_\gamma}\right)^2\right]. \tag{A.33}$$

The range that restricts the differential cross section then becomes:

$$\frac{1-\beta}{1+\beta} \le \frac{E'_e}{E_e} \le 1 \quad \to \quad \frac{1-\beta}{1+\beta} \le \frac{E_e - E'_\gamma}{E_e} \le 1 \quad \Leftrightarrow$$

$$0 \le E'_\gamma \le E_e\left(1 - \frac{1-\beta}{1+\beta}\right).$$

A.3 Interaction rate for Inverse Compton scattering: alternative parameterisations

For the IC interaction rate on the CMB, we here present an alternative parameterisation, using a different variant of the squared total energy-momentum for-vector than the s' parameterisation above.

This parameterisation was tested to mitigate numerical instabilities in the computation of the numerical integrals.

A.3.1 Total interaction rate Γ_{IC} – *alternative version*

We introduce the alternative parameterisation:

$$\boxed{s'' \equiv \frac{s}{4m_e^2} - 1/4}$$

$$\text{where still:} \quad s = 2\varepsilon E_e(1-\cos\theta) + m_e^2.$$

Inserting the definition of s, we get:

$$s'' \equiv \frac{\varepsilon E_e(1-\cos\theta)}{2m_e^2} + \frac{1}{4} - \frac{1}{4} \quad \Leftrightarrow \quad \frac{1-\cos\theta}{2} = s''\,\frac{m_e^2}{E_e\varepsilon}$$

$$\frac{\mathrm{d}s''}{\mathrm{d}\theta} = \frac{\mathrm{d}}{\mathrm{d}\theta}\left(\frac{\varepsilon E_e(1-\cos\theta)}{2m_e^2}\right) \Leftrightarrow \sin\theta\,\mathrm{d}\theta = \left(\frac{2m_e^2}{E_e\varepsilon}\right)\mathrm{d}s''$$

We substitute these into our general expression for the interaction rate and get:

$$\Gamma_{IC}(E_e) = \lambda^{-1}_{IC}(E_e) = 2\left(\frac{m_e^2}{E_e}\right)^2 \int_0^\infty \frac{n_\gamma(\varepsilon)}{\varepsilon^2}\int_{s''_{\min}}^{s''_{\max}} s''\,\sigma_{IC}(s')\,\mathrm{d}s''\,\mathrm{d}\varepsilon.$$

The integration limits are then:

- $\theta_{\min} = 0 \;\to\; s''_{\min} = \frac{\varepsilon E_e(1-\cos\theta_{\min})}{2m_e^2} = 0$
- $\theta_{\max} = \pi \;\to\; s''_{\max} = \frac{\varepsilon E_e(1-\cos\theta_{\max})}{2m_e^2} = \frac{\varepsilon E_e}{m_e^2} = \frac{\varepsilon_0}{x}$.

The last equal sign we get from substituting the integration variable $\varepsilon \to \varepsilon_0 = \frac{\varepsilon}{k_B T}$ and using the variable $x(E_e) \equiv \frac{m_e^2}{E_e k_B T}$. We get a factor $k_B T$ from switching to $\mathrm{d}\varepsilon = \mathrm{d}\varepsilon_0\, k_B T$ and a factor $(k_B T)^{-2}$ from the ε^2 in the denominator. The interaction rate for Inverse Compton can then be expressed as (analogously to (A.7) above):

$$\Gamma_{IC}(E_e) = \lambda_{IC}^{-1}(E_e) = \frac{2}{k_B T}\left(\frac{m_e^2}{E_e}\right)^2 \int_0^\infty \frac{n_\gamma(\varepsilon_0\, k_B T)}{\varepsilon_0^2} \int_0^{\varepsilon_0/x} s''\, \sigma_{IC}(s'')\, \mathrm{d}s''\, \mathrm{d}\varepsilon_0 \tag{A.34}$$

Cross section

We also need to rewrite the IC cross section in terms of the parameter s''.

Since $s = 4m_e^2 s'' + m_e^2$, we get:

$$\begin{aligned}
\sigma_{IC}(s) &= \sigma_T \frac{3}{8}\frac{m_e^2}{s} & \frac{1}{\beta}\left[\frac{2}{\beta(1+\beta)}(2+2\beta-\beta^2-2\beta^3) - \frac{1}{\beta^2}(2-3\beta^2-\beta^3)\ln\frac{1+\beta}{1-\beta}\right] \\
&= \pi r_c^2 \frac{m_e^2}{s} & \frac{1}{\beta}\left[\frac{2}{\beta(1+\beta)}(2+2\beta-\beta^2-2\beta^3) - \frac{1}{\beta^2}(2-3\beta^2-\beta^3)\ln\frac{1+\beta}{1-\beta}\right] \\
\sigma_{IC}(s'') &= \pi r_c^2 \frac{m_e^2}{4m_e^2 s'' + m_e^2} & \frac{1}{\beta}\left[\frac{2}{\beta(1+\beta)}(2+2\beta-\beta^2-2\beta^3) - \frac{1}{\beta^2}(2-3\beta^2-\beta^3)\ln\frac{1+\beta}{1-\beta}\right] \\
&= \pi r_c^2 \frac{1}{4s''+1} & \frac{1}{\beta}\left[\frac{2}{\beta(1+\beta)}(2+2\beta-\beta^2-2\beta^3) - \frac{1}{\beta^2}(2-3\beta^2-\beta^3)\ln\frac{1+\beta}{1-\beta}\right]
\end{aligned}$$

And the corresponding reduced cross section becomes $\bar{\sigma}_{IC}(s'')$:

$$\bar{\sigma}_{IC}(s'') \equiv \frac{1}{\pi r_c^2}\, \sigma_{IC}(s'').$$

Finally, we need to rewrite $\beta(s)$:

$$\beta = \frac{s - m_e^2}{s + m_e^2} = \frac{4m_e^2 s'' + m_e^2 - m_e^2}{4m_e^2 s'' + m_e^2 + m_e^2} = \frac{4m_e^2 s''}{4m_e^2 s'' + 2m_e^2} = \frac{2s''}{2s''+1}.$$

IC interaction rate

Now we can write our interaction length using s''. With the reduced cross section and the integration variable substitutions, we can write the interaction length for IC as integrations over dimensionless quantities, with all the constants out in front:

$$\Gamma_{IC}(E_e) = \lambda_{IC}^{-1}(E_e) = 2\,\pi \left(\frac{r_c\, m_e^2}{E_e}\right)^2 \int_0^\infty \frac{n_\gamma(\varepsilon)}{\varepsilon^2} \int_0^{\frac{\varepsilon E_e}{m_e^2}} s''\, \bar{\sigma}_{IC}(s'')\, \mathrm{d}s''\, \mathrm{d}\varepsilon \tag{A.35}$$

$$= 2\,\frac{\pi}{k_B T}\left(\frac{r_c\, m_e^2}{E_e}\right)^2 \int_0^\infty \frac{n_\gamma(\varepsilon_0\, k_B T)}{\varepsilon_0^2} \int_0^{\frac{\varepsilon_0\, k_B T\, E_e}{m_e^2}} s''\, \bar{\sigma}_{IC}(s'')\, \mathrm{d}s''\, \mathrm{d}\varepsilon_0. \tag{A.36}$$

A.3.2 Differential interaction rate γ_{IC} – *alternative version*

In the s''-parameterisation, the differential cross section for an with energy E_e to produce an outgoing electron of energy E_e' becomes:

$$\begin{aligned}
\frac{\mathrm{d}\sigma_{IC}(s)}{\mathrm{d}E_e'} &= \sigma_T \cdot \frac{3}{8}\frac{m_e^2}{s}\frac{1}{E_e}\frac{1+\beta}{\beta}\left[\frac{E_e'}{E_e} + \frac{E_e}{E_e'} + \frac{2(1-\beta)}{\beta}\left(1 - \frac{E_e}{E_e'}\right) + \frac{(1-\beta)^2}{\beta^2}\left(1 - \frac{E_e}{E_e'}\right)^2\right] \\
\frac{\mathrm{d}\sigma_{IC}(s'')}{\mathrm{d}E_e'} &= \pi r_c^2 \frac{1}{4s''+1}\frac{1}{E_e}\frac{1+\beta}{\beta}\left[\frac{E_e'}{E_e} + \frac{E_e}{E_e'} + \frac{2(1-\beta)}{\beta}\left(1 - \frac{E_e}{E_e'}\right) + \frac{(1-\beta)^2}{\beta^2}\left(1 - \frac{E_e}{E_e'}\right)^2\right].
\end{aligned}$$

We use energy conservation (and neglect the low energy of the background photon) to get the differential interaction rate in terms of the energy of outgoing photon: $E_e' = E_e - E_\gamma'$. The differential

cross section from equation (A.33) in the s''-parameterisation becomes:

$$\frac{\mathrm{d}\sigma_{IC}(s'')}{\mathrm{d}E'_\gamma} = \pi r_c^2 \frac{1}{4s''+1}\frac{1}{E_e}\frac{1+\beta}{\beta}\left[\frac{E_e - E'_\gamma}{E_e} + \frac{E_e}{E_e - E'_\gamma} + \frac{2(1-\beta)}{\beta}\left(1 - \frac{E_e}{E_e - E'_\gamma}\right) + \frac{(1-\beta)^2}{\beta^2}\left(1 - \frac{E_e}{E_e - E'_\gamma}\right)^2\right].$$

In the s''-parameterisation, the differential interaction rate can thus be expressed as:

$$\gamma^{IC}_{e\to e}(E_e, E'_e) = 2\,\frac{k_B T}{\pi}\left(\frac{m_e^2 r_c}{E_e}\right)^2 \int_0^\infty (e^{\varepsilon_0} - 1)^{-1} \int_0^{\varepsilon_0/x} s''\,\frac{\mathrm{d}\sigma_{IC}(s'')}{\mathrm{d}E'_e}\,\mathrm{d}s''\,\mathrm{d}\varepsilon_0.$$

Recasting in log: ε and s''

We transform the integration parameters for the total interaction rate from s'' and ε to logarithmic quantities. We begin with ε:

$\varepsilon \to \log(\varepsilon) = x \quad \Rightarrow \quad \varepsilon = \exp(x)$,

$\mathrm{d}\log\varepsilon = \frac{1}{\varepsilon}\mathrm{d}\varepsilon \quad \Rightarrow \quad \mathrm{d}\varepsilon = \varepsilon\,\mathrm{d}\log\varepsilon$,

and likewise for recasting in $\mathrm{d}\log\varepsilon_0$:

$\varepsilon_0 \to \log(\varepsilon_0) = x_0 \quad \Rightarrow \quad \varepsilon_0 = \exp(x_0)$,

$\mathrm{d}\log\varepsilon_0 = \frac{1}{\varepsilon_0}\mathrm{d}\varepsilon_0 \quad \Rightarrow \quad \mathrm{d}\varepsilon_0 = \varepsilon_0\,\mathrm{d}\log\varepsilon_0$,

to obtain the following expression for the interaction rate:

$$\begin{aligned}\Gamma_{IC}(E_e) &= 2\,\pi\left(\frac{r_c\,m_e^2}{E_e}\right)^2 \int_0^\infty \frac{n_\gamma(\varepsilon)}{\varepsilon^2}\int_0^{\frac{\varepsilon E_e}{m_e^2}} s''\,\bar\sigma_{IC}(s'')\,\mathrm{d}s''\,\mathrm{d}\varepsilon \\ &= 2\,\pi\left(\frac{r_c\,m_e^2}{E_e}\right)^2 \int_{\log(\varepsilon_{\min})}^{\log(\varepsilon_{\max})} \frac{n_\gamma(\exp(x))}{\exp(x)}\int_0^{\frac{\exp(x)E_e}{m_e^2}} s''\,\bar\sigma_{IC}(s'')\,\mathrm{d}s''\,\mathrm{d}x \\ &= 2\,\frac{\pi}{k_B T}\left(\frac{r_c\,m_e^2}{E_e}\right)^2 \int_{\log(\varepsilon_{0,\min}\,k_B T)}^{\log(\varepsilon_{\max}\,k_B T)} \frac{n_\gamma(\exp(x_0)\,k_B T)}{\exp(x_0)}\int_0^{\frac{\exp(x_0)\,k_B T\,E_e}{m_e^2}} s''\,\bar\sigma_{IC}(s'')\,\mathrm{d}s''\,\mathrm{d}x_0.\end{aligned}$$

Recasting in log values, for s''

Next, we transform s'' to a logarithmic version. Using:

$s'' \to \log(s'') = z \quad \Rightarrow \quad s'' = \exp(z)$,

$\mathrm{d}\log s'' = \frac{1}{s''}\mathrm{d}s \quad \Rightarrow \quad \mathrm{d}s'' = s''\,\mathrm{d}\log s''$,

we can now write the total interaction rate as:

$$\begin{aligned}\Gamma_{IC}(E_e) &= 2\,\pi\left(\frac{r_c\,m_e^2}{E_e}\right)^2 \int_{\log(\varepsilon_{\min})}^{\log(\varepsilon_{\max})} \frac{n_\gamma(\exp(x))}{\exp(x)}\int_0^{\frac{\exp(x)E_e}{m_e^2}} s''\,\bar\sigma_{IC}(s'')\,\mathrm{d}s''\,\mathrm{d}x \\ &= 2\,\pi\left(\frac{r_c\,m_e^2}{E_e}\right)^2 \int_{\log(\varepsilon_{\min})}^{\log(\varepsilon_{\max})} \frac{n_\gamma(\exp(x))}{\exp(x)}\int_{\log(0)}^{\log\left(\frac{\exp(x)E_e}{m_e^2}\right)} \exp(z)^2\,\bar\sigma_{IC}(\exp(z))\,\mathrm{d}z\,\mathrm{d}x.\end{aligned}$$

A.3.3 Constant integration limits

A final step that can be done with regards to simplifying the integrals prior to numerical evaluation is to convert from variable to constant integration limits for the inner integral over s'.

That would mean transforming the limits $s'_{\min} = 1/4,\ s'_{\max} = \varepsilon_0/x + 1/4 = \frac{\varepsilon_0\,E_e\,k_B T}{m_e^2} + 1/4$ to the constants: $\xi_{\min} = 0,\ \xi_{\max} = 1$.

In the general formula below, the inner integral has an upper limit that depends on the integration variable of the outer integral. To transform to integrals with only constant limits, we define a dimensionless parameter: $0 \leq \xi \leq 1$ and make the following variable substitution: $y = y_0(x) + \xi(y_1(x) - y_0(x))$:

$$\int_{x_0}^{x_1} \mathrm{d}x \int_{y_0(x)}^{y_1(x)} \mathrm{d}y\, f(x,y), \;\; y \to \xi :$$

$$y = y_0(x) + \xi(y_1(x) - y_0(x)) \;\Leftrightarrow\; \xi = \frac{y - y_0}{y_1 - y_0} \;\Rightarrow$$

$$\frac{\mathrm{d}y}{\mathrm{d}\xi} = y_1(x) - y_0(x) \;\Rightarrow$$

$$\int_{x_0}^{x_1} \mathrm{d}x \int_{y_0(x)}^{y_1(x)} \mathrm{d}y\, f(x,y) = \int_{x_0}^{x_1} \mathrm{d}x \int_0^1 \mathrm{d}\xi\, (y_1(x) - y_0(x))\, f(x,\xi).$$

So now, we go to the final version for the interaction rate for IC and perform the corresponding substitution $s'(\xi) = s'_{\min} + \xi \cdot (s'_{\max} - s'_{\min})$:

$$\Gamma_{IC}(E_e) = \frac{k_B T}{2\pi} \left(\frac{m_e^2\, r_c}{E_e}\right)^2 \int_0^\infty (e^{\varepsilon_0} - 1)^{-1} \int_{1/4}^{\varepsilon_0/x + 1/4} \left(s' - \frac{1}{4}\right) \bar{\sigma}_{IC}(s')\; \mathrm{d}s'\; \mathrm{d}\varepsilon_0$$

$$s'(\xi) = s'_{\min} + \xi \cdot (s'_{\max} - s'_{\min}) = 1/4 + \xi \cdot \left(\frac{\varepsilon_0\, E_e\, k_B T}{m_e^2} + 1/4 - 1/4\right) = 1/4 + \xi \left(\frac{\varepsilon_0\, E_e\, k_B T}{m_e^2}\right),$$

$$\frac{\mathrm{d}s'}{\mathrm{d}\xi} = (s'_{\max} - s'_{\min}) = \frac{\varepsilon_0\, E_e\, k_B T}{m_e^2} + 1/4 - 1/4 = \frac{\varepsilon_0\, E_e\, k_B T}{m_e^2}$$

So for $s' \to \xi$:

$$\Gamma_{IC}(E_e) \;\to\; \frac{k_B T}{2\pi} \left(\frac{m_e^2\, r_c}{E_e}\right)^2 \int_0^\infty (e^{\varepsilon_0} - 1)^{-1} \int_0^1 (s'_{\max} - s'_{\min}) \left(s'(\xi) - \frac{1}{4}\right) \bar{\sigma}_{IC}(\xi)\; \mathrm{d}\xi\; \mathrm{d}\varepsilon_0$$

$$= \frac{k_B T}{2\pi} \left(\frac{m_e^2\, r_c}{E_e}\right)^2 \int_0^\infty (e^{\varepsilon_0} - 1)^{-1} \int_0^1 \frac{\varepsilon_0\, E_e\, k_B T}{m_e^2} \left(1/4 + \xi \left(\frac{\varepsilon_0\, E_e\, k_B T}{m_e^2}\right) - \frac{1}{4}\right) \bar{\sigma}_{IC}(\xi, \varepsilon_0, E_e)\; \mathrm{d}\xi\; \mathrm{d}\varepsilon_0$$

$$= \frac{k_B T}{2\pi} \left(\frac{m_e^2\, r_c}{E_e}\right)^2 \int_0^\infty (e^{\varepsilon_0} - 1)^{-1} \int_0^1 \xi \left(\frac{\varepsilon_0\, E_e\, k_B T}{m_e^2}\right)^2 \bar{\sigma}_{IC}(\xi, \varepsilon_0, E_e)\; \mathrm{d}\xi\; \mathrm{d}\varepsilon_0,$$

where now also:

$$\beta(\xi, \varepsilon_0, E_e) = \frac{4 \cdot s'(\xi) - 1}{4 \cdot s'(\xi) + 1} = \frac{\left[1 + 4\xi \left(\frac{\varepsilon_0\, E_e\, k_B T}{m_e^2}\right)\right] - 1}{\left[1 + 4\xi \left(\frac{\varepsilon_0\, E_e\, k_B T}{m_e^2}\right)\right] + 1} = \frac{\left[2\xi \left(\frac{\varepsilon_0\, E_e\, k_B T}{m_e^2}\right)\right]}{\left[1 + 2\xi \left(\frac{\varepsilon_0\, E_e\, k_B T}{m_e^2}\right)\right]},$$

$$\bar{\sigma}_{IC}(\xi, \varepsilon_0, E_e) = \frac{1}{s'(\xi)} \frac{1}{\beta(\xi, \varepsilon_0, E_e)} \left[\frac{2}{\beta(\xi, \varepsilon_0, E_e)(1 + \beta(\xi, \varepsilon_0, E_e))} (2 + 2\beta(\xi, \varepsilon_0, E_e) - \beta(\xi, \varepsilon_0, E_e)^2 - 2\beta(\xi, \varepsilon_0, E_e)^3)\right.$$

$$\left. - \frac{1}{\beta(\xi, \varepsilon_0, E_e)^2} (2 - 3\beta(\xi, \varepsilon_0, E_e)^2 - \beta(\xi, \varepsilon_0, E_e)^3) \ln \frac{1 + \beta(\xi, \varepsilon_0, E_e)}{1 - \beta(\xi, \varepsilon_0, E_e)}\right].$$

In the end, we observed fewest numerical instabilities for the computations of the interaction rates using the s' parameterisation from the main text for the integrals, compared to the alternatives described in this appendix chapter, though they are analytically equivalent.

A.4 Continuous Energy Loss Approximation

In preparation for using the Boltzmann equations in the matrix equation setup in the next appendix chapter, we here derive the continuous energy loss (CEL) approximation.

We introduce the continuous energy loss rate: $\boxed{b(E) = -\frac{dE}{dt} = \langle \Delta E \rangle\, \Gamma(E)}$.

For interactions with only energy gains and losses, and with E as the incoming and E' as the outgoing energy of the particles, we wish to show:

$$\frac{dN_e}{dt} = \boxed{-\Gamma(E)\,N_e(E) + \int_E^\infty \mathrm{d}E'\,\gamma(E',E)\,N_e(E') \;\rightarrow\; \partial_E(b(E)\,N_e(E)).} \tag{A.37}$$

The differential interaction rate:

$$\gamma(E,E') = \frac{1}{2}\int d\,\cos\theta \int_0^\infty d\,\varepsilon\,(1-\cos\theta)\,n_\gamma(\varepsilon)\,\frac{d\,\sigma}{dE'}.$$

From the behaviour of $\gamma(E',E)$, we get to make the substitution:

$$\boxed{\gamma(E,E') \approx \delta(E-E'-\langle\Delta E\rangle)\,\Gamma(E).} \tag{A.38}$$

We now consider two different cases for how $\langle\Delta E\rangle$ depends on energy.

- $\boxed{\textbf{Case 1: } \langle\Delta E\rangle = const. \quad \Rightarrow \quad \partial_E\langle\Delta E\rangle = 0}$

In order to show that:

$$-\Gamma(E)\,N_e(E) + \int_E^\infty \mathrm{d}E'\,\gamma(E',E)\,N_e(E') \;\rightarrow\; \partial_E(b(E)\,N_e(E)), \tag{A.39}$$

we start from the LHS and use the approximation in eqn. (A.38), $\gamma(E,E') \approx \delta(E-E'-\langle\Delta E\rangle)\,\Gamma(E)$, together with the property of the integral over the Dirac delta-function: $\int_a^b f(x)\delta(x-c)\,dx = f(c),\ a \le c \le b$:

$$\begin{aligned}
&-\Gamma(E)\,N_e(E) + \int_E^\infty \mathrm{d}E'\,\boxed{\gamma(E',E)}\,N_e(E') \\
&= -\Gamma(E)\;N_e(E) + \int \mathrm{d}E'\,\boxed{\Gamma(E')\,\delta(E'-(E+\langle\Delta E\rangle))}\,N_e(E') \\
&= -\Gamma(E)\;N_e(E) + \Gamma(E+\langle\Delta E\rangle)\,N_e(E+\langle\Delta E\rangle) \\
&= \langle\Delta E\rangle\left(\frac{-\Gamma(E)\;N_e(E) + \Gamma(E+\langle\Delta E\rangle)\,N_e(E+\langle\Delta E\rangle)}{\langle\Delta E\rangle}\right)
\end{aligned}$$

So if we assume: $\langle\Delta E\rangle = const.$ and $\langle\Delta E\rangle \ll 1$,

we can use the definition of the derivative: $f'(x) = \lim_{\epsilon\to 0}\dfrac{f(x+\epsilon)-f(x)}{\epsilon}$:

$$\begin{aligned}
&= \langle\Delta E\rangle\,\partial_E(\Gamma(E)N_e(E)) \\
&= \partial_E(\langle\Delta E\rangle\,\Gamma(E)\,N_e(E)) = \partial_E(b(E)\,N_e(E)).
\end{aligned}$$

But if $\langle\Delta E\rangle$ is not constant in E, we will need to account for how to go from $\langle\Delta E\rangle\,\partial_E(\Gamma(E)N_e(E)) \rightarrow \partial_E(\langle\Delta E\rangle\,\Gamma(E)\,N_e(E))$.

- $\boxed{\textbf{Case 2: } \langle\Delta E\rangle = xE \textbf{ for } x \ll 1 \quad \Rightarrow \quad \partial_E\langle\Delta E\rangle = x \textbf{ and } \dfrac{\langle\Delta E\rangle}{E} \ll 1.}$

We first insert $\langle\Delta E\rangle = xE$ on equation (2.25).

Starting from the LHS, we use the scaling property of the Dirac Delta-function, $\delta(a\,x) = \frac{\delta(x)}{|a|}$:

$$
\begin{aligned}
&-\Gamma(E)\ N_e(E) + \int \mathrm{d}E'\ \Gamma(E')\,\delta(E' - (E + xE'))\,N_e(E') \\
&= -\Gamma(E)\ N_e(E) + \int \mathrm{d}E'\ \Gamma(E')\,\delta(E'(1-x) - E)\,N_e(E') \\
&= -\Gamma(E)\ N_e(E) + \int \mathrm{d}E'\ \Gamma(E')\,\delta\left((1-x)\left(E' - \frac{E}{(1-x)}\right)\right)\,N_e(E') \\
&= -\Gamma(E)\ N_e(E) + \int \mathrm{d}E'\ \Gamma(E')\,\frac{\delta\left(E' - \frac{E}{(1-x)}\right)}{|1-x|}\,N_e(E') \\
&= -\Gamma(E)\ N_e(E) + \frac{1}{1-x}\Gamma\left(\frac{E}{1-x}\right)\,N_e\left(\frac{E}{1-x}\right) \\
&= -\Gamma(E)\ N_e(E) + \frac{1+x}{(1-x)(1+x)}\Gamma\left(\frac{E(1+x)}{(1-x)(1+x)}\right)\,N_e\left(\frac{E(1+x)}{(1-x)(1+x)}\right) \\
&= -\Gamma(E)\ N_e(E) + \frac{1+x}{1-x^2}\,\Gamma\left(\frac{E(1+x)}{1-x^2}\right)\,N_e\left(\frac{E(1+x)}{1-x^2}\right)
\end{aligned}
$$

Now since $x \ll 1$, we drop the terms that are second-order in x (indicated in red font).

We again use the definition of the derivative: $f'(x) = \lim_{\epsilon\to 0}\frac{f(x+\epsilon)-f(x)}{\epsilon}$:

$$
\begin{aligned}
&= -\Gamma(E)\,N_e(E) + \frac{1+x}{1-x^2}\,\Gamma\left(\frac{E(1+x)}{1-x^2}\right)\,N_e\left(\frac{E(1+x)}{1-x^2}\right) \\
&= -\Gamma(E)\,N_e(E) + (1+x)\,\Gamma(E+Ex)\,N_e(E+Ex) \\
&= \boxed{-\Gamma(E)\,N_e(E) + \Gamma(E+Ex)\,N_e(E+Ex)} + x\,\Gamma(E+Ex)\,N_e(E+Ex) \\
&= \boxed{Ex\,\partial_E(\Gamma(E)\,N_e(E))} + x\,\Gamma(E+Ex)\,N_e(E+Ex) \\
&= Ex\,\partial_E(\Gamma(E)\,N_e(E)) + x\,[Ex\,\partial_E(\Gamma(E)N_e(E)) + \Gamma(E)N_e(E)] \\
&= Ex\,\partial_E(\Gamma(E)\,N_e(E)) + x^2\,E\,\partial_E(\Gamma(E)N_e(E)) + x\,\Gamma(E)N_e(E) \\
&= Ex\,\partial_E(\Gamma(E)\,N_e(E)) + x\,\Gamma(E)N_e(E) \\
&= \langle\Delta E\rangle\,\partial_E(\Gamma(E)\,N_e(E)) + \partial_E(\langle\Delta E\rangle)\,\Gamma(E)N_e(E) \\
&= \partial_E(\langle\Delta E\rangle\,\Gamma(E)\,N_e(E)) \\
&= \partial_E(b\,N_e).
\end{aligned}
$$

$\boldsymbol{\langle\Delta E\rangle = \Delta E}$ in the approximation $\gamma(E,E') \approx \Gamma(E)\delta(E-E'-\Delta E)$, since:

$$
\begin{aligned}
\langle\Delta E\rangle \equiv \frac{b(E)}{\Gamma(E)} &= \frac{\int dE'\,\gamma(E,E')\,(E-E')}{\Gamma(E)} \\
&\text{so if we insert } \gamma(E,E') \approx \Gamma(E)\delta(E-E'-\Delta E): \\
&= \frac{\int dE'\,\Gamma(E)\,\delta(E-E'-\Delta E)\,(E-E')}{\Gamma(E)} \\
&= \frac{\Gamma(E)}{\Gamma(E)}\,(E-(E-\Delta E)) = \Delta E.
\end{aligned}
$$

Continuous energy loss approximation and the energy loss rate

For the case of Inverse Compton scattering, we consider the relation between the continuous energy loss approximation and the energy loss rate. Note that we assume $N_e = N_{e^\pm}$ in the following. Starting from equation (A.37) from above, the IC scattering version can be expressed as:

$$
\frac{\mathrm{d}N_{e^\pm}}{\mathrm{d}t} = -\Gamma_{IC}(E_e)\,N_e(E_e) + \int_{E_e}^{\infty}\mathrm{d}E'_e\,\gamma(E'_e,E_e)\,N_e(E'_e),
$$

where the differential and non-diff. interaction rates are connected by: $\Gamma_{IC}(E_e) = \int \mathrm{d}E'_e\, \gamma(E_e, E'_e)$. With the rate $b(E)$ from above, we can make a connection to the energy loss rate Γ_{loss}:

$$\Gamma_{loss}(E_e) = \frac{1}{E_e}\frac{\mathrm{d}E_e}{\mathrm{d}t}$$
$$b(E_e) \equiv \frac{\mathrm{d}E_e}{dt} \;\Rightarrow\; \boxed{\Gamma_{loss}(E_e) = \frac{b(E_e)}{E_e}.}$$

We can now show how:

$$-\Gamma_{IC}(E_e)\, N_e(E_e) + \int_{E_e}^{\infty} \mathrm{d}E'_e\, \gamma(E'_e, E_e)\, N_e(E'_e) \;\rightarrow\; \partial_{E_e}(b(E_e)\, N_e(E_e)) \rightarrow \Gamma_{loss}(E_e)$$

since:

$$\partial_{E_e}(b(E_e)\, N_e(E_e)) = \partial_{E_e} b(E_e)\; N_e(E_e) \;+\; b(E_e)\, \partial_{E_e} N_e(E_e),$$

where the second term goes to 0, and the first term:

$$\partial_{E_e}(b(E_e)\, N_e(E_e)) \simeq \partial_{E_e} b(E_e)\; N_e(E_e)$$
$$\simeq \partial_{E_e} b(E_e) \;\simeq\; \frac{b(E_e)}{E_e} \;\simeq\; \Gamma_{loss}(E_e).$$

Appendix B

EM module

B.1 Discretisation of Boltzmann equations

B.1.1 Approach for energy discretisation: Integrating over one bin

To get a more precise approximation for the integral over $\gamma^{IC}_{e\to e}(E_j, E_i)$ than the Riemann sums can provide, we integrate over one bin for the **outgoing** energy:

$$\text{From:} \quad \sum_j \Delta E_j \, \gamma(E_j, E'_i) \qquad = \int \mathrm{d}E_j \;\; \gamma(E_j, E'_i)$$

$$\text{to:} \quad \sum_j \Delta E_j \, \frac{1}{\Delta E'_i} \int_{E'_{i,L}}^{E'_{i,R}} \mathrm{d}E'_i \;\; \gamma(E_j, E'_i) \;= \int \mathrm{d}E_j \;\; \gamma(E_j, E'_i),$$

where $E_{i,L}$ designates the left bin-edge of the energy bin i, so that E_i is the center of the bin. Likewise, $E_{i,R}$ is the right bin-edge of the energy bin i, as shown in figure (B.1). The extra factor $\frac{1}{\Delta E'_i}$ makes up for the binwise-integration over the outgoing energy.

We show this for the third term in $n_e(E_i, t + \Delta t)\Delta E_i$ from above, for the IC differential interaction rate in terms of outgoing electrons:

$$\Delta t \Delta E'_i \sum_j \Delta E_j \, \gamma^{IC}_{e\to e}(E_j, E'_i) \, n_e(E_j, t) \;\; \to$$

$$\Delta t \Delta E'_i \sum_j \Delta E_j \, \frac{\int_{E'_{i,L}}^{E'_{i,R}} \mathrm{d}E'_i \;\; \gamma(E_j, E'_i)}{\Delta E'_i} \, n_e(E_j, t),$$

where as before $E_{i,L}$ is the left bin-edge of the energy bin i, $E_{i,R}$ is the right bin-edge of the energy bin i, and E_i is the center of the bin. We get a cancellation of the two energy bin widths $\Delta E'_i$. Compared to our original Boltzmann equations (considering here only IC), we get thus the following:

$$n_e(E, t + \Delta t) = n_e(E, t) - \Delta t \, \Gamma_{IC}(E) \, n_e(E, t) + \Delta t \int \mathrm{d}E_e \, \gamma^{IC}_{e\to e}(E_e, E) \, n_e(E_e, t) \;\; \Rightarrow$$

$$N_{e,i}(t + \Delta t) \simeq N_{e,i}(t) - \Delta t \, \Gamma^{IC}_{e,i} \, N_{e,i}(t) + \Delta t \, \sum_j \left(\int_{E_{i,L}}^{E_{i,R}} \mathrm{d}E_i \;\; \gamma^{IC}_{e\to e}(E_j, E_i) \right) \;\; N_{e,j}(t).$$

We then replace the differential interaction rates with their one-bin integrated counterparts and get the following transfer matrices:

$$
\begin{aligned}
\left[T_{\gamma\gamma}(\Delta t)\right]_{ji} &\equiv \left(1-\Delta t\ \left[\Gamma_{\gamma}^{PP}\right]_i\right)\ \delta_{ji} \\
\left[T_{e\gamma}(\Delta t)\right]_{ji} &\equiv \Delta t\ \left[\int_{E_{i,L}}^{E_{i,R}} \mathrm{d}E_i\ \gamma_{e\to\gamma}^{IC}(E_j,E_i)\right] \\
\left[T_{\gamma e}(\Delta t)\right]_{ji} &\equiv \Delta t\ \left[2\int_{E_{i,L}}^{E_{i,R}} \mathrm{d}E_i\ \gamma_{\gamma\to e}^{PP}(E_j,E_i)\right] \\
\left[T_{ee}(\Delta t)\right]_{ji} &\equiv \left(1-\Delta t\ \left[\Gamma_{e}^{IC}\right]_i\right)\ \delta_{ji}\ +\ \Delta t\ \left[\int_{E_{i,L}}^{E_{i,R}} \mathrm{d}E_i\ \gamma_{e\to e}^{IC}(E_j,E_i)\right] \\
\mathcal{T}(\Delta t) &\equiv \begin{bmatrix} T_{\gamma\gamma}(\Delta t) & T_{e\gamma}(\Delta t) \\ T_{\gamma e}(\Delta t) & T_{ee}(\Delta t)\end{bmatrix}.
\end{aligned}
$$

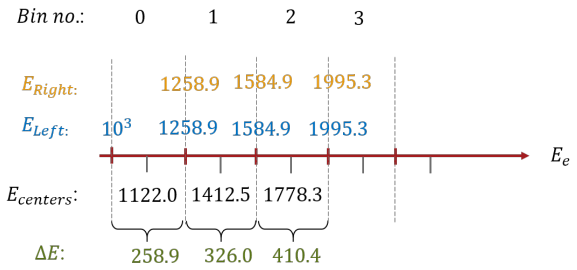

Figure B.1: Energy bins, bin edges and bin widths

B.1.2 Matrix multiplication method

We follow references [58, 23] and employ the matrix doubling method that we elaborate on here.

With the four transfer matrices defined above, we can write the equations for the evolution of spectra of photons and electrons as a matrix equation:

$$
\begin{bmatrix} N_\gamma \\ N_e \end{bmatrix}_i (\Delta t) \simeq \sum_j \begin{bmatrix} T_{\gamma\gamma}(\Delta t) & T_{e\gamma}(\Delta t) \\ T_{\gamma e}(\Delta t) & T_{ee}(\Delta t)\end{bmatrix}_{ji} \begin{bmatrix} N_\gamma \\ N_e \end{bmatrix}_j (0), \tag{B.1}
$$

or equivalently:

$$
\begin{aligned}
N_\gamma(\Delta t) &= T_{\gamma\gamma}(\Delta t)N_\gamma(0) + T_{e\gamma}(\Delta t)N_e(0) \\
N_e(\Delta t) &= T_{\gamma e}(\Delta t)N_\gamma(0) + T_{ee}(\Delta t)N_e(0).
\end{aligned}
$$

If we consider this set of equations at double the time step, $2\Delta t$, we see that:

$$
\begin{aligned}
N_\gamma(2\Delta t) = &\ T_{\gamma\gamma}(\Delta t)N_\gamma(\Delta t) + T_{e\gamma}(\Delta t)N_e(\Delta t) &= &\ T_{\gamma\gamma}(2\Delta t)N_\gamma(0) + T_{e\gamma}(2\Delta t)N_e(0) \\
N_e(2\Delta t) = &\ T_{\gamma e}(\Delta t)N_\gamma(\Delta t) + T_{ee}(\Delta t)N_e(\Delta t) &= &\ T_{\gamma e}(2\Delta t)N_\gamma(0) + T_{ee}(2\Delta t)N_e(0),
\end{aligned}
$$

where this next generation of transfer matrices is given by:

$$
\begin{aligned}
T_{\gamma\gamma}(2\Delta t) &= \left[T_{\gamma\gamma}(\Delta t)\right]\left[T_{\gamma\gamma}(\Delta t)\right] + \left[T_{e\gamma}(\Delta t)\right]\left[T_{\gamma e}(\Delta t)\right] \\
T_{e\gamma}(2\Delta t) &= \left[T_{\gamma\gamma}(\Delta t)\right]\left[T_{e\gamma}(\Delta t)\right] + \left[T_{e\gamma}(\Delta t)\right]\left[T_{ee}(\Delta t)\right] \\
T_{\gamma e}(2\Delta t) &= \left[T_{ee}(\Delta t)\right]\left[T_{\gamma e}(\Delta t)\right]\ + \left[T_{\gamma e}(\Delta t)\right]\left[T_{\gamma\gamma}(\Delta t)\right] \\
T_{ee}(2\Delta t) &= \left[T_{ee}(\Delta t)\right]\left[T_{ee}(\Delta t)\right]\ + \left[T_{\gamma e}(\Delta t)\right]\left[T_{e\gamma}(\Delta t)\right].
\end{aligned}
$$

Since these are equivalent to the square of the original four transfer matrices, we can write:

$$
\begin{bmatrix} N_\gamma \\ N_e \end{bmatrix}_i (2\Delta t) \simeq \sum_j \begin{bmatrix} T_{\gamma\gamma}(\Delta t) & T_{e\gamma}(\Delta t) \\ T_{\gamma e}(\Delta t) & T_{ee}(\Delta t)\end{bmatrix}^2_{ji} \begin{bmatrix} N_\gamma \\ N_e \end{bmatrix}_j (0) \tag{B.2}
$$

$$
\begin{bmatrix} N_\gamma \\ N_e \end{bmatrix} (2\Delta t) \simeq \left[\mathcal{T}(\Delta t)\right]^2 \begin{bmatrix} N_\gamma \\ N_e \end{bmatrix} (0). \tag{B.3}
$$

We generalise this procedure by combining the four original transfer matrices into one transition matrix $\mathcal{T}(\Delta t)$. To compute the fluxes N_γ and N_e after the time interval $2^n\,\Delta t$, we square $\mathcal{T}(\Delta t)$ iteratively n times, so we get:

$$\mathcal{T}(2^n\,\Delta t) = \left[\left[\left[\mathcal{T}(\Delta t)\right]^2\right]^2\right]^{2\,\cdots}{}^2 = \left[\mathcal{T}(\Delta t)\right]^{2^n} \tag{B.4}$$

$$\begin{bmatrix} N_\gamma \\ N_e \end{bmatrix}_i (2^n\,\Delta t) \simeq \sum_j \left[\left[\left[\begin{bmatrix} T_{\gamma\gamma}(\Delta t) & T_{e\gamma}(\Delta t) \\ T_{\gamma e}(\Delta t) & T_{ee}(\Delta t) \end{bmatrix}_{ji}^2\right]^2\right]^{2\,\cdots}{}^2 \begin{bmatrix} N_\gamma \\ N_e \end{bmatrix}_j (0) \tag{B.5}$$

$$\begin{bmatrix} N_\gamma \\ N_e \end{bmatrix} (2^n\,\Delta t) \simeq \left[\left[\left[\begin{bmatrix} T_{\gamma\gamma}(\Delta t) & T_{e\gamma}(\Delta t) \\ T_{\gamma e}(\Delta t) & T_{ee}(\Delta t) \end{bmatrix}^2\right]^2\right]^{2\,\cdots}{}^2 \begin{bmatrix} N_\gamma \\ N_e \end{bmatrix} (0). \tag{B.6}$$

$$\begin{bmatrix} N_\gamma \\ N_e \end{bmatrix} (2^n\,\Delta t) \simeq \left[\left[\left[\mathcal{T}(\Delta t)\right]^2\right]^2\right]^{2\,\cdots}{}^2 \begin{bmatrix} N_\gamma \\ N_e \end{bmatrix} (0). \tag{B.7}$$

So in terms of propagating time steps, this means:

0 time steps — For $t = 0$, we have just the initial spectra $N_\gamma(0) = N_{\gamma,in}, N_{e,in}$ that we input to the cascade module.

1 time step — $\boxed{n = 0}$: After the first time step $t = \Delta t = 2^0\,\Delta t$, we have:

$\begin{bmatrix} N_\gamma \\ N_e \end{bmatrix} (\Delta t) \simeq [T(\Delta t)] \begin{bmatrix} N_\gamma \\ N_e \end{bmatrix} (0)$, corresponding to the exponent $2^n = 2^0 = 1$.

0 matrix multiplications were needed to go 1 time step.

2 time steps — $\boxed{n = 1}$: After 2 time steps, when the interval $t = 2\Delta t = 2^1\,\Delta t$ has elapsed, we have:

$\begin{bmatrix} N_\gamma \\ N_e \end{bmatrix} (2\Delta t) \simeq [T(\Delta t)]^2 \begin{bmatrix} N_\gamma \\ N_e \end{bmatrix} (0)$, corresponding to the exponent $2^n = 2^1 = 2$.

1 matrix multiplication was needed to go 2 time steps.

4 time steps — $\boxed{n = 2}$: After 4 time steps, when the interval $t = 4\Delta t = 2^2\Delta t$ has elapsed, we have:

$\begin{bmatrix} N_\gamma \\ N_e \end{bmatrix} (2^2\Delta t) \simeq \left[[T(\Delta t)]^2\right]^2 \begin{bmatrix} N_\gamma \\ N_e \end{bmatrix} (0)$, corresponding to the exponent $2^n = 2^2 = 4$.

2 matrix multiplications were needed to go 4 time steps.

8 time steps — $\boxed{n = 3}$: After 8 time steps, when the interval $t = 8\Delta t = 2^3\Delta t$ has elapsed, we have:

$\begin{bmatrix} N_\gamma \\ N_e \end{bmatrix} (2^3\Delta t) \simeq \left[\left[[T(\Delta t)]^2\right]^2\right]^2 \begin{bmatrix} N_\gamma \\ N_e \end{bmatrix} (0)$, corresponding to the exponent $2^n = 2^3 = 8$.

3 matrix multiplications were needed to go 8 time steps.

$\vdots$

2^n time steps — $\boxed{n = n}$: After 2^n time steps, when the interval $t = 2^n\Delta t$ has elapsed, we have:

$\begin{bmatrix} N_\gamma \\ N_e \end{bmatrix} (2^n\Delta t) \simeq [T(\Delta t)]^{2^n} \begin{bmatrix} N_\gamma \\ N_e \end{bmatrix} (0)$.

n matrix multiplications were needed to go 2^n time steps.

B.1.3 Comparing γ to the total interaction rate Γ

When we compare the one-bin integrated differential interaction rates to the total interaction rate, we sum the contributions from the one-bin integrals over the **outgoing** energy:

$$\sum_i \int_{E'_{i,L}}^{E'_{i,R}} \mathrm{d}E'_i \ \gamma(E_j, E'_i) = \int \mathrm{d}E'_i \ \gamma(E_j, E'_i) \ = \ \Gamma(E_j).$$

This gives us a way to compare the computation of γ to the computation of Γ for the different interactions and backgrounds and verify whether they agree. See figure B.2 for comparisons of differential and total interactions lengths for Inverse Compton Scattering and figure B.3 for the Pair Production counterpart.

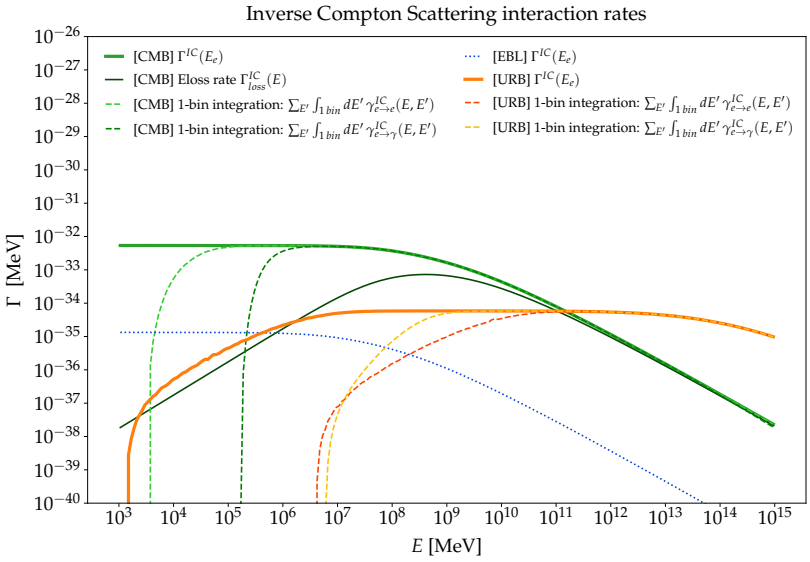

Figure B.2: Inverse Compton scattering interaction rates.

Figure B.2 illustrates why we need to employ the Continuous Energy Loss approximation for Inverse Compton scattering on the CMB: even with the one-bin integration over outgoing energy, the differential interaction rates γ^{IC} on CMB diverge from the total interaction rate Γ^{IC} for the lowest energies.

Even though the same feature occurs for IC on the radio background (URB) as well, as evident from figure B.2, this is not an issue for the computation of the electromagnetic cascades. The issue is avoided since IC on URB is switched off when IC on CMB starts to dominate (at around $E = 10^{11}$ MeV), and this is before the differential interaction rates start to diverge from Γ^{IC} on URB.

For comparison, figure B.3 shows the ideal behaviour of differential vs. total interaction rates: for Pair Production, we get a close match between the two rates along the energy whole range, across the three photon backgrounds, in spite of the limited resolution of the energy grid.

B.2 CEL implementation with Forward Difference

We use a forward difference on the time derivative and for the energy derivative, defined as follows:

$$\partial_t u \approx \frac{u_j^{n+1} - u_j^n}{\Delta t},$$
$$\partial_E u \approx \frac{u_{j+1}^n - u_j^n}{E_{j+1} - E_j}.$$

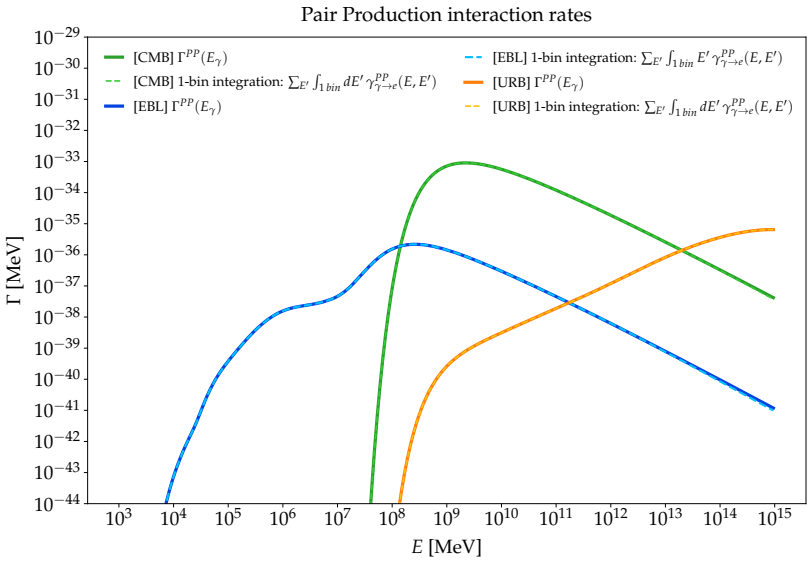

Figure B.3: Pair Production interaction rates.

We begin with the energy derivative. Quick proof of product rule for forward difference:

$$
\begin{aligned}
\Delta_h f(x) &= f(x+h) - f(x) \\
\Delta_h(f*g) &= f*\Delta g + g*\Delta f + \Delta f \Delta g \\
&= f(x)*(g(x+h)-g(x)) + g(x)*(f(x+h)-f(x)) + (f(x+h)-f(x))(g(x+h)-g(x)) \\
&= f(x)g(x+h) - f(x)g(x) + g(x)f(x+h) - g(x)f(x) + f(x+h)g(x+h) - f(x+h)g(x) \\
&\qquad - f(x)g(x+h) + f(x)g(x) \\
&= f(x+h)g(x+h) - f(x)g(x).
\end{aligned}
$$

We use a forward difference on the time derivative and for the energy derivative, respectively:

$$
\begin{aligned}
\partial_t n_e &\simeq \partial_E(b(E)\cdot n_e) \\
&\text{Forward difference:} \\
\frac{n_e(t+\Delta t) - n_e(t)}{\Delta t} &\simeq \frac{b(E_{i+1})n(E_{i+1}) - b(E_i)n(E_i)}{E_{i+1}-E_i} \\
&\simeq \frac{b(E+\Delta E)\, n_e(E+\Delta E) - b(E)\, n_e(E)}{\Delta E} \\
&\simeq \frac{b(E)\, n_e(E) - b(E-\Delta E)\, n_e(E-\Delta E)}{\Delta E} \\
&\simeq \frac{b(E)}{\Delta E}\, n_e(E) - \frac{b(E-\Delta E)}{\Delta E}\, n_e(E-\Delta E) \\
&\simeq \frac{b(E_i)}{E_i - E_{i-1}}\, n(E_i) - \frac{b(E_{i-1})}{E_i - E_{i-1}}\, n(E_{i-1}).
\end{aligned}
$$

Next we set $t=0$ and multiply by ΔE_i^{bin}:

$$
\Delta E_i^{bin} n_e(\Delta t) = \Delta E_i^{bin} n_e(0) + \Delta t \frac{\Delta E_i^{bin}}{\Delta E_{i+1}^{bin}} \frac{b_{i+1}}{E_{i+1}-E_i}\, \Delta E_{i+1}^{bin}\, n_{e,i+1} - \Delta t \frac{b_i}{E_{i+1}-E_i}\, \Delta E_i^{bin}\, n_{e,i},
$$

and set $N_{e,i} = \Delta E_i^{bin}\, n_e(E_i)$:

$$
N_{e,i}(\Delta t) = N_{e,i}(0) + \Delta t \frac{\Delta E_i^{bin}}{\Delta E_{i+1}^{bin}} \frac{b_{i+1}}{E_{i+1}-E_i}\, N_{e,i+1}(0) - \Delta t \frac{b_i}{E_{i+1}-E_i}\, N_{e,i}(0).
$$

For the energy loss parameter b, we use the energy loss length Γ^{IC}_{loss} for Inverse Compton scattering:

$$\Gamma_{loss}(E_e) = \frac{1}{E_e}\frac{\mathrm{d}E_e}{\mathrm{d}t} \quad \Rightarrow$$
$$b(E_i) \equiv \frac{\mathrm{d}E_i}{dt} \;=\; E_i\,\Gamma_{loss}(E_i).$$

With this, we finally get the matrix equation for the CEL approximation for Inverse Compton Scattering:

$$\begin{aligned} N_{e,i}(\Delta t) &\simeq N_{e,i}(0) + \Delta t \frac{\Delta E_i^{bin}}{\Delta E_{i+1}^{bin}} \frac{E_{i+1}}{E_{i+1}-E_i}\,\Gamma_{i+1}^{IC\,loss}\,N_{e,i+1}(0) - \Delta t \frac{E_i}{E_{i+1}-E_i}\,\Gamma_i^{IC\,loss}\,N_{e,i}(0) \\ &= \left[1 - \Delta t \frac{E_i}{E_{i+1}-E_i}\,\Gamma_i^{IC\,loss}\right]\,N_{e,i}(0) + \Delta t \frac{\Delta E_i^{bin}}{\Delta E_{i+1}^{bin}} \frac{E_{i+1}}{E_{i+1}-E_i}\,\Gamma_{i+1}^{IC\,loss}\,N_{e,i+1}(0). \end{aligned} \tag{B.8}$$

The matrix version of our CEL equation can be written as:

$$\begin{aligned} \vec{N}_e(\Delta t) = &\begin{bmatrix} 1-\frac{\Delta t\,E_0}{E_1-E_0}\,\Gamma_0^{IC\,loss} & 0 & 0 & 0 & \dots \\ 0 & 1-\frac{\Delta t\,E_1}{E_2-E_1}\,\Gamma_1^{IC\,loss} & 0 & 0 & \dots \\ 0 & 0 & 1-\frac{\Delta t\,E_2}{E_3-E_2}\,\Gamma_2^{IC\,loss} & 0 & \dots \\ 0 & 0 & 0 & 1-\frac{\Delta t\,E_3}{E_4-E_3}\,\Gamma_3^{IC\,loss} & \dots \\ \vdots & \vdots & \vdots & \vdots & \ddots \end{bmatrix} \vec{N}_e(0) \\ + \Delta t &\begin{bmatrix} 0 & \frac{\Delta E_0^{bin}}{\Delta E_1^{bin}}\frac{E_1}{E_1-E_0}\,\Gamma_1^{IC\,loss} & 0 & 0 & \dots \\ 0 & 0 & \frac{\Delta E_1^{bin}}{\Delta E_2^{bin}}\frac{E_2}{E_2-E_1}\,\Gamma_2^{IC\,loss} & 0 & \dots \\ 0 & 0 & 0 & \frac{\Delta E_2^{bin}}{\Delta E_3^{bin}}\frac{E_3}{E_3-E_2}\,\Gamma_3^{IC\,loss} & \dots \\ 0 & 0 & 0 & 0 & \dots \\ \vdots & \vdots & \vdots & \vdots & \ddots \end{bmatrix} \vec{N}_e(0). \end{aligned}$$

Combining the contributions into one matrix, we get:

$$\vec{N}_e(\Delta t) = \begin{bmatrix} 1-\frac{\Delta t\,E_0}{E_1-E_0}\,\Gamma_0^{IC\,loss} & \frac{\Delta E_0^{bin}}{\Delta E_1^{bin}}\frac{\Delta t\,E_1}{E_1-E_0}\,\Gamma_1^{IC\,loss} & 0 & 0 & \dots \\ 0 & 1-\frac{\Delta t\,E_1}{E_2-E_1}\,\Gamma_1^{IC\,loss} & \frac{\Delta E_1^{bin}}{\Delta E_2^{bin}}\frac{\Delta t\,E_2}{E_2-E_1}\,\Gamma_2^{IC\,loss} & 0 & \dots \\ 0 & 0 & 1-\frac{\Delta t\,E_2}{E_3-E_2}\,\Gamma_2^{IC\,loss} & \frac{\Delta E_2^{bin}}{\Delta E_3^{bin}}\frac{\Delta t\,E_3}{E_3-E_2}\,\Gamma_3^{IC\,loss} & \dots \\ 0 & 0 & 0 & 1-\frac{\Delta t\,E_3}{E_4-E_3}\,\Gamma_3^{IC\,loss} & \dots \\ \vdots & \vdots & \vdots & \vdots & \ddots \end{bmatrix} \vec{N}_e(0).$$

Below we include a section on how to implement this numerically in terms of pseudo code.

Numpy pseduo-code

Here * denotes element-wise multiplication and @ denotes matrix multiplication, and where the energy vectors $\vec{E}$ and $\Delta\vec{E}$ are extended by one extra energy bin in each end of the range in order

to include the entries at the boundaries:

$$\vec{N}_e(\Delta t) = \left[1 - \Delta t \frac{\vec{E}[1:-1]}{\vec{E}[2:] - \vec{E}[1:-1]} * \vec{\Gamma}^{IC\,loss}\right] * \begin{bmatrix} 1 & 0 & 0 & 0 & \dots \\ 0 & 1 & 0 & 0 & \dots \\ 0 & 0 & 1 & 0 & \dots \\ 0 & 0 & 0 & 1 & \dots \\ \vdots & \vdots & \vdots & \vdots & \ddots \end{bmatrix} @\, \vec{N}_e(0) \tag{B.9}$$

$$+ \Delta t \, \frac{\Delta\vec{E}[0:-2]}{\Delta\vec{E}[1:-1]} * \frac{\vec{E}[1:-1]}{\vec{E}[1:-1] - \vec{E}[:-2]} * \vec{\Gamma}^{IC\,loss} * \begin{bmatrix} 0 & 1 & 0 & 0 & \dots \\ 0 & 0 & 1 & 0 & \dots \\ 0 & 0 & 0 & 1 & \dots \\ 0 & 0 & 0 & 0 & \dots \\ \vdots & \vdots & \vdots & \vdots & \ddots \end{bmatrix} @\, \vec{N}_e(0) \tag{B.10}$$

$$\mathtt{N_e(\Delta t)} = \left(\left[1 - \mathtt{\Delta t} \frac{\mathtt{E_i}}{\mathtt{E_{i+1}} - \mathtt{E_i}} \, \Gamma_{\mathtt{i}}^{\mathtt{IC\,loss}}\right] \mathtt{numpy.identity(dim)} + \mathtt{\Delta t} \frac{\mathtt{\Delta E_{i-1}^{bin}}}{\mathtt{\Delta E_i^{bin}}} \frac{\mathtt{E_i}}{\mathtt{E_i} - \mathtt{E_{i-1}}} \, \Gamma_{\mathtt{i}}^{\mathtt{IC\,loss}} \, \mathtt{numpy.eye(dim, k = 1)} \right) @\, \mathtt{N_e(0)}$$

The brackets are to be understood as subsections of the total vectors. An offset of starting points and endpoints for each vector corresponds to the indices i and $i+1$ from equation (B.8).

Since the energy vectors $\vec{E}$ and $\Delta\vec{E}$ are extended by one extra energy bin before and after the energy range, the energy vector for the normal energy range is given by $\vec{E}[1:-1]$: excluding the extra left and extra right energy point, it goes from the the first to the last energy in the normal energy range.

For the first part of the expression above, (B.9), the index i from equation (B.8) becomes the subrange $[1:-1]$. The index $i+1$ likewise becomes $[2:]$. For the second part, (B.10), the index i in equation (B.8) is shifted to $i-1$ (when we change from $N_{e,i+1}(0)$ to $N_{e,i}(0)$) and so becomes the range $[:-2]$. The index $i+1$ is shifted to i and becomes the range $[1:-1]$.

By writing the CEL approximation as a transfer matrix $T_{ee,CEL}$, we can define a new CEL transition matrix that replaces T_{ee} by its CEL counterpart:

$$[T_{ee,CEL}(\Delta t)] \equiv \left[1 - \Delta t \frac{\vec{E}[1:-1]}{\vec{E}[2:] - \vec{E}[1:-1]} \cdot \vec{\Gamma}^{IC\,loss}\right] \cdot \begin{bmatrix} 1 & 0 & 0 & 0 & \dots \\ 0 & 1 & 0 & 0 & \dots \\ 0 & 0 & 1 & 0 & \dots \\ 0 & 0 & 0 & 1 & \dots \\ \vdots & \vdots & \vdots & \vdots & \ddots \end{bmatrix}$$

$$+ \Delta t \, \frac{\Delta\vec{E}[0:-2]}{\Delta\vec{E}[1:-1]} \cdot \frac{\vec{E}[1:-1]}{\vec{E}[1:-1] - \vec{E}[:-2]} \cdot \vec{\Gamma}^{IC\,loss} \cdot \begin{bmatrix} 0 & 1 & 0 & 0 & \dots \\ 0 & 0 & 1 & 0 & \dots \\ 0 & 0 & 0 & 1 & \dots \\ 0 & 0 & 0 & 0 & \dots \\ \vdots & \vdots & \vdots & \vdots & \ddots \end{bmatrix},$$

$$\mathcal{T}_{CEL}(\Delta t) \equiv \begin{bmatrix} T_{\gamma\gamma}(\Delta t) & T_{e\gamma}(\Delta t) \\ T_{\gamma e}(\Delta t) & T_{ee,CEL}(\Delta t) \end{bmatrix}.$$

B.2.1 Determining E_{crit}: Comparing the average energy loss to the energy bin size ΔE_{bin}:

We want to switch from the **exact calculation** to the **CEL approximation** when the loss of energy becomes smaller than the energy bin width ΔE_{bin}.

To investigate when this is, we consider the energy loss and the energy difference $\Delta E_{diff} = E_j - E'_i$, in the following quantity:

$$\langle \Delta E_j \rangle = \frac{\sum_i \left(\gamma^{IC}_{e\to e}(E_j, E'_i)\,(E_j - E'_i)\,\Delta E'_{i,bin} \right)}{\sum_i \gamma^{IC}_{e\to e}(E_j, E'_i)\Delta E'_{i,bin}} = \frac{\int \mathrm{d}E'_i\, \gamma^{IC}_{e\to e}(E_j, E'_i)\,(E_j - E'_i)}{\int \mathrm{d}E'_i\, \gamma^{IC}_{e\to e}(E_j, E'_i)},$$
$$= \frac{\Gamma^{IC}_{loss}(E_j)\cdot E_j}{\Gamma^{IC}(E_j)},$$

where the energy loss rate is defined as:

$$\Gamma^{IC}_{loss}(E_j) \equiv \frac{1}{E_j}\frac{dE_j}{dt} = \frac{1}{E_j}\int \mathrm{d}E'_i\, \gamma(E_j, E'_i)\,(E_j - E'_i),$$

and the total interaction rate is:

$$\Gamma^{IC}(E_j) \equiv \int \mathrm{d}E'_i\, \gamma(E_j, E'_i).$$

In Python, considering the first sum in the expression above:

$$\sum_i \gamma_{ee}(E_j, E'_i)\,(E_j - E'_i)\,\Delta E'_i, \tag{B.11}$$

- where $\gamma_{ee}(E_j, E'_i)$ is a $j \times i$ matrix, array shape (j,i)
- E_j is a column vector $j \times 1$, array shape (j,)
- E'_i and $\Delta E'_i$ are row vectors $1 \times i$, array shape (i,),

we can treat it as either a sum or simply as the matrix multiplication (denoted by the equivalent operations @ or `numpy.dot`):

$$\sum_i \gamma_{ee}(E_j, E'_i)\,(E_j - E'_i)\,\Delta E'_i = \texttt{sum}\,(\,\gamma_{ee}[:, i] * (E_j - E'_i[i]) * \Delta E'_i[i]\,)\ \texttt{for i in range(len(E'}_\texttt{i}\texttt{))}$$
$$= \gamma_{ee}\ @\ (\,(E_j - E'_i) * \Delta E'_i\,)\,.$$

When the input and output energy vectors are over the same range, $E_j - E'_i$ becomes 0, and we stick to method 1 (summing).

We compare this to the energy bin width ΔE_{bin}:

$$\langle \Delta E_i \rangle < \Delta E_{bin} \quad \Leftrightarrow \quad \frac{\langle \Delta E_i \rangle}{\Delta E_{bin}} < 1$$
$$E_{cr} \equiv E^*_i \text{ for which } \frac{\langle \Delta E^*_i \rangle}{\Delta E_{bin}} < 1$$

B.3 Results from the EM module

This section contains additional plots to the ones in section 4.2. We show here the results from applying our EM module to simple input spectra of either photons only, electrons/positrons only or both, with $\frac{\mathrm{d}N}{\mathrm{d}E} \sim E^{-2}$, for a selection of different cases in three groupings.

The first three plots, figures B.4-B.6, showcase the results for the CMB photon background only.

The subsequent two plots, figures B.7-B.8, contain the results from including all three photon backgrounds.

The last plot, fig. B.9 shows the effect of only using the Pair Production process on the CMB. As the interpolation only applies to the Inverse Compton scattering process, the interpolation is left out here.

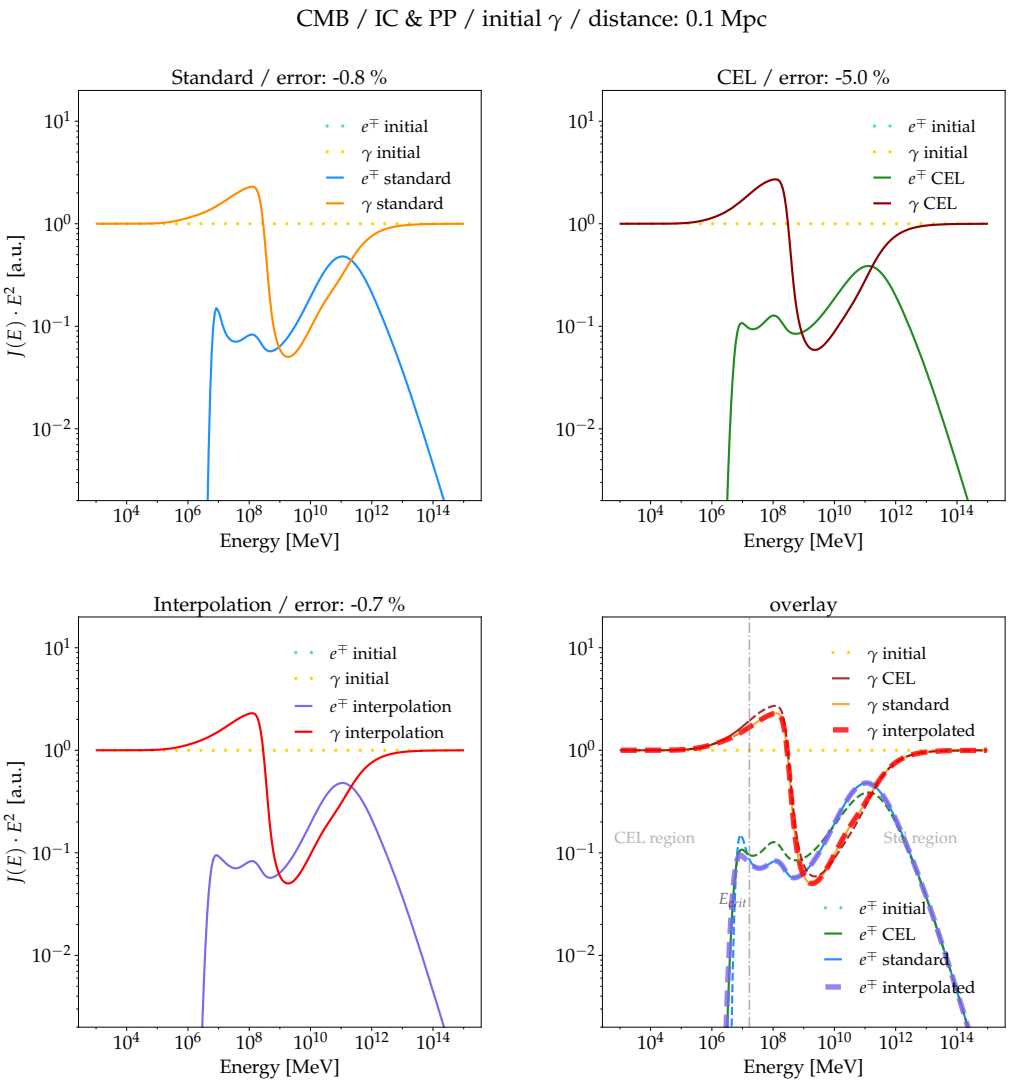

Figure B.4: IC+PP on CMB: for initial photons only.

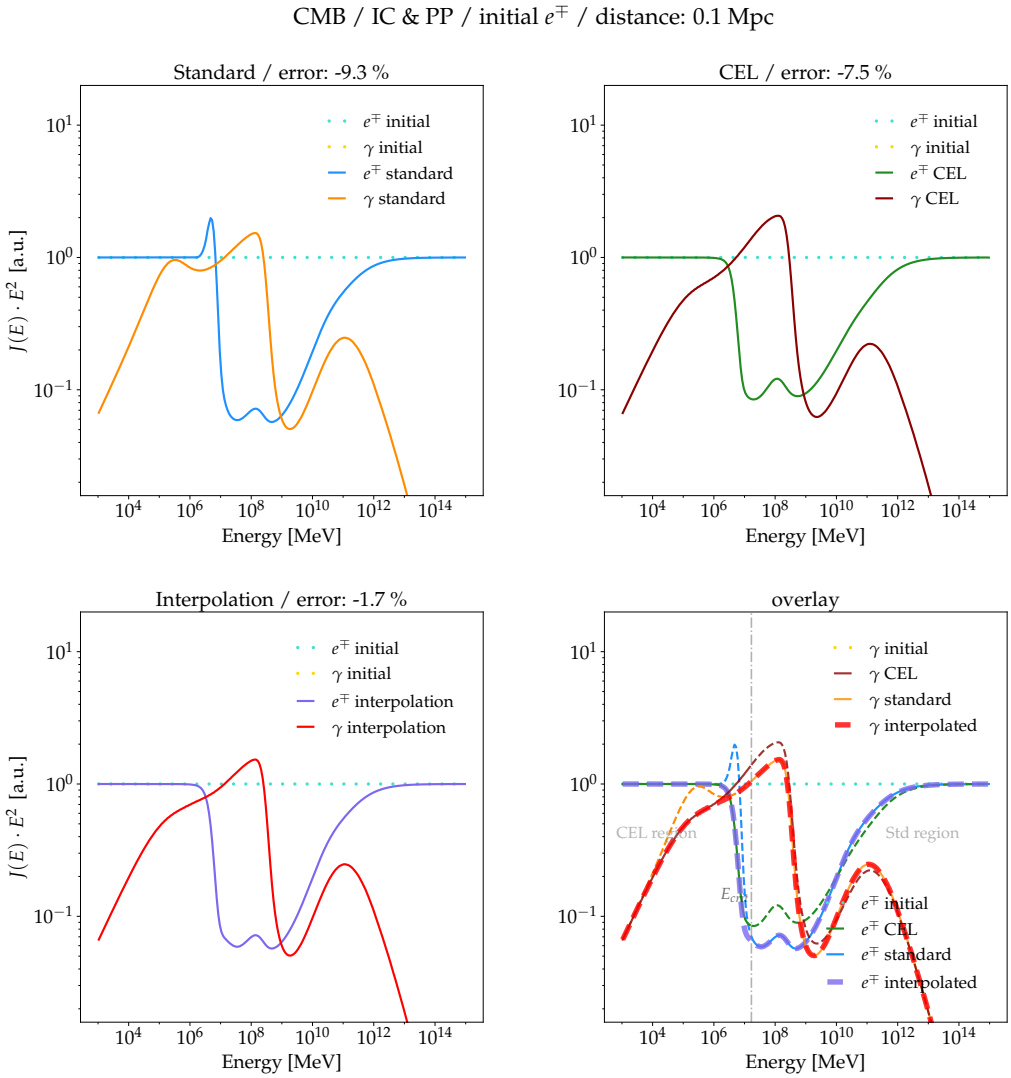

Figure B.5: IC+PP on CMB: for initial electrons/positrons only.

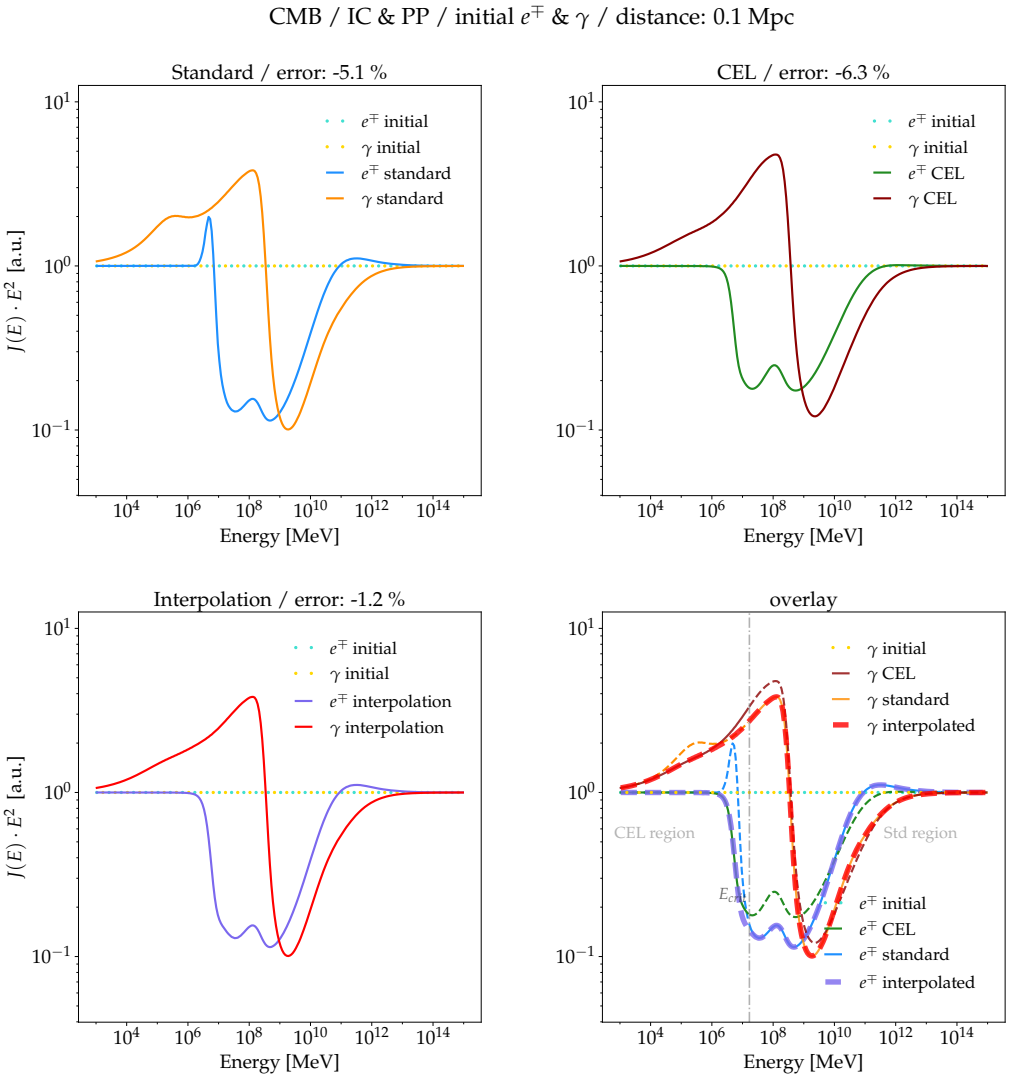

Figure B.6: IC+PP on CMB: for initial photons and electrons/positrons.

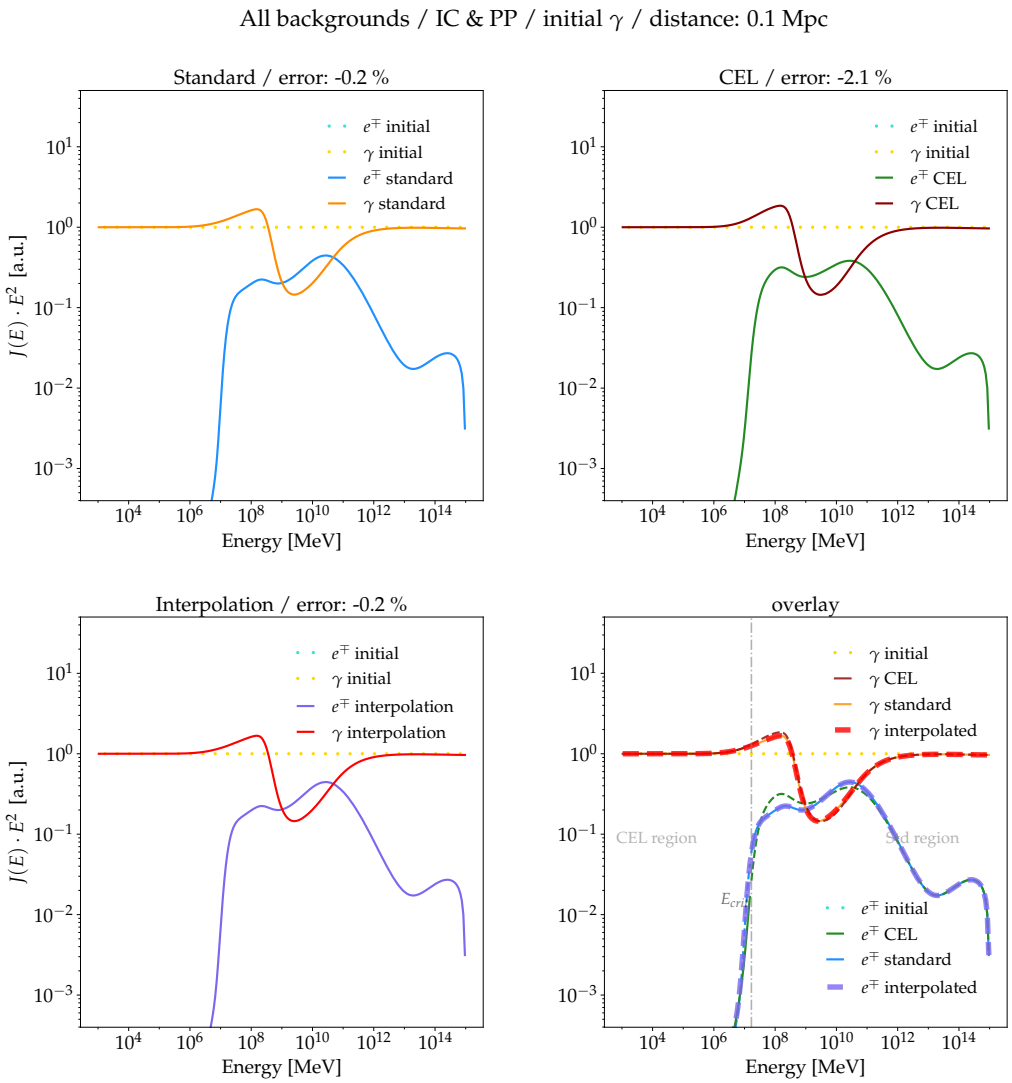

Figure B.7: All backgrounds – photons: IC and PP for initial photons only on all three photon backgrounds: CMB, EBL and URB.

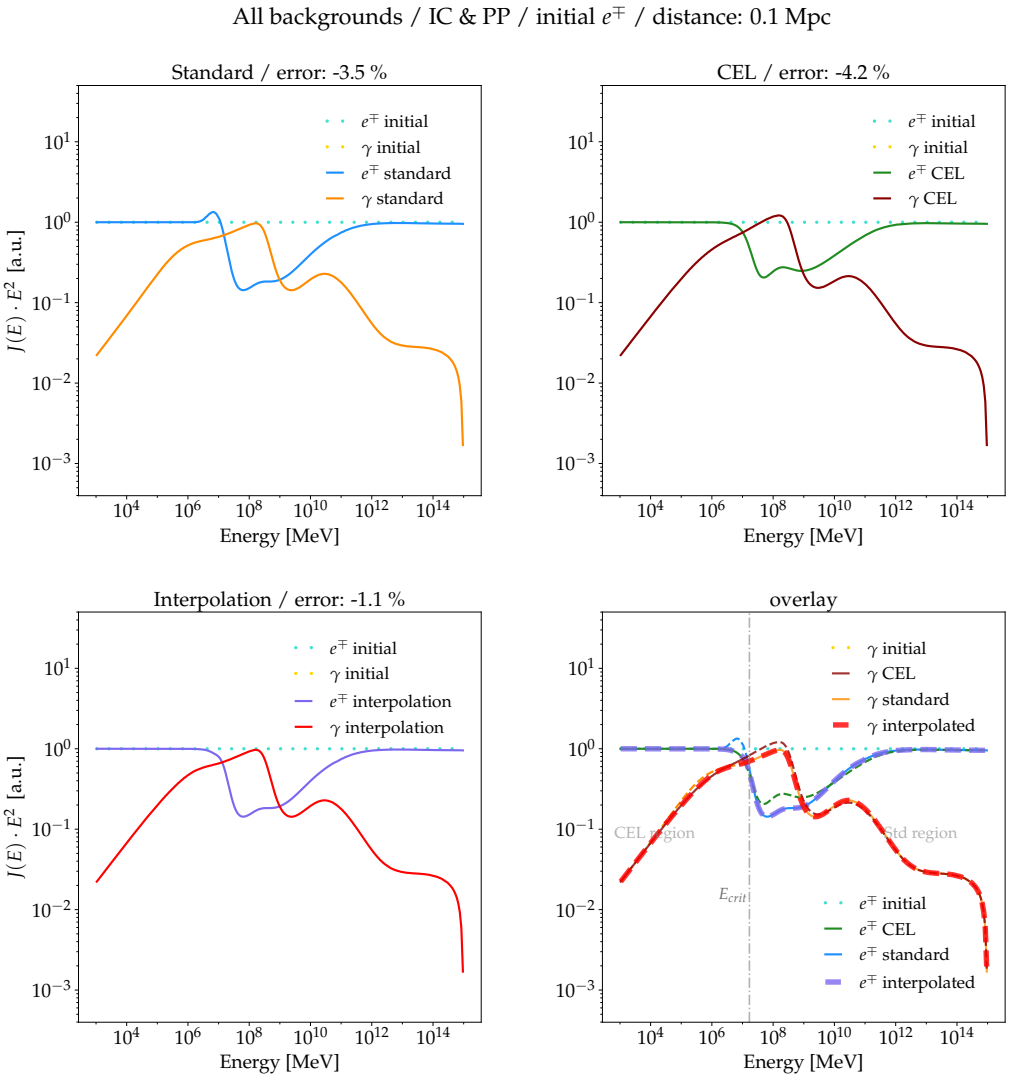

Figure B.8: All backgrounds – electrons: IC and PP for initial electrons only on all three photon backgrounds: CMB, EBL and URB.

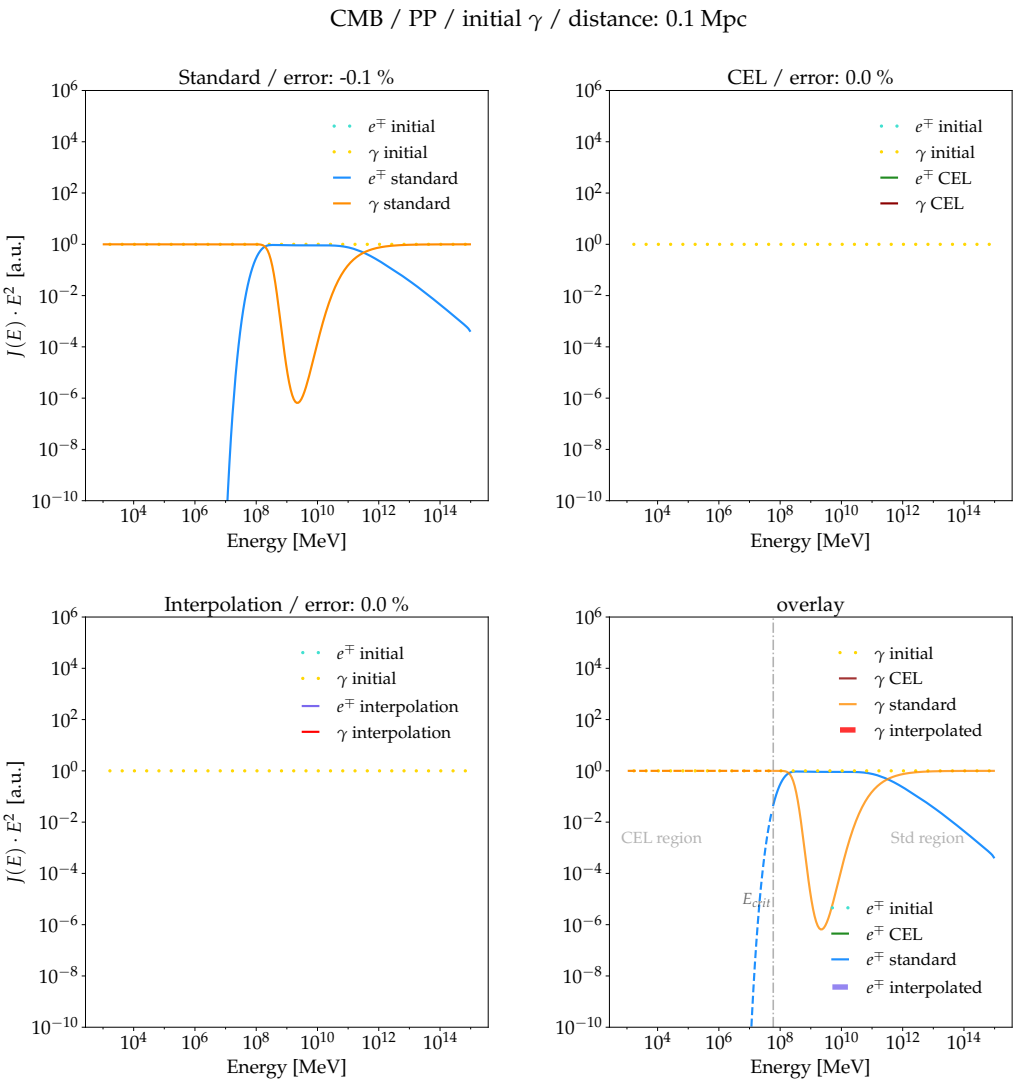

Figure B.9: PP on CMB: for initial photons only. The interpolation does not apply for Pair Production and is left out here.

Appendix C

ICRC 2021 Proceedings

The following conference proceedings are from the 37th International Cosmic Ray Conference 2021 [8].

PROCEEDINGS OF SCIENCE

ONLINE ICRC 2021
THE ASTROPARTICLE PHYSICS CONFERENCE
Berlin | Germany
37th International Cosmic Ray Conference
12–23 July 2021

Improved Limits on Cosmogenic Fluxes from Ultra-High Energy Cosmic Rays

Kathrine Mørch Groth,* **Yoann Genolini and Markus Ahlers**

Niels Bohr Institute, University of Copenhagen, DK-2100 Copenhagen, Denmark
E-mail: xsq168@alumni.ku.dk

Ultra-high energy cosmic rays (UHE CRs) interacting with the cosmic radiation background produce two cosmogenic messengers: neutrinos with energies in the EeV range and gamma rays accumulating in the GeV-TeV range. The most optimistic scenario for cosmogenic fluxes assumes the dominance of protons above the Greisen-Zatsepin-Kuzmin threshold of resonant scattering with photons in the cosmic microwave background. Whereas these optimistic cosmogenic fluxes are testable with present observatories, the corresponding predictions of heavier UHE CR composition models are orders of magnitude smaller, falling within the domain of more sensitive future detectors. In this study we use the latest results of the Pierre Auger observatory for the UHE CR spectrum and chemical composition to derive conservative lower limits on the cosmogenic neutrino and gamma ray fluxes. We investigate the prospects and requirements of future large-scale neutrino and CR observatories to observe these fluxes.

37th International Cosmic Ray Conference (ICRC 2021)
July 12th – 23rd, 2021
Online – Berlin, Germany

*Presenter

PoS(ICRC2021)1005

1. Introduction

The propagation of ultra-high energy (UHE) cosmic rays (CRs) is affected by their interactions with cosmic radiation backgrounds. Above an energy of $E_{\rm GZK} \simeq 50$ EeV CR protons scatter resonantly with photons of the cosmic microwave background (CMB) via the $\Delta(1232)$ resonance whereas CR nuclei are photo-dissociated via the giant dipole resonance (GDR). This limits the propagation distance to about 100-200 Mpc [1, 2]. The observed spectrum above $E > E_{\rm GZK}$ is therefore expected to receive contributions only from local cosmic ray sources.

Pion production via photo-hadronic processes above $E_{\rm GZK}$ is visible in the form of cosmogenic neutrinos and γ-rays in the EeV energy range [3]. These fluxes are guaranteed contributions to the cosmic neutrino and γ-ray backgrounds that follow directly from the observation of UHE CRs and the existence of cosmic photon backgrounds. In particular, cosmogenic neutrinos are one of the main targets of next-generation neutrino observatories that are sensitive in the EeV energy range. The detection (or upper limits) of these neutrinos can provide valuable information about the composition of UHE CRs and hence their possible sources.

Cosmogenic flux predictions in the EeV range have a strong dependence on the mass composition of UHE CRs above $E_{\rm GZK}$. To estimate the required flux sensitivity of future neutrino observatories, it is of general interest to derive a *minimal* contribution consistent with the observed UHE CR spectra and composition. We follow here the idea of Ref. [4] that lower limits on cosmogenic fluxes can be estimated from the *observed* composition of UHE CRs, rather than the *initial* chemical composition at the source – information that gets rapidly washed out by GDR cascades.

In these proceedings, we will reevaluate the results of Ref. [4] using recent observations of the Pierre Auger observatory and state-of-the-art CR propagation models. We will start in section 2 with a summary of cosmic ray propagation effects and emission of cosmogenic contributions. We will then give an estimate of cosmogenic neutrino and γ-ray spectra in section 3 that are based on the observed UHE CR spectrum and the average *observed* mass composition above $E_{\rm GZK}$. We then conclude in section 4.

2. Propagation of UHE CR Nuclei

Over sufficiently large distances, the distribution of UHE CR sources can be treated as continuous and homogeneous. In this case, the evolution of the flux of UHE CR nuclei is governed by a set of (Boltzmann) continuity equations of the form

$$\dot{Y}_i = \partial_E(HEY_i) + \partial_E(b_i Y_i) - \Gamma_i^{\rm tot} Y_i + \sum_j \int {\rm d}E_j \, \gamma_{ji} Y_j + \mathcal{L}_i \,, \tag{1}$$

where Y_i is the comoving number density of particle type i related to the physical density n_i as $Y_i = (1+z)^{-3} n_i$. We assume the standard flat ΛCDM universe with Hubble rate $H^2 = H_0^2(\Omega_\Lambda + \Omega_M (1+z)^3)$ with $\Omega_M = 0.31$, $\Omega_\Lambda = 0.69$ and $H_0 \simeq 67\,{\rm km\,s^{-1}\,Mpc^{-1}}$ [5]. Redshift and coordinate time are related as $\dot{z} = -(1+z)H$. The first two terms on the r.h.s. of Eq. (1) describe energy loss via cosmic expansion and other continuous energy losses defined via $b_i = -{\rm d}E/{\rm d}t$. The third and forth term describe particle losses via inelastic interactions with total rates $\Gamma_i^{\rm tot}$ and generations $j \to i$ via differential interaction rates γ_{ji}. The last term $\mathcal{L}_i$ denotes the comoving emission rate

density of particle type i. The detailed derivation of the interaction rates and energy losses from a given photon background is discussed, *e.g.* in Refs. [6, 7].

The relevant interactions for UHE CR nuclei during propagation are interactions with the cosmic radiation backgrounds. Besides the CMB there are also infra-red to ultra-violet contributions at higher energies [8, 9] as well as radio backgrounds at lower energies [10, 11] from the emission of stars and (active) galaxies. At energies of the CR *ankle* the dominant interaction is continuous energy loss via Bethe-Heitler pair production [12] in the CMB. This process is a coherent interaction of the UHE CR nucleons. Compared to the proton case with energy loss $b_p(z, E)$, the loss of heavy nuclei with mass number A and charge Z scales as $b_A(E) \simeq Z^2 b_p(E/A)$.

At higher energies the propagation of UHE CR nuclei is dominated by photo-disintegration [13, 14]. Rapid interactions of UHE CR nuclei with CMB photons via the giant dipole resonance (GDR) lead to the nucleon losses such as $A \rightarrow (A-1)+N$ or $A \rightarrow (A-2)+2N$ where N indicates the disintegrated nucleons. The resonance lies at about 20 MeV in the rest frame of the nucleus, corresponding to a CR energy of $E \simeq 2 \times 10^{10}/\epsilon_{\rm meV}$ GeV, where $\epsilon_{\rm meV}$ is the background photon energy in units of meV.

At the highest energies, when the photon wavelength becomes smaller than the size of the nucleus, the photon interacts with substructures like quasi-deuterons. This channel forms a plateau above about 30 MeV in the nucleus rest frame that extends up to the pion production threshold at about 145 MeV [15]. Resonant pion production of UHE CR protons, in particular via $\Delta(1232)$, as well as the GDR of UHE CR nuclei with CMB photons both peak at energies of a few 10^{10} GeV. Hence, independent of the chemical composition of UHE CRs we expect a cutoff (or break) in the flux of UHE CRs around $E_{\rm GZK} \simeq 50$ EeV as first pointed out by Greisen, Zatsepin and Kuzmin (GZK) [1, 2].

Photo-hadronic interactions above the pion production threshold are the dominant channels for the production of cosmogenic neutrinos and γ-rays [3]. The rapidly increasing rates at energies around 5×10^{10} GeV are due to resonances with CMB photons, in particular $p + \gamma \rightarrow \Delta(1232) \rightarrow n + \pi^+$. At higher energies multi-pion production becomes relevant which forms a plateau in the cross section. In the case of UHE CR nuclei we can approximate the energy loss from photo-nucleon interactions above pion production threshold as $b_{A,\gamma\pi}(E) \simeq A b_{p,\gamma\pi}(E/A)$. However, see the discussion in Ref. [16].

Pions produced in photo-hadronic interactions decay via $\pi^+ \rightarrow \mu^+ + \nu_\mu$ and $\mu^+ \rightarrow e^+ + \nu_e + \bar{\nu}_\mu$ and the charged conjugate processes. The total flux of neutrinos depends on the source spectrum, composition and evolution. In general, lighter compositions and larger maximal energies with hard spectra ($\gamma \simeq 2$) predict higher cosmogenic neutrino fluxes since the pion production threshold scales with atomic mass number. Since the UHE CR spectrum at the highest energies can only receive contributions from local sources ($r \lesssim 200$ Mpc) a strong redshift evolution of the sources with an increased contribution to neutrinos is also feasible.

Cosmogenic neutrinos and γ-rays have been studied by various authors for the case of pure-proton models [3, 17–23] and also mixed composition models including heavy nuclei [24–34]. In these proceedings we follow the ansatz of Ref. [4] and derive lower limits on the cosmogenic neutrino contributions which are based on the *observed* composition of UHE CRs, rather than the *inferred* composition at the sources.

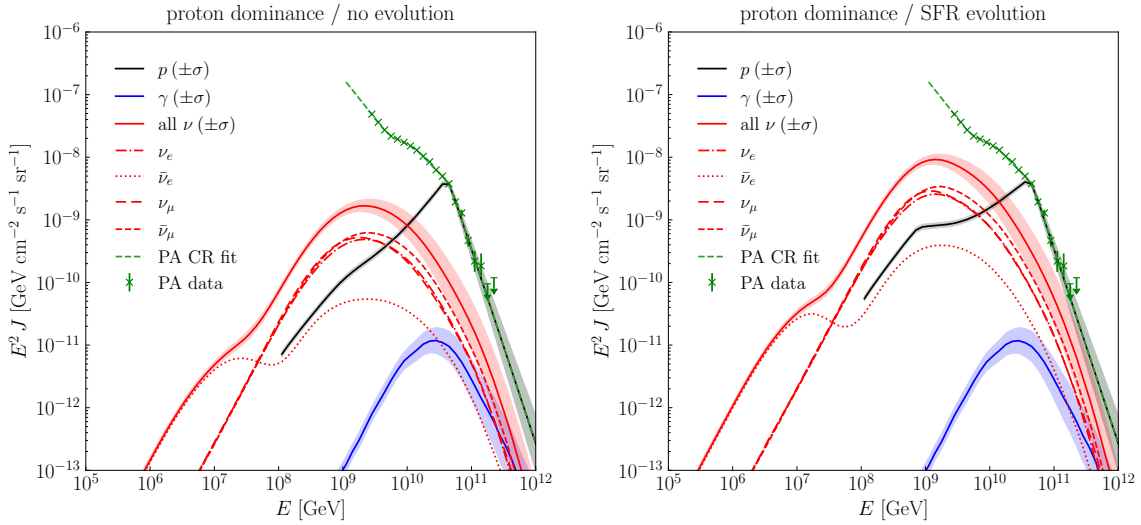

Figure 1: Cosmogenic neutrino and γ-ray fluxes from UHE CR above 50 EeV assuming proton dominance. The proton flux (black line) is fixed to the best-fit spectrum from Pierre Auger [35, 36] (dashed green line). We show results for a constant comoving number density of sources ("no evolution"; left plot) and comoving number density following the star formation rate ("SFR evolution"; right plot). The γ-ray flux (blue lines) are attenuated by pair production in the CMB. We also show the contribution of individual neutrino flavors on production.

3. Minimal Cosmogenic Contributions

The fluxes of cosmogenic neutrinos and γ-rays in the EeV energy range are produced by photo-hadronic interactions of cosmic ray nuclei with energies $E_{\rm CR} \gtrsim A \times 50$ EeV. To first order, the cross section of this process can be approximated as the incoherent superposition of subprocesses involving the scattering of A nucleons with energy $E_{\rm CR}/A$. The only competing process at these high energies are photo-disintegration of heavy nuclei. The latter process (approximately) conserves the Lorentz boost of secondary nuclei and hence the energy per nucleon.

These two arguments show that the production of cosmogenic fluxes in the EeV range is determined by the UHE CR nucleon spectrum above the nucleon energy $E_{\rm N} \gtrsim 50$ EeV. This flux can be estimated from recent observations on the Pierre Auger Observatory [35]. The cosmic ray spectrum at these energies can be approximated by a soft power-law, $J(E_{\rm CR}) \propto E_{\rm CR}^{-\gamma}$ with $\gamma \simeq 5.2 \pm 0.4$. We will assume in the following that the CR flux above this energy is dominated by the *observed* mass group $A_{\rm o}$. The nucleon spectrum above 50 EeV is therefore approximately

$$J_{\rm N}(E_{\rm N}) \simeq A_{\rm o}^2 J_{\rm CR}(A_{\rm o} E_{\rm N}) \simeq A_{\rm o}^{2-\gamma} J_{\rm CR}(50\ {\rm EeV}) \left(\frac{E_{\rm N}}{50\ {\rm EeV}}\right)^{-\gamma}, \qquad (2)$$

with $50\ {\rm EeV} \times J_{\rm CR}(50\ {\rm EeV}) \simeq 0.018\,{\rm km^{-2} sr^{-1} yr^{-1}}$. In the following we will derive cosmogenic fluxes assuming proton dominance above 50 EeV. Other mass compositions follow the same energy spectra as the protons rescaled by the factor $A_{\rm o}^{2-\gamma}$. For instance, for helium we expect only about 1.2% of the cosmogenic neutrino flux with respect to the proton case.

For our fit of the UHE CR nucleon spectrum we approximate the source term in Eq. (1) in the form $\mathcal{L}_{\rm N}(z, E_{\rm N}) = \mathcal{H}(z) Q_{\rm N}(E_{\rm N})$, where $\mathcal{H}$ accounts for the redshift evolution of comoving

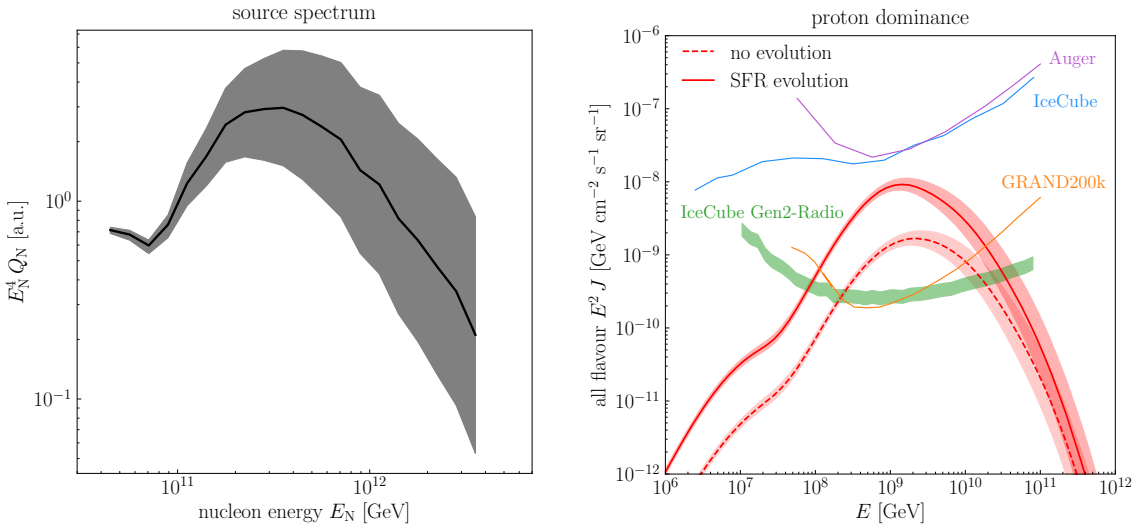

Figure 2: Left panel: Reconstructed source spectrum of UHE CR nucleons (arbitrary units). The source spectrum is practically identical for the two source evolution cases shown in Fig. 1 and follow a soft spectrum in the vicinity of E^{-4}. **Right panel:** Summary of cosmogenic neutrino fluxes assuming proton dominance of UHE CR protons above 50 EeV. We compare the expected fluxes for constant comoving source number density ("no evolution"; dashed red line) and source density evolution following the star formation rate ("SFR evolution"; solid red line). These flux predictions are consistent with limits from IceCube [37] and and Pierre Auger [38] and are in reach of future observatories, such as GRAND200k [39] and IceCube-Gen2 [40].

source density and $Q_N(E)$ denotes the nucleon spectral emission rate from an individual source. We consider two source evolution scenarios in the following: *i)* The case "no evolution" considers a constant comoving number density of UHE CR sources, $\mathcal{H}(z) = \mathcal{H}(0)$, in the redshift range $0 \leq z \leq 4$. This is our most pessimistic scenario in terms of the production of cosmogenic neutrinos and γ-rays. *ii)* The case "SFR evolution" is a less conservative choice where the source evolution follows the star-formation rate (SFR) $\mathcal{H}_{\rm SFR}(z) \propto (1+z)^{n_i}$ with $n_1 = 3.4$ for $z < 1$ and $n_2 = -0.3$ for $1 < z < 4$ [41, 42].

We use the Monte-Carlo code CRPROPA [43] to determine the secondary emission of UHE CR sources. Figure 1 shows the resulting fit to the UHE CR spectrum above 50 EeV provided by Pierre Auger [35, 36]. The calculation assumes proton dominance in the observed spectrum, $A_o = 1$, at these energies. Note that the CR emission spectrum above 50 EeV produces a tail of CR nucleons in the observed spectrum that extends below this energy threshold. These CR nucleons are related to secondary cosmic rays from photo-hadronic processes in the CMB. The left panel of Fig. 2 also shows our best-fit spectrum of CR nuclei above 50 EeV. The emission is soft with a spectral index that follows approximately $\gamma \simeq 4$.

Figure 1 shows also the corresponding flux of cosmogenic neutrinos and γ rays as red and blue bands, respectively, that accounted for the statistical uncertainty of the power-law fit [35, 36] (green dashed lines). While pion production produces neutrinos and γ-rays with comparable intensity, the observable γ-ray fluxes are reduced by e^+e^- pair production in the CMB. Source evolution of UHE CR sources following the SFR (left panel) provides cosmogenic contributions that are a factor 5 larger than those for a constant comoving source density (right panel).

Note that extending the UHE CR emission spectrum below 50 EeV will necessarily increase the contribution of cosmogenic neutrinos and γ-rays. In this sense, our flux predictions can be considered as *lower limits* of the cosmogenic emission, that only depend on the observed average mass composition A_o above 50 EeV. The right panel of Fig. 2 shows the summary of our "minimial" cosmogenic neutrino fluxes for the two source evolution scenarios in comparison to neutrino upper limits from IceCube [37] and Pierre Auger [38] as well as the sensitivity of future neutrino observatories IceCube-Gen2 [40] and GRAND200k [39]. One can notice that future neutrino observatories are capable of detecting cosmogenic neutrino emission in the EeV range if the contribution of protons above 50 EeV is at least 10%. This is consistent with earlier results [4, 44].

As mentioned earlier, our "minimal" flux predictions have a simple scaling with observed CR mass number as $J \propto A_o^{2-\gamma}$. For helium dominance, $A_o = 4$, this corresponds to a flux reduction of 1.2% compared to the case of proton dominance. This low flux level is below the sensitivity of next-generation neutrino telescope. However, our calculation does not account for cosmogenic neutrino production by the extra-galactic background light (EBL), which produces additional contribution in the sub-EeV energy range. These contributions become increasingly important for the case of heavy nuclei [4].

4. Conclusion

We have discussed the production of cosmogenic neutrinos and γ-rays by UHE CRs above energies of 50 EeV. At these high energies, the neutrino production can be simply estimated by the UHE CR nucleon spectrum, which can be estimated directly by the observed mass composition at Earth. We have shown that proton dominance above 50 EeV will result in cosmogenic neutrino fluxes that are in reach of next-generation neutrino observatories.

Depending on source evolution, a contribution of 2% ("SFR evolution") or 10% ("no evolution") would lead to detectable fluxes. On the other hand, dominance of heavier nuclei above 50 EeV will degrade the cosmogenic flux predictions as $J \propto A_o^{2-\gamma}$, making the observation of EeV cosmogenic neutrinos less likely.

Cosmogenic γ-rays can also be tested by UHE CR observatories by limits on the photon fractions. The γ-ray fluxes in these proceedings have been approximated by the absorption of γ-rays via pair production with the CMB. We are presently investigating the effect of cosmic radiation background, including the most recent estimates of the EBL and radio backgrounds as well as secondary emission of electromagnetic cascades on our flux predictions.

Acknowledgements

The authors acknowledge support from VILLUM FONDEN under project no. 18994.

References

[1] K. Greisen, *Phys. Rev. Lett.* **16** (1966) 748–750.
[2] G. T. Zatsepin and V. A. Kuzmin, *JETP Lett.* **4** (1966) 78–80.

[3] V. S. Berezinsky and G. T. Zatsepin, *Yad. Fiz.* **11** (1970) 200–205.
[4] M. Ahlers and F. Halzen, *Phys. Rev. D* **86** (2012) 083010, arXiv:1208.4181.
[5] P. A. Zyla *et al.*, (Particle Data Group Collaboration), *PTEP* **2020** no. 8, (2020) 083C01.
[6] M. Ahlers, L. A. Anchordoqui, and S. Sarkar, *Phys. Rev. D* **79** (2009) 083009, arXiv:0902.3993.
[7] M. Ahlers and A. M. Taylor, *Phys. Rev. D* **82** (2010) 123005, arXiv:1010.3019.
[8] A. Franceschini, G. Rodighiero, and M. Vaccari, *Astron. Astrophys.* **487** (2008) 837, arXiv:0805.1841.
[9] A. Franceschini and G. Rodighiero, *Astron. Astrophys.* **603** (2017) A34, arXiv:1705.10256.
[10] R. J. Protheroe and P. L. Biermann, *Astropart. Phys.* **6** (1996) 45–54, arXiv:astro-ph/9605119. [Erratum: Astropart.Phys. 7, 181 (1997)].
[11] I. C. Niţu, H. T. J. Bevins, J. D. Bray, and A. M. M. Scaife, *Astropart. Phys.* **126** (2021) 102532, arXiv:2004.13596.
[12] G. R. Blumenthal, *Phys. Rev. D* **1** (1970) 1596–1602.
[13] F. W. Stecker, *Phys. Rev.* **180** (1969) 1264–1266.
[14] J. L. Puget, F. W. Stecker, and J. H. Bredekamp, *Astrophys. J.* **205** (1976) 638–654.
[15] A. Mücke, R. Engel, J. P. Rachen, R. J. Protheroe, and T. Stanev, *Comput. Phys. Commun.* **124** (2000) 290–314, arXiv:astro-ph/9903478.
[16] L. Morejon, A. Fedynitch, D. Boncioli, D. Biehl, and W. Winter, *JCAP* **11** (2019) 007, arXiv:1904.07999.
[17] S. Yoshida and M. Teshima, *Prog. Theor. Phys.* **89** (1993) 833–845.
[18] C. T. Hill and D. N. Schramm, *Phys. Lett. B* **131** (1983) 247.
[19] R. J. Protheroe and P. A. Johnson, *Astropart. Phys.* **4** (1996) 253, arXiv:astro-ph/9506119.
[20] R. Engel, D. Seckel, and T. Stanev, *Phys. Rev. D* **64** (2001) 093010, arXiv:astro-ph/0101216.
[21] M. Ahlers, L. A. Anchordoqui, M. C. Gonzalez-Garcia, F. Halzen, and S. Sarkar, *Astropart. Phys.* **34** (2010) 106–115, arXiv:1005.2620.
[22] G. B. Gelmini, O. Kalashev, and D. V. Semikoz, *JCAP* **01** (2012) 044, arXiv:1107.1672.
[23] J. Heinze, D. Boncioli, M. Bustamante, and W. Winter, *Astrophys. J.* **825** no. 2, (2016) 122, arXiv:1512.05988.
[24] D. Hooper, A. Taylor, and S. Sarkar, *Astropart. Phys.* **23** (2005) 11–17, arXiv:astro-ph/0407618.
[25] M. Ave, N. Busca, A. V. Olinto, A. A. Watson, and T. Yamamoto, *Astropart. Phys.* **23** (2005) 19–29, arXiv:astro-ph/0409316.
[26] D. Allard, M. Ave, N. Busca, M. A. Malkan, A. V. Olinto, E. Parizot, F. W. Stecker, and T. Yamamoto, *JCAP* **09** (2006) 005, arXiv:astro-ph/0605327.
[27] L. A. Anchordoqui, H. Goldberg, D. Hooper, S. Sarkar, and A. M. Taylor, *Phys. Rev. D* **76** (2007) 123008, arXiv:0709.0734.
[28] K. Kotera, D. Allard, and A. V. Olinto, *JCAP* **10** (2010) 013, arXiv:1009.1382.
[29] S. Yoshida and A. Ishihara, *Phys. Rev. D* **85** (2012) 063002, arXiv:1202.3522.
[30] A. Romero-Wolf and M. Ave, *JCAP* **07** (2018) 025, arXiv:1712.07290.

PoS(ICRC2021)1005

[31] R. Alves Batista, R. M. de Almeida, B. Lago, and K. Kotera, *JCAP* **01** (2019) 002, arXiv:1806.10879.
[32] K. Møller, P. B. Denton, and I. Tamborra, *JCAP* **05** (2019) 047, arXiv:1809.04866.
[33] A. van Vliet, R. Alves Batista, and J. R. Hörandel, *Phys. Rev. D* **100** no. 2, (2019) 021302, arXiv:1901.01899.
[34] J. Heinze, A. Fedynitch, D. Boncioli, and W. Winter, *Astrophys. J.* **873** no. 1, (2019) 88, arXiv:1901.03338.
[35] A. Aab *et al.*, (Pierre Auger Collaboration), *Phys. Rev. Lett.* **125** no. 12, (2020) 121106, arXiv:2008.06488.
[36] A. Aab *et al.*, (Pierre Auger Collaboration), *Phys. Rev. D* **102** no. 6, (2020) 062005, arXiv:2008.06486.
[37] M. G. Aartsen *et al.*, (IceCube Collaboration), *Phys. Rev. D* **98** no. 6, (2018) 062003, arXiv:1807.01820.
[38] A. Aab *et al.*, (Pierre Auger Collaboration), *JCAP* **10** (2019) 022, arXiv:1906.07422.
[39] J. Álvarez-Muñiz *et al.*, (GRAND Collaboration), *Sci. China Phys. Mech. Astron.* **63** no. 1, (2020) 219501, arXiv:1810.09994.
[40] M. G. Aartsen *et al.*, (IceCube-Gen2 Collaboration), *J. Phys. G* **48** no. 6, (2021) 060501, arXiv:2008.04323.
[41] A. M. Hopkins and J. F. Beacom, *Astrophys. J.* **651** (2006) 142–154, arXiv:astro-ph/0601463.
[42] H. Yuksel, M. D. Kistler, J. F. Beacom, and A. M. Hopkins, *Astrophys. J. Lett.* **683** (2008) L5–L8, arXiv:0804.4008.
[43] R. Alves Batista, A. Dundovic, M. Erdmann, K.-H. Kampert, D. Kuempel, G. Müller, G. Sigl, A. van Vliet, D. Walz, and T. Winchen, *JCAP* **05** (2016) 038, arXiv:1603.07142.
[44] A. van Vliet, R. Alves Batista, and J. R. Hörandel, *PoS* **ICRC2019** (2021) 1025, arXiv:1909.01932.

PoS(ICRC2021)1005

Bibliography

[1] The Pierre Auger Collaboration. *Measurement of the cosmic ray energy spectrum above* 2.5×10^{18} eV *using the Pierre Auger Observatory.* Phys. Rev. D 102 (2020) 062005; arXiv:2008.06486.

[2] The Pierre Auger Collaboration. *Features of the energy spectrum of cosmic rays above* 2.5×10^{18} eV *using the Pierre Auger Observatory.* Phys. Rev. Lett. 125 (2020) 121106; arXiv:2008.06488.

[3] G. T. Zatsepin, V. A. Kuz'min. *Upper Limit of the Spectrum of Cosmic Rays.* Pis'ma Zh. Eksp. Teor. Fiz. 4 (1966) 114. http://jetpletters.ru/ps/1624/article_24846.pdf

[4] K. Greisen. *End to the cosmic ray spectrum?* Phys. Rev. Lett. 16 (1966) 748-750.

[5] B. P. Abbott *et al.* (LIGO Scientific Collaboration and Virgo Collaboration). *GW170817: Observation of Gravitational Waves from a Binary Neutron Star Inspiral.* Phys. Rev. Lett. 119 (2017), 161101.

[6] The IceCube Collaboration, Fermi-LAT, MAGIC, AGILE, ASAS-SN, HAWC, H.E.S.S., INTEGRAL, Kanata, Kiso, Kapteyn, Liverpool Telescope, Subaru, Swift/NuSTAR, VERITAS, VLA/17B-403 teams. *Multimessenger observations of a flaring blazar coincident with high-energy neutrino IceCube-170922A.* Science, Vol. 361, No. 6398, eaat1378 (2018).

[7] CRPropa3 documentation: https://crpropa.github.io/CRPropa3/

[8] K.M. Groth, Y. Génolini and M. Ahlers. *Improved Limits on Cosmogenic Fluxes from Ultra-High Energy Cosmic Rays.* Proceedings of 37th International Cosmic Ray Conference — PoS(ICRC2021), 395 (2021) 1005.

[9] M. Spurio. *Probes of Multimessenger Astrophysics.* 2018 (2nd ed.)

[10] V. F. Hess. *Über Beobachtungen der durchdringenden Strahlung bei sieben Freiballonfahrten.* Phys.Z. 13 (1912) 1084-1091.

[11] J. Linsley. *Evidence for a Primary Cosmic-Ray Particle with Energy* 10^{20} eV. Phys. Rev. Lett. 10 (1963) 146.

[12] S. Abdollahi *et al.* (Fermi-LAT). *Cosmic-ray electron-positron spectrum from 7 GeV to 2 TeV with the Fermi Large Area Telescope.* Phys. Rev. D95 (2017) 8, 082007.

[13] C. Evoli. *The Cosmic-Ray Energy Spectrum.* Zenodo (2020, December 1). http://doi.org/10.5281/zenodo.4396125

[14] P.A. Zyla *et al.* (Particle Data Group), Prog. Theor. Exp. Phys. 2020, 083C01 (2020). Sec. 30 "Cosmic Rays". https://pdg.lbl.gov/2021/reviews/rpp2020-rev-cosmic-rays.pdf

[15] The Pierre Auger Collaboration. *Combined fit of spectrum and composition data as measured by the Pierre Auger Observatory.* CAP 04 (2017) 038, JCAP 03 (2018) E02 (erratum); arXiv:1612.07155.

[16] D. Ikeda, W. Hanlon *et al.* (Telescope Array Collab.). *Hybrid Measurement of the Energy Spectrum and Composition of Ultra-High Energy Cosmic Rays by the Telescope Array.* PoS ICRC2017 (2017) 515.

[17] V. de Souza *et al.* (Telescope Array and Pierre Auger Collabs.). *Testing the agreement between the $X_{\max}$ distributions measured by the Pierre Auger and Telescope Array Observatories.* PoS ICRC2017 (2017) 522.

[18] M. Muzio, G. Farrar, M. Unger. *Constraining the origin of UHECRs and astrophysical neutrinos.* PoS (2021) ICRC 1021.

[19] R. A. Batista *et al. Open Questions in Cosmic-Ray Research at Ultrahigh Energies.* Front.Astron.Space Sci. 6 (2019) 23; arXiv: 1903.06714.

[20] A. M. Hillas. *The Origin of Ultra-High-Energy Cosmic Rays.* Annual review of astronomy and astrophysics. Volume 22 (1984) p. 425-444.

[21] J.K. Becker. *High-energy neutrinos in the context of multimessenger physics.* Phys. Rept. 458 (2008) 173-246; arXiv:0710.1557.

[22] P.A. Zyla *et al.* (Particle Data Group), Prog. Theor. Exp. Phys. 2020, 083C01 (2020). Sec. 2 "Astrophysical Constants and Parameters". https://pdg.lbl.gov/2020/reviews/rpp2020-rev-astrophysical-constants.pdf

[23] R. J. Protheroe and P. A. Johnson. Propagation of Ultra High Energy Protons over Cosmological Distances and Implications for Topological Defect Models. Astropart.Phys. 4 (1996) 253.

[24] R. Gilmore *et al. Semi-analytic modelling of the extragalactic background light and consequences for extragalactic gamma-ray spectra* . Mon. Not. R. Astron. Soc. 422 (2012) 3189–3207.

[25] I.C. Nitu and H.T.J. Bevins and J.D. Bray and A.M.M. Scaife. An updated estimate of the cosmic radio background and implications for ultra-high-energy photon propagation. Astroparticle Physics 126(11):102532 (2021)

[26] H. Bethe, W. Heitler. *On the stopping of fast particles and on the creation of positive electrons.* Proc. Roy. Soc. Lond. A 146 (1934) 83-112.

[27] G. Blumenthal. *Energy Loss of High-Energy Cosmic Rays in Pair-Producing Collisions with Ambient Photons.* Phys. Rev. D 1 (1970) 1596–1602.

[28] D. Kuempel. *Extragalactic Propagation of Ultra-High Energy Cosmic Rays.* 10th Rencontres du Vietnam, Very High Energy Phenomena in the Universe (2014); arXiv:1409.3129.

[29] CRPropa 3 (2018): C. Heiter, D. Kuempel, D. Walz, M. Erdmann. *Photon production and electromagnetic cascade propagation.* Astropart. Phys. 102 (2018) 39; arXiv:1710.11406.

[30] R.A. Batista, D. Boncioli, A. di Matteo, A. van Vliet, D. Walz. *Effects of uncertainties in simulations of extragalactic UHECR propagation, using CRPropa and SimProp.* JCAP 10 (2015) 063; arXiv:1508.01824.

[31] D. Hooper, S. Sarkar, A.M. Taylor. *The intergalactic propagation of ultra-high energy cosmic ray nuclei.* Astropart. Phys. 27 (2007) 199-212 arXiv:astro-ph/0608085.

[32] CRPropa 3 (2016): R. A. Batista, A. Dundovic, M. Erdmann, K. Kampert, D. Kuempel, G. Müller, G. Sigl, A. van Vliet, D. Walz, T. Winchen. *CRPropa 3 - a Public Astrophysical Simulation Framework for Propagating Extraterrestrial Ultra-High Energy Particles.* JCAP 1605 (2016) 038; arXiv:1603.07142.

[33] M. G. Aartsen *et al.* (IceCube-Gen2 Collaboration). *IceCube-Gen2: The Window to the Extreme Universe.* J. Phys. G 48 no. 6, (2021) 060501; arXiv:2008.04323.

[34] M. Ackermann *et al. The spectrum of isotropic diffuse gamma-ray emission between 100 MeV and 820 GeV.* ApJ 799 (2015) 86.

[35] M. Huber (for the IceCube Collaboration). *Searches for steady neutrino emission from 3FHLblazars using eight years of IceCube data from the Northern hemisphere.* PoS-ICRC2019-916 (2019); arXiv:1908.08458.

[36] M. Ackermann *et al.* (Fermi-LAT), Astrophys. J. 799, 86 (2015); arXiv: 1410.3696

[37] M.G. Aartsen *et al.* (IceCube Collaboration) (2017); arXiv: 1710.01191

[38] A. Aab *et al.* (Pierre Auger Collaboration). *The Pierre Auger Observatory: Contributions to the 34th International Cosmic Ray Conference (ICRC 2015).* PoS(ICRC2015) (2015); arXiv: 1509.03732.

[39] M. Ahlers. *Neutrino Sources from a Multi-Messenger Perspective.* Proceedings of the 7th Roma International Conference on Astroparticle Physics (2018); arXiv: 1811.07633

[40] M. Ahlers, L. A. Anchordoqui, M. C. Gonzalez-Garcia, F. Halzen, S. Sarkar. *GZK Neutrinos after the Fermi-LAT Diffuse Photon Flux Measurement.* Astroparticle Physics 34 (2010) 106-115; arXiv:1005.2620v2

[41] M. Ahlers, J. Salvado. *Cosmogenic gamma-rays and the composition of cosmic rays.* Phys. Rev. D 84 (2011) 085019; arXiv:1105.5113.

[42] R. J. Gould and G. P. Schréder. Pair Production in Photon-Photon Collisions. Phys. Rev. 155, 1404 (1967)

[43] P. Bhattacharjee, G Sigl. *Origin and Propagation of Extremely High Energy Cosmic Rays.* Phys.Rept.327 (2000) 109-247; arXiv:astro-ph/9811011.

[44] S. Lee. Propagation of extragalactic high energy cosmic and γ rays, Phys. Rev. D 58 043004 (1998)

[45] M. Ahlers, L.A. Anchordoqui, and S. Sarkar. *Neutrino diagnostics of ultrahigh energy cosmic ray protons.* Phys. Rev. D 79 (2009) 083009.

[46] CRPropa (2007): E. Armengaud, G. Sigl, T. Beau, F. Miniati. *CRPropa - A Numerical Tool for the Propagation of UHE Cosmic Rays, γ-rays and Neutrinos.* Astropart. Phys. 28: 463-471 (2007); arXiv:astro-ph/0603675v2.

[47] CRPropa 2 (2012): K. Kampert, J. Kulbartz, L. Maccione, N. Nierstenhoefer, P. Schiffer, G. Sigl, A. van Vliet. *CRPropa 2 - a Public Framework for Propagating High Energy Nuclei, Secondary Gamma Rays and Neutrinos.* Astropart.Phys. 42 (2013) 41-51; arXiv:1206.3132.

[48] SimProp (2012): R. Aloisio, D. Boncioli, A. F. Grillo, S. Petrera, F. Salamida. *SimProp: a Simulation Code for Ultra High Energy Cosmic Ray Propagation.* JCAP 1210 (2012) 007; arXiv:1204.2970.

[49] PriNCe (2019): J. Heinze, A. Fedynitch, D. Boncioli and W. Winter. *A new view on Auger data and cosmogenic neutrinos in light of different nuclear disintegration and air-shower models.* Astrophys. J. 873 (2019) no.1, 88 https://doi.org/10.3847/1538-4357/ab05ce

[50] R. A. Batista. *Propagation of Astroparticles: a multimessenger view.* Astroparticle Seminar at the Niels Bohr International Academy (NBIA), Copenhagen, Denmark, 2021. https://8rafael.com/files/RAB-NBIA-2021.pdf

[51] D. Walz. *Constraining models of the extragalactic cosmic ray origin with the Pierre Auger Observatory.* PhD thesis, RWTH Aachen U. (2016).

[52] M. Ahlers, F. Halzen. *Minimal cosmogenic neutrinos.* Phys. Rev. D 86 (2012) 083010; arXiv:1208.4181.

[53] H. Yuksel, M. D. Kistler, J. F. Beacom, and A. M. Hopkins. *Revealing the High-Redshift Star Formation Rate with Gamma-Ray Bursts.* Astrophys. J. Lett. 683 (2008) L5–L8; arXiv:0804.4008.

[54] M. G. Aartsen *et al.* (IceCube Collaboration). *Differential limit on the extremely-high-energy cosmic neutrino flux in the presence of astrophysical background from nine years of IceCube data.* Phys. Rev. D 98 no. 6, (2018) 062003; arXiv:1807.01820.

[55] A. Aab *et al.* (Pierre Auger Collaboration). *Probing the origin of ultra-high-energy cosmic rays with neutrinos in the EeV energy range using the Pierre Auger Observatory.* JCAP 10 (2019) 022; arXiv:1906.07422.

[56] J. Álvarez-Muñiz *et al.* (GRAND Collaboration). *The Giant Radio Array for Neutrino Detection (GRAND): Science and Design*. Sci. China Phys. Mech. Astron. 63 no. 1 (2020) 219501; arXiv:1810.09994.

[57] A. Aab *et al.* (Pierre Auger Collaboration). *The Pierre Auger Observatory: Contributions to the 35th International Cosmic Ray Conference (ICRC 2017)*. PoS(ICRC2017) (2017); arXiv:1708.06592.

[58] R. J. Protheroe and T. Stanev. Electron-photon cascading of very high-energy gamma-rays in the infrared background. Mon. Not. R. Astron. Soc. 264, 191 (1993).

[59] CRPropa 3.1.7 release on GitHub: https://github.com/CRPropa/CRPropa3/releases/tag/3.1.7

[60] CRPropa 3.2 (2021): R. A. Batista, J. B. Tjus, J. Dörner, A. Dundovic, B. Eichmann, A. Frie, C. Heiter, M.R. Hoerbe, K.H. Kampert, L. Merten, G. Müller, P. Reichherzer, A. Saveliev, L. Schlegel, G. Sigl, A. van Vliet and T. Winchen. *CRPropa 3.2: a framework for high-energy astroparticle propagation*. PoS (2021) ICRC 938.

[61] C. Bleve (for the Pierre Auger Collaboration). *Updates on the neutrino and photon limits from the Pierre Auger Observatory*. Proceedings of The 34th International Cosmic Ray Conference — PoS(ICRC2015) 236 (2016) 1103.

[62] A. Neronov, I. Vovk. *Evidence for strong extragalactic magnetic fields from Fermi observations of TeV blazars*. Science 328 (2010) 73-75; arXiv:1006.3504.

[63] P.A. Zyla *et al.* (Particle Data Group), Prog. Theor. Exp. Phys. 2020, 083C01 (2020). Sec. 48 "Kinematics" https://pdg.lbl.gov/2020/reviews/rpp2020-rev-kinematics.pdf